ABSTRACT

Title of Dissertation: RELATIONSHIPS BETWEEN TURBULENT WALL PRESSURE AND VELOCITY FIELD SOURCES

Peter Asha Chang, III, Doctor of Philosophy, 1998

Dissertation directed by: Associate Professor Ugo Piomelli
Department of Mechanical Engineering

Although the study of wall pressure fluctuations (WPFs) has a long and venerable history, relatively little is known about the nature of the source terms responsible for the wall pressure. This study takes advantage of the three-dimensional velocity fields available from turbulence simulations to try to answer some long-standing questions about the nature of WPFs. Which parts of the boundary layer generate the various wavenumber regions of the wall pressure? What are the dominant source terms? What are the relative magnitudes of the mean-shear (MS) and turbulence-turbulence (TT) wall pressures? What physical processes in the boundary layer generate the wall pressure?

The velocity field sources and partial wall pressures were computed from a database generated by a direct numerical simulation of a low Reynolds number,

fully developed, turbulent channel flow. Results show that the mean-shear (MS) and turbulence-turbulence (TT) partial pressures (π^{MS} and π^{TT}, respectively) are the same order of magnitude. The buffer region dominates most of the wavenumber range; the viscous shear layer is significant at the highest-wavenumbers; buffer and logarithmic regions are important at low-wavenumbers. The dominant length scales of the MS source term indicate that it is generated by near-wall shear layers. Over most of the wavenumber range, the contribution from the buffer region is the dominant TT component; in the low-wavenumber range the viscous shear-layer, buffer region, and logarithmic region are dominant; in the medium- and high-wavenumbers the viscous shear-layer and buffer region. The most important TT partial pressures are π_{23}^{TT}, π_{13}^{TT} and π_{12}^{TT} from the buffer region. It is hypothesized that π_{23}^{TT} and π_{13}^{TT} are generated by quasi-streamwise vortices that are parallel and tilted with respect to the wall, respectively. π_{12}^{TT} may be due to near-wall shear layers and spanwise vortices, but is much less important than π^{MS}. π_{23}^{TT}, π_{22}^{TT} and π_{33}^{TT} from the viscous shear-layer are the dominant high wavenumber partial pressures; they may be due to the downward side of quasi-streamwise vortices impinging on the wall.

Modelling the MS pressure depends upon the vertical velocity field. It was shown that the streamwise spectra of v, normalized by its mean square, is constant across the channel. The peak of the spanwise spectra, however, shifts towards lower wavenumbers with distance from the wall. The $k_z\delta$ location of the peak varies as y^0, $y^{-1/3}$ and y^{-1} in the viscous shear-layer, buffer layer, and logarithmic region, respectively. Further efforts are necessary to scale the amplitude of the spanwise v spectra. For $y/y' \leq 1.0$, the broadband correlations were shown to collapse to a single curve when plotted versus y/y'.

RELATIONSHIPS BETWEEN TURBULENT WALL PRESSURE AND VELOCITY FIELD SOURCES

by

Peter Asha Chang, III

Dissertation submitted to the Faculty of the Graduate School of the
University of Maryland, College Park in partial fulfillment
of the requirements for the degree of
Doctor of Philosophy
1998

Advisory Committee:

Associate Professor Ugo Piomelli, Chairman/Advisor
Professor James Wallace
Professor James Duncan
Professor Jewel Barlow
Dr. William Blake

Dedication

To my wife, Margaret

and my daughters, Sally and Sophie

Acknowledgements

I would like to express my deepest appreciation to my advisor Prof. Ugo Piomelli for the many years of guidance, insights, and high standards of quality which made this work possible. Special thanks are also due to Dr. William K. Blake for his technical guidance, inspiration and for serving on my Advisory Committee. I would also like to thank the rest of my Advisory Committee: Profs. James Wallace, James Duncan, and Jewel Barlow.

Thanks to all those who I have associated with at University of Maryland: Chandrasekhar Kannepalli and Drs. Jun-Hui Liu and Xiaoli Huai who helped with understanding the details of the turbulence simulation codes Pedro Espina and all the others in the CFD Laboratory.

I would like to thank my coworkers at David Taylor Model Basin: Dr. Wen-Chin Lin, who, in all his wisdom, guided me toward turbulence simulations; Drs. Francis Noblesse, Dane Hendrix, Tom Fu, Mark Busby and David Coakley, and Mike Griffin, Robin Imber, Gabor Karafiath, Richard Messalle and Toby Ratcliffe for their constant encouragement; Brian Hill for indirectly helping in innumerable ways; Steven C. Fisher for computer system support; Dr. Theodore Farabee and Bruce Abraham of NUWC for teaching me the experimental aspects of wall pressure; Drs. Mario Casarella and Steven J. Russell for

fruitful technical discussions; Serena Lin-Bush, for providing graphics assistance, humor and common sense; Dr. Bruce Douglas, for helping to fund the early years of this work.

I am deeply indebted to my wife, Margaret for her infinite patience, support and love throughout all the years of work. I could not, and would not have, done it without her. I would also like to acknowledge my two daughters, Sally and Sophie, for their humor and love, and whose own achievements have been a source of inspiration to me. I would also like to acknowledge the encouragement of Margaret's and my parents and family.

This work was performed at the Naval Surface Warfare Center — Carderock Division (NSWCCD), West Bethesda, MD. It was sponsored by the Hydroacoustics 6.2 project; by the In-House Laboratory Independent Research (ILIR) Program administered by the Office of the Research Director, Bruce Douglas, Code 0112, NSWCCD for the office of the Chief of Naval Research; and by a grant of High Performance Computing (HPC) time from the Department of Defense (DoD) HPC Shared Resource Center, Army Corps of Engineers Waterways Experiment Station (CEWES), Vicksburg, MS (Cray Y-MP and C-90).

This dissertation was formatted using the `dissertation` style developed by Pablo A. Straub* for the LaTeX document processing system.

*Straub, Pablo A., "The `dissertation` LaTeX Style," available by anonymous ftp from ftp.umiacs.umd.edu in the directory pub/um-dissertation

Table of Contents

List of Tables

Number **Page**

List of Figures

Number **Page**

RELATIONSHIPS BETWEEN TURBULENT
WALL PRESSURE AND
VELOCITY FIELD SOURCES

Peter Asha Chang, III

December 9, 1998

Defense in Rm 2164 at 10 AM on Wednesday September 9, 1998.

Phone numbers and email addresses for committee and candidate:
Ugo Piomelli 301-405-5254, ugo@eng.umd.edu
James Wallace 410-455-3313, wallaced@eng.umd.edu
James H. Duncan 301-405-5260, duncan@eng.umd.edu
William Blake 301-227-1879, wblake@dt.navy.mil
Jewel Barlow, barlow@eng.umd.edu
Peter Chang 301-227-7059, changp@dt.navy.mil

This comment page is not part of the dissertation.

Typeset by LaTeX using the `dissertation` style by Pablo A. Straub, University of Maryland.

Chapter 1

Introduction

1.1 Previous Work

Wall pressure fluctuations (WPFs) are caused by the passage of turbulent flow over the wall bounding the flow. They are the cause of flow-induced structural noise, which can cause undesireable airplane cabin noise and interference with acoustic sensors and are also important for wind-wave generation on air-water interfaces and scouring of the sea-bed [Blake (1986), Willmarth (1975)]. WPFs are related to the turbulent flow through a Poisson equation, and they are a function of all the sources in the flow domain. The source terms consist of the so-called mean shear (MS) or linear term and turbulence-turbulence (TT) or non-linear terms. The former represents the interaction between the mean shear and the fluctuating velocity gradients, while the latter represent the interactions between fluctuating-velocity gradients. The MS term is also called the "rapid" term, because it changes rapidly in response to the flow conditions, whereas the TT term is called the "slow" term since it is affected only through non-linear interactions [Kim (1989)]. Because of the complexity of the three-dimensional and time-dependent turbulent flows, it

has been difficult to determine the exact relationship between velocity field sources and WPFs. The present state of knowledge of the character of WPFs and their sources is due to the contributions of many researchers over the past 40 years. Their work can be roughly divided into three areas: modelling; characterization in frequency and frequency-wavenumber space; determination of source terms and their relationships to WPFs, in physical space. In this review, only references that directly relate to the current work will be mentioned. Comprehensive overviews of the work prior to 1988 can be found in Willmarth (1975) and Eckelmann (1988).

Modelling

Modelling efforts are aimed at providing a WPF model in wavenumber-frequency space that provides the forcing function for flow-induced structural noise predictions. The modal response of a structure is the product of the WPF forcing function and the structural acceptances. Corcos (1963) developed a model that assumes that the cross-spectral density of pressure is the product of three functions: the autospectrum of the point pressure fluctuations and two exponential functions, to account for pressure decorrelation in the streamwise and spanwise directions. The Corcos model was developed to describe the cross spectrum of pressures dominated by the convective wavenumber range. As initially developed, it has questionable validity in the sub-convective wavenumber range ($k_x \ll \omega/U_c$, where k_x is the streamwise wavenumber, U_c is the convection velocity and ω denotes the radian frequency) because measurements and applications at the time were from the convective range. In many subsequent applications [Blake (1986)], the underlying wall structure has its major acceptance modes in the subconvective wavenumber range; thus, variants of the Corcos model, which attempt to model

the subconvective wavenumber range are widely used for flow-induced structural noise predictions [Hwang and Maidanik (1990), Ko and Schloemer (1992)].

Models that explicitly include the source terms have more potential for accurate modelling. Blake (1971, 1986) expressing the solution to Poisson equation in a form first applied by Lilley (1960) obtained a double integral over the wall-normal coordinate, which involves the evaluation of the five-dimensional cross-spectral density of the wall-normal velocity fluctuations, $\Phi_{22}(y, y', \mathbf{K}, \omega)$ (y is the wall-normal coordinate, $\mathbf{K}$ denotes the planar wavenumber vector). He further assumed that the cross-spectral density can be separated into a wall-normal correlation function, and streamwise and spanwise wavenumber spectra of the wall-normal velocity. However, even these much simpler functions are difficult to determine because of the lack of data that may be used to define the spatial structure of the wall-normal velocity field.

Panton and Linebarger (1974) followed in this vein by invoking further detail in describing the variation of root-mean-square (r.m.s.) quantities in the boundary-layer, but they characterized spatial statistical properties of the sources as essentially homogenous. Recently, Zawadski *et al.* (1996) evaluated Blake's (1971) formulation for a flow with adverse pressure gradient and separation using direct numerical simulation (DNS) data. They were able to define some of the essential correlations and predict the wall pressure spectra which had the correct trends when compared with DNS pressure.

Chase (1980) was the first to attempt modeling of the spatial characteristics of boundary-layer structure and attempted to invoke details of structure. He assumed that the wavenumber spectra of the wall-normal velocity scales like Ky (K denotes the planar wavenumber amplitude), based on the conclusions of Morrison and

Kronauer (1969); Chase (1980) then obtained a form for both the MS and TT pressure spectra that is dependent upon eight empirical coefficients, which control the shape and level of the pressure spectra.

These models point out that there is a need for more information about the source terms, and more information about the wavenumber-frequency characteristics of WPFs, particularly in the subconvective wavenumber range range, with which to validate the models.

Characterization in spectral space

Analysis of the frequency spectra of WPFs at a point on the plane was perhaps the first tool used to study the nature of the source terms. By associating various frequency ranges with regions of the boundary-layer it has been possible to hypothesize where in the boundary-layer the dominant sources are located. In the ensuing discussions frequency and streamwise wavenumber, k_x $(= \omega/U_c)$ will be used interchangeably, since in the literature both appear, and can be related to each other through Taylor's frozen convection hypothesis. Accordingly, most early work in source modelling addresses principally convected pressure fluctuations.

Bradshaw (1967) argued that between $k_x\delta \approx 4$ (δ is the boundary-layer thickness) and a wavenumber inversely proportional to the height of the viscous shear layer, the spectra should have a k_x^{-1} decay rate. This is called the "overlap region" because the pressure spectra will collapse for varying Reynolds numbers when normalized both by outer and inner variables. It has been shown by many researchers [Farabee and Casarella (1991), Keith *et al.* (1992), Olivero-Bally *et al.* (1993)] that there is a region with a k_x^{-1} decay, which increases in size with

Reynolds number [Panton (1974), Blake (1986)]. Kraichnan (1956), considering just the Poisson equation solution for the MS pressure, determined that in the low wavenumbers the spectra should have a k_x^2 behavior. This was confirmed by Farabee and Casarella (1991), who used noise-cancellation techniques to obtain accurate low-frequency spectra. At high wavenumbers, a k_x^{-5} behavior is expected. If inner-scaling is used, the k_x^{-5} behavior appears universal (*i.e.*, independent of Reynolds number) [Farabee and Casarella (1991), Keith *et al.* (1992), Olivero-Bally *et al.* (1993), Chang *et al.* (1994)].

In an effort to shed some light on the relationship between wavenumber spectra and source locations, Panton and Linebarger (1974), starting with the formulation of Kraichnan (1956), obtained an approximate numerical solution for the contribution of the MS term to the pressure. They validated the k_x^{-1} decay rate and, in addition, showed the influence that various regions of the boundary-layer have on the streamwise-wavenumber pressure spectra. They demonstrated that MS sources from the outer region ($y > 0.2\delta$) affected only the low-wavenumbers ($k_x\delta < 20$), up to the location where the k_x^{-1} decay rate began. The middle ($33.6\nu/u_\tau < y < 0.2\delta$) ($\nu$ is the kinematic viscosity, and u_τ is the friction velocity) and inner regions ($y^+ < 33.6$)* affected the higher-wavenumbers. They also showed that sources from the middle region become dominant at the lowest wavenumbers, hinting at the possibility that all regions of the boundary-layer contribute to the low-wavenumber pressure.

Blake (1986) showed that the k_x^2, k_x^{-1} and k_x^{-5} behaviors can be obtained by just considering the MS term, and making estimates for the mean velocity derivative and the cross-spectral density of the wall-normal velocity fluctuations appropriate

*$y^+ = yu_\tau/\nu$

to the various regions of the boundary-layer (viscous shear-layer, logarithmic and wake regions). The fact that experimental data confirms these behaviors lends credence to the belief that the MS term is more important than the TT terms. It also confirms the conjecture that there is correlation between certain regions of the boundary-layer wavenumber ranges. In summary, the weight of the evidence is that the k_x^2 range is due to the wake region; the k_x^{-1} is due to the logarithmic region; the k_x^{-5} range is due to the viscous shear-layer.

Characterization in physical space

Perhaps the first experiments that showed the two-dimensional physical characteristics of wall pressure were performed by Emmerling, Meier and Dinkelacker (1973); using optical interferometry techniques they were able to view the flexible wall deformations caused by the wall pressure fluctuations beneath a turbulent boundary layer. It is now thought that coherent turbulent structures are very important for wall pressure generation and that high-amplitude wall-pressure events contribute a significant proportion to the mean-square wall-pressure, even though they only occur a fraction of the time [Karangelen (1991), Abraham and Keith (1995)]. Based on experimental and numerical evidence, it has long been known that the boundary-layer is populated by coherent events. Overviews of the key developments in coherent-event research are given by Cantwell (1981) and Robinson (1991). When Cantwell (1981) wrote his review article, the accepted boundary-layer events were: (1) low-speed sublayer streaks, possibly related to pairs of streamwise vortices; (2) the lift-up of streaks and their turbulent bursting, occuring at an outer scaled frequency, pointing to inner-layer bursting events controlled by outer flow events; (3) tilted shear layers, the upstream sides of which

were sites of intense turbulence activity; (4) the inner buffer region as the site for most of the turbulence production. Based on these notions, researchers studied the relationship between velocity and wall pressure events using conditional sampling techniques. Thomas and Bull (1983) used VITA techniques in an experimental turbulent boundary-layer to obtain conditional samples of pressure traces related to high-amplitude velocity perturbations. They concluded that high-amplitude wall-pressure events are produced by near-wall shear layers and that such events consist of a region of positive pressure with upstream and downstream regions of negative pressure. Johansson *et al.* (1987), also using conditional sampling techniques, showed that near-wall shear layers and positive pressure events have a bi-directional relationship (*i.e.*, the same events are detected whether velocity or pressure is used as the detection criteria) and hypothesized that the MS term was primarily responsible for the high-amplitude wall-pressure events.

The 1980's and 90's saw the increasing usage of numerical simulations of turbulent channel and boundary-layer flows. Simulations allow access to the three-dimensional and temporal velocity field data, from which coherent events can be extracted more easily. Robinson *et al.* (1988, 1989) and Robinson (1991a,b) used a database obtained from a direct numerical simulation (DNS) of a low-Reynolds number boundary-layer, determined that quasi-streamwise vortices and near-wall shear layers are among the primary turbulent structures in wall-bounded flows, and that spanwise vortices in the logarithmic region occur less frequently. They hypothesized that horseshoe and hairpin vortices proposed by many researchers [Cantwell (1981), Robinson(1991b)], which are a combination of quasi-streamwise vortices and spanwise vortices, were less common than the individual vortices. They hypothesized that near-wall shear layers are closely related to quasi-

streamwise and spanwise vortices: they are thought to form when high-speed outer-region fluid collides with the slower-moving fluid ejected from the upward-directed sides of the quasi-streamwise or spanwise vortices [Robinson *et al.* (1988)].

Visualization of turbulence structures showed that quasi-streamwise vortices generate regions of negative wall-pressure beneath low-pressure vortex cores and ejections, while positive pressures have been shown to occur beneath sweeps [Robinson *et al.* (1988), Bernard and Thomas (1993)]. Using the DNS of Kim *et al.* (1987), Johansson, Alfredsson, and Kim (1988) conditionally averaged the streamwise velocity to obtain a three-dimensional and temporal view of near-wall shear layers and their relationship with wall pressure. They found convincing evidence that high-amplitude wall-pressure events are related to near-wall shear layers; the pressure footprint they obtained seems consistent with the findings of Thomas and Bull (1983). Using the DNS database of Choi and Moin (1990), Lueptow, (1995) detected pressure-gradient events, and found a pressure footprint consistent with previous workers [Thomas and Bull (1983), Johansson, Alfredsson, and Kim (1988), Wilczynski (1992)]. Using the same database, Abraham and Keith (1995) detected high-amplitude negative and positive wall-pressure events and computed their planar wavenumber spectra.

Casarella and his coworkers have pursued the relationships between coherent events and wall pressure in a low-noise experimental facility described in Farabee (1986): Wilczynski (1992) found that the relationship between wall pressure gradients and Reynolds stress events was stronger than that between pressure peaks and velocity peaks, and detected wall-pressure gradient events and related them to $u - v$ velocity fields. Kammeyer (1995) and Russell (1997) used pressure itself to detect high-amplitude wall-pressure events, and conditionally averaged

the associated velocity fields. Russell (1997) used band-pass frequency filtering to obtain pressure-velocity fields in frequency bands commonly associated with inner-, mixed- and outer-scaling. His results are generally in agreement with the notion that the shear layers generate high-amplitude wall-pressure events. Kammeyer (1995), using wavelet transforms, found similar structures.

Another advantage of numerical simulations is that, from the two-dimensional wall pressure fields, the frequency-wavenumber (three-spectra) can be obtained, although their computation is quite expensive [Handler *et al.* (1984), Chang *et al.* (1994)]. A long time series is necessary to obtain a reasonably well-resolved, yet smooth, spectrum; grid resolution must match the frequency resolution in order to resolve the convective ridge and obtain the correct high frequency behavior. Choi and Moin (1990) computed a well-resolved wavenumber-frequency spectra using a simulation of fully developed channel flow. They were able to evaluate various methods of computing convection velocity and study the similarity form of the frequency spectrum. However, there were questions about the behavior of their spectra in the subconvective wavenumber range. Chang *et al.* (1994) compared the wavenumber-frequency spectra computed using LES and DNS and studied their characteristics, particularly in the sub-convective wavenumber range. They obtained much lower subconvective wavenumber energy than Choi and Moin (1990). Singer (1996) performed an LES of a turbulent boundary-layer, and obtained the frequency spectra of wall pressure, at a Reynolds number 5 times higher than that of Chang *et al.* (1994).

Numerical simulations have also allowed, for the first time, analysis of the source terms. Kim and Lee (1989) and Kim (1989) computed the wall-normal distribution of the mean-squares of the MS and TT source terms. Their data showed that the

dominant source term is the one most strongly associated with streamwise vortices.

Dhanak *et al.* (1997) numerically simulated single and pairs of streamwise vortices and studied the space-time characteristics of the related wall pressure. They showed that the time-space trace of the pressure footprint closely resembled that detected experimentally. They obtained frequency and spanwise wavenumber power spectra, which showed the same roll-offs obtained for the total pressure, although their spectra levels were functions of an externally imposed flow field and vortex parameters.

In summary, accurate WPF modelling suffers from lack of information about the source terms and the well-resolved wavenumber-frequency pressure spectra that can be used for validation. The weight of the research into turbulent structures has lead to the conclusion that, at least in low Reynolds number flows, quasi-streamwise vortices and near-wall shear layers are the dominant coherent events. Turbulence simulation databases have been used to study in depth the nature of wall pressure, but have been used only sparingly to study the nature of the source terms.

1.2 Objectives

The objective of this work is to use a DNS database to study the relationships between the velocity field source terms and the wall pressure. The approach used here is to determine which source terms are important for wall pressure generation, and then to correlate these dominant source terms to physical events in the flow-field. This will be accomplished by identifying the regions (buffer layer, logarithmic region *etc.*) that give the most significant contributions to the pressure spectra

in various wavenumber ranges, and then by relating the dominant terms to the turbulent structures in the boundary-layer.

Chapter 2 describes the mathematical formulation and numerical techniques of the turbulence simulations; it contains the derivation of the Poisson equation for wall pressure and its analytical solution for a channel flow. Chapter 3 validates the velocity and wall pressure fields, comparing statistics, spectra and correlations to published data. In Chapter 4 the total wall pressure is decomposed into partial pressures due to individual terms and regions and the dominant partial pressures are determined. Chapter 5 is concerned with the characteristics of the sources associated with the dominant partial pressures; it is found that these source terms are closely related to coherent turbulent events. Chapter 6 investigates modelling of the MS pressure and uses the channel flow data to begin to model the terms in the MS pressure formulation. Finally, concluding remarks and recommendations for further research can be found in Chapter 7.

Chapter 2

Mathematical Formulation

This chapter describes, in detail, the mathematical formulation and numerical techniques used in the turbulence simulations of the fully developed turbulent channel flow that was used to generate the pressure databases. Also it describes the derivation and solution of the Poisson equation for fluctuating wall pressure. The governing equations are described in Section 2.1; the numerical techniques are presented in Section 2.2; mathematical differences between the modified pressure obtained directly from the simulations and the physical pressure are derived in Section 2.4. Derivation of the Poisson equation for fluctuating pressure is described in Section 2.5 and its analytical solution are described in Section 2.6.

2.1 Governing equations

The time-dependent, three-dimensional Navier-Stokes and continuity equations for incompressible flow are

$$\frac{\partial u_i}{\partial t} + \frac{\partial}{\partial x_j}\left(u_i u_j\right) = -\frac{\partial P}{\partial x_i} + \frac{1}{Re_\ell}\frac{\partial^2 u_i}{\partial x_j \partial x_j} \tag{2.1.1}$$

$$\frac{\partial u_i}{\partial x_i} = 0. \tag{2.1.2}$$

The three velocity components of the large-scale motions in the three directions* are u, v and w or u_1, u_2 and u_3; P is the *physical* pressure, whereas the modified pressure (see below) is denoted by ϕ. The flow variables are made dimensionless by the half-channel width, δ, a reference velocity U_ℓ and the kinematic viscosity, ν. The reference Reynolds number Re_ℓ is defined as

$$Re_\ell = \frac{U_\ell \delta}{\nu}. \tag{2.1.3}$$

2.2 Numerical technique

The time-dependent, incompressible Navier-Stokes equations (2.1.1) in vector form can be written as

$$\frac{\partial \mathbf{u}}{\partial t} + h(\mathbf{u}) = -\nabla P + \nu \nabla^2 \mathbf{u} \tag{2.2.1}$$

where $h(\mathbf{u})$ is the nonlinear term. The nonlinear term $h(\mathbf{u})$ can be written in the skew-symmetric form

$$h(\mathbf{u}) = \frac{1}{2}\left[\mathbf{u} \cdot \nabla \mathbf{u} + \nabla \cdot (\mathbf{u}\mathbf{u})\right] \tag{2.2.2}$$

or in the rotational form

$$h(\mathbf{u}) = -\mathbf{u} \times \boldsymbol{\omega} + \frac{1}{2}\nabla \cdot (\mathbf{u}\mathbf{u}) \tag{2.2.3}$$

where $\boldsymbol{\omega} = \nabla \times \mathbf{u}$ is the vorticity vector. The term $\frac{1}{2}\nabla \cdot (\mathbf{u}\mathbf{u})$ goes into the modified pressure term if the rotational form is used, and the resultant computed pressure is $P + \frac{1}{2}\nabla \cdot (\mathbf{u}\mathbf{u})$. Zang (1991) showed that the skew-symmetric form is the most

*The streamwise direction will be denoted by x or x_1, the vertical direction by y or x_2, and the spanwise direction by z or x_3.

accurate, while the rotational form is less expensive. Both forms have been used in the present simulations.

The governing equations have been advanced in time by a fractional time step method [Zang and Hussaini (1986)]. Fourier expansions were used in the streamwise and spanwise directions, with a Chebychev collocation method in the wall-normal direction.

Temporal discretization

The Navier-Stokes equations (2.2.1) can be written in the form

$$\frac{\partial \mathbf{u}}{\partial t} = \mathbf{H} - \nabla P + \nu \frac{\partial^2 \mathbf{u}}{\partial y^2} \tag{2.2.4}$$

where

$$\mathbf{H} = -\frac{1}{2}\mathbf{u} \cdot \nabla \mathbf{u} - \frac{1}{2}\nabla \cdot (\mathbf{u}\mathbf{u}) + \nu \left(\nabla^2 \mathbf{u} - \frac{\partial^2 \mathbf{u}}{\partial y^2} \right). \tag{2.2.5}$$

In the fractional time step method, an intermediate velocity $\mathbf{u}^*$ is computed first from a Helmholtz equation (the momentum equations without the pressure term); then, a pressure correction is obtained by computing a Poisson equation for the modified pressure defined in (2.4.10) to enforce the continuity constraint. Equation (2.2.4) is discretized as

$$\frac{\mathbf{u}^* - \mathbf{u}^n}{\Delta t} = \mathbf{H} + \nu \frac{\partial^2 \mathbf{u}^n}{\partial y^2} \tag{2.2.6}$$

and

$$\frac{\mathbf{u}^{n+1} - \mathbf{u}^*}{\Delta t} = -\nabla \phi^{n+1}. \tag{2.2.7}$$

Taking the divergence of the latter equation and using the divergence-free condition for $\mathbf{u}^{n+1}$ yields a Poisson equation for the modified pressure

$$\nabla^2 \phi^{n+1} = \frac{1}{\Delta t} \nabla \cdot \mathbf{u}^*. \tag{2.2.8}$$

The intermediate velocity $\mathbf{u}^*$ and modified pressure ϕ are computed from (2.2.6) and (2.2.8); subsequently, (2.2.7) gives velocity $\mathbf{u}^{n+1}$.

The vertical diffusion term $\nu\frac{\partial^2\mathbf{u}}{\partial y^2}$ in equation (2.2.6) is treated by the Crank-Nicholson scheme, which is implicit and second order accurate in time. The nonlinear term $\mathbf{H}$, which includes the nonlinear term and the remaining diffusion terms, is advanced by using a low storage third-order Runge-Kutta method [Williamson, 1980]. Thus, the time advancement process of the governing equations is

STAGE 1

$$\begin{cases} \left[1-\frac{1}{6}\Delta t\nu\frac{\partial^2}{\partial y^2}\right]\mathbf{u}^{*\prime} &= \left[1+\frac{1}{6}\Delta t\nu\frac{\partial^2}{\partial y^2}\right]\mathbf{u}^n+\frac{1}{3}\Delta t\mathbf{H}^n \\ \frac{1}{3}\Delta t\nabla^2\phi' &= \nabla\cdot\mathbf{u}^{*\prime} \\ \mathbf{u}' &= \mathbf{u}^{*\prime}-\frac{1}{3}\Delta t\nabla\phi' \end{cases} \tag{2.2.9}$$

STAGE 2

$$\begin{cases} \left[1-\frac{5}{24}\Delta t\nu\frac{\partial^2}{\partial y^2}\right]\mathbf{u}^{*\prime\prime} &= \left[1+\frac{5}{24}\Delta t\nu\frac{\partial^2}{\partial y^2}\right]\mathbf{u}^{*\prime} \\ & \quad +\frac{15}{16}\Delta t\Big(\mathbf{H}'-\frac{5}{9}\mathbf{H}^n\Big) \\ \frac{5}{12}\Delta t\nabla^2\phi'' &= \nabla\cdot\mathbf{u}^{*\prime\prime} \\ \mathbf{u}'' &= \mathbf{u}^{*\prime\prime}-\frac{5}{12}\Delta t\nabla\phi'' \end{cases} \tag{2.2.10}$$

STAGE 3

$$\begin{cases} \left[1-\frac{1}{8}\Delta t\nu\frac{\partial^2}{\partial y^2}\right]\mathbf{u}^{*n+1} &= \left[1+\frac{1}{8}\Delta t\nu\frac{\partial^2}{\partial y^2}\right]\mathbf{u}^{*\prime\prime} \\ & \quad +\frac{8}{15}\Delta t\Big(\mathbf{H}''-\frac{153}{128}\mathbf{H}'+\frac{153}{128}\cdot\frac{5}{9}\mathbf{H}^n\Big) \\ \frac{1}{4}\Delta t\nabla^2\phi^{n+1} &= \nabla\cdot\mathbf{u}^{*n+1} \\ \mathbf{u}^{n+1} &= \mathbf{u}^{*n+1}-\frac{1}{4}\Delta t\nabla\phi^{n+1}; \end{cases} \tag{2.2.11}$$

these equations are solved in Fourier space.

The CFL value for the RK3 scheme is computed from

$$CFL=\max\left[\Delta t\left(\left|\frac{u}{\Delta x}\right|+\left|\frac{v}{\Delta y}\right|+\left|\frac{w}{\Delta z}\right|\right)\right]; \tag{2.2.12}$$

For numerical stability, the RK3 scheme requires $CFL < 0.55$. The value used in the simulations was between 0.2 and 0.4.

Spatial discretization

In the simulations Fourier expansions are used in the streamwise and spanwise directions and Chebychev expansions are employed in the wall-normal direction. The Fourier series expansions of velocity are

$$\mathbf{u}(x,y,z,t) = \sum_{k_x=-\frac{N_x}{2}}^{\frac{N_x}{2}-1} \sum_{k_z=-\frac{N_z}{2}}^{\frac{N_z}{2}-1} \widehat{\mathbf{u}}(k_x,y,k_z,t)\, e^{i(\widehat{k}_x x+\widehat{k}_z z)} \tag{2.2.13}$$

where $\widehat{k}_x = \frac{2\pi}{L_x}k_x$, $\widehat{k}_z = \frac{2\pi}{L_z}k_z$, and L_x and L_z are the imposed periodicity lengths in the streamwise and spanwise directions; N_x and N_z are the number of points in the streamwise and spanwise directions. The collocation points in the periodic directions are

$$x_i = \frac{2\pi i}{N_x L_x}, \qquad i = 0,1,\ldots,N_x-1 \tag{2.2.14}$$

$$z_k = \frac{2\pi k}{N_z L_z}, \qquad k = 0,1,\ldots,N_z-1 \tag{2.2.15}$$

The Chebychev expansion of the Fourier coefficient $\widehat{\mathbf{u}}(k_x,y,k_z,t)$ is

$$\widehat{\mathbf{u}}(k_x,y,k_z,t) = \sum_{j=0}^{N_y} \tilde{\mathbf{u}}(k_x,j,k_z,t)\, T_j(\xi) \tag{2.2.16}$$

where N_y is the number of grid points, j is the Chebychev collocation point, and $T_j(\xi)$ is the Chebychev polynomial,

$$T_j(\xi) = \cos(j\cos^{-1}\xi), \qquad j = 0,1,\ldots,N_y. \tag{2.2.17}$$

In the wall-normal direction, the velocities are defined at the full-grid points

$$\xi_j = \cos\frac{\pi j}{N_y}, \qquad j = 0,1,\ldots,N_y \tag{2.2.18}$$

and the pressure is defined at the staggered (half-) grid points

$$\xi_{j+\frac{1}{2}} = \cos\frac{\pi(j+\frac{1}{2})}{N_y}, \quad j = 0, 1, \ldots, N_y - 1 \tag{2.2.19}$$

The momentum equations are enforced at the full-grid points and the continuity equation is enforced at the half-grid points.

Matrix inversion

Since the Laplacian operator ∇^2 in Fourier space takes the form

$$\nabla^2 = -\widehat{k}_x^2 - \widehat{k}_z^2 + \frac{\partial^2}{\partial y^2}, \tag{2.2.20}$$

the left sides of equations (2.2.9-2.2.11) are linear functions of the second derivative operator $\frac{\partial^2}{\partial y^2}$. Applying the Chebychev expansions (2.2.16) to this operator results in a linear full $N_y \times N_y$ matrix, and the resultant forms of equations (2.2.9-2.2.11) can be expressed in a general form

$$\mathbf{LU} = \mathbf{F}. \tag{2.2.21}$$

The inversion of the matrix $\mathbf{L}$ requires a large amount of computing time and additional storage. To improve the computing efficiency, the preconditioning matrix method—an iterative technique with fast convergence—is used in the simulation.

If $\mathbf{U}^0$ is an initial guess of $\mathbf{U}$, the initial residual is

$$\mathbf{R}^0 = \mathbf{F} - \mathbf{L}\mathbf{U}^0 \tag{2.2.22}$$

which can be also written as

$$\mathbf{L}\,(\mathbf{U} - \mathbf{U}^0) = \mathbf{R}^0. \tag{2.2.23}$$

Applying a finite difference discretization technique to equations (2.2.9-2.2.11) results in a finite difference preconditioning matrix $\mathbf{G}$,

$$\mathbf{G}\ \Delta\mathbf{U}^0 = \mathbf{R}^0 \tag{2.2.24}$$

in which $\Delta\mathbf{U}^0$ is the finite difference solution of $\mathbf{U} - \mathbf{U}^0$. The iterative direction is adjusted by the Conjugate Residual method proposed by Hestenes and Stiefel (1952) to improve the convergence rates:

$$\mathbf{U}^{k+1} = \mathbf{U}^k + \alpha_k \Delta\mathbf{U}^k \tag{2.2.25}$$

with

$$\alpha_k = \frac{(\mathbf{L}\ \Delta\mathbf{U}^k, R^k)}{(\mathbf{L}\ \Delta\mathbf{U}^k, \mathbf{L}\ \Delta\mathbf{U}^k)}. \tag{2.2.26}$$

Then, the residual and the iteration equation at the k+1–th step are

$$\mathbf{R}^{k+1} = \mathbf{R}^k - \alpha_k \mathbf{L}\ \Delta\mathbf{U}^k \tag{2.2.27}$$

and

$$\mathbf{G}\ \Delta\mathbf{U}^{k+1} = \mathbf{R}^{k+1}. \tag{2.2.28}$$

This process continues until convergence is reached. The preconditioning matrix $\mathbf{G}$ used above is obtained by performing a second-order finite difference approximation to the operator $\mathbf{L}$ at the Chebychev collocation points y_j,

$$\frac{-2}{h_{j-1}(h_j + h_{j-1})} u_{j-1} + \frac{2}{h_j h_{j-1}} u_j + \frac{-2}{h_j(h_j + h_{j+1})} u_{j+1} = f_j,$$
$$j = 1, \ldots, N_y - 1 \tag{2.2.29}$$

$$u_0 = 0, \tag{2.2.30}$$

$$u_{N_y} = 0 \tag{2.2.31}$$

where $h_j = y_j - y_{j+1}$. This process shows an extremely fast convergence rate and only takes less than 30 iteration steps to reach convergence in the present simulations.

Dealiasing

The nonlinear terms of the Navier-Stokes equations and the velocity field source terms, presented later are subject to aliasing errors if measures are not taken to eliminate them. The 2/3 dealiasing rule was used to eliminate aliasing errors in the computation of the nonlinear products. Aliasing occurs because the multiplication of two functions with M resolved components results in a function with energy in $2M$ components, with the highest M modes unresolved. Fourier transforming the product will result in the unresolved energy being aliased back into the resolved modes. In the pseudo-spectral method used here, the nonlinear terms are computed in physical space, but need to be transformed into Fourier space for solution. In the 2/3 dealiasing rule the entire simulation is run on a grid which has $3M_x/2$ and $3M_z/2$ collocation points in each of the planar directions, respectively. The following dealiasing method is described in terms of x, but the concepts are the same for z and $x - z$. Starting with velocity fields with only M_x resolved modes, multiplication will result in a function with energy in $2M_x$ modes. However, since the solution is on a grid with $3M_x$ modes, the aliased energy will be folded about the $3M_x/2 + 1$ mode so that the aliased energy will end up only in the top 1/3 modes, $M_x + 1 \leq |m| \leq 3M_x/2$. The top 1/3 modes, which would contain the aliasing errors are set to zero. The resulting velocity fields have M_x dealiased modes, or 2/3 of the modes upon which the solution is computed.

Boundary conditions

No-slip and no-flow-through boundary conditions are enforced at the walls. Periodic boundary conditions are enforced at the streamwise and spanwise boundaries.

Since the method of the fractional time step introduces the intermediate velocity $\mathbf{u}^*$, its boundary conditions also need to be defined. It can be expressed as

$$\mathbf{u}^* = \mathbf{u}^{n+1} + \Delta t \nabla \phi^{n+1} \tag{2.2.32}$$

from (2.2.7). ϕ^{n+1} is approximated by the second order accurate Taylor expansion at the boundaries and yields a third order accurate approximation for $\mathbf{u}^*$:

$$\mathbf{u}^* = \mathbf{u}^{n+1} + \Delta t \nabla \phi^n + \Delta t^2 \frac{\partial}{\partial t} \nabla \phi^n + O(\Delta t^3) \tag{2.2.33}$$

which has the same order accuracy as the RK3 scheme. The boundary condition for $\mathbf{u}^*$ is written as

$$\mathbf{u}^* = \Delta t \nabla \phi^n + \Delta t^2 \frac{\partial}{\partial t} \nabla \phi^n \tag{2.2.34}$$

at the walls.

2.3 Large-eddy simulation

In addition to the DNS that produced most of the data presented in this work, some large-eddy simulations (LES) were also run and will be discussed in Chapter 3. In large-eddy simulations the flow variables are decomposed into a large-scale (or resolved) component, denoted by an overbar, and a subgrid-scale component. The large-scale component is defined by the filtering operation,

$$\overline{f}(x_1, x_2, x_3, t) = \int_D \prod_{i=1}^{3} G_i(x_i, x_i') f(x_1', x_2', x_3', t) dx_1' dx_2' dx_3' \tag{2.3.35}$$

where D is the computation domain and G_i is the filter function in the i-th direction. Applying the filtering operation to the Navier-Stokes and continuity equations yields the governing equations for the large scale motions,

$$\frac{\partial \overline{u}_i}{\partial t} + \frac{\partial}{\partial x_j}\left(\overline{u}_i \overline{u}_j\right) = -\frac{\partial \overline{\phi}}{\partial x_i} - \frac{\partial \tau_{ij}}{\partial x_j} + \frac{1}{Re_\ell} \frac{\partial^2 \overline{u}_i}{\partial x_j \partial x_j} \tag{2.3.36}$$

$$\frac{\partial \overline{u}_i}{\partial x_i} = 0. \tag{2.3.37}$$

The subgrid-scale stress term,

$$\tau_{ij} = \overline{u_i u_j} - \overline{u}_i \overline{u}_j \tag{2.3.38}$$

represents the contribution from the subgrid scales and must be modeled. In this, the dynamic model [Germano *et al.*(1991), Lilly (1992)] has been applied. The anisotropic part of the SGS stresses are parametrized by an eddy viscosity assumption

$$\tau_{ij} \; - \; \delta_{ij}\tau_{kk}/3 = -2\nu_T \overline{S}_{ij} \tag{2.3.39}$$

where $\overline{S}_{ij}$ is the large-scale strain rate tensor is given by

$$\overline{S}_{ij} = \frac{1}{2}\left(\frac{\partial \overline{u}_i}{\partial x_j} + \frac{\partial \overline{u}_j}{\partial x_i}\right), \tag{2.3.40}$$

and the eddy viscosity ν_T is given by

$$\nu_T \; = \; C\overline{\Delta}^2 |\overline{S}|, \tag{2.3.41}$$

where $|\overline{S}| = \sqrt{2\overline{S}_{ij}\overline{S}_{ij}}$ and $\overline{\Delta} = (4\overline{\Delta}_x\overline{\Delta}_y\overline{\Delta}_z)^{1/3}$ is the filter width at the grid scale. The coefficient C is determined from the energy content of the smallest resolved scales using the least squares approach of Lilly (1992),

$$C = -\frac{1}{2}\frac{\mathcal{L}_{ij}M_{ij}}{M_{ij}M_{ij}}. \tag{2.3.42}$$

Here, $\mathcal{L}_{ij} = \widehat{\overline{u}_i\overline{u}_j} - \widehat{\overline{u}}_i\widehat{\overline{u}}_j$ "resolve the turbulent stresses" and $M_{ij} = \alpha_{ij} - \widehat{\beta_{ij}}$ where $\beta_{ij} = \overline{\Delta}^2|\overline{S}|\overline{S}_{ij}$ and $\alpha_{ij} = \widehat{\overline{\Delta}}^2|\widehat{\overline{S}}|\widehat{\overline{S}}_{ij}$. Filtering at a test scale with filter width $\widehat{\overline{\Delta}} > \overline{\Delta}$ is denoted by $\widehat{\ }$.

The numerical solution of the filtered equations is carried out using the scheme described before; however, the viscosity ν is replaced by $\nu + < \nu_T >$ (where $< \nu_T >$ is the plane-averaged turbulent eddy viscosity computed using the dynamic model); the remainder of the SGS stress is advanced explicitly using the RK3 method.

2.4 Modified versus physical pressure

As shown in Section 2.2, the modified pressure, ϕ, rather than the physical pressure, P, is solved in the simulations. In this section, the difference between the two pressures will be derived. The fractional step method with Crank-Nicholson time advancement yields a Helmholtz equation

$$\frac{\mathbf{u}^* - \mathbf{u}^n}{\Delta t} = -h(\mathbf{u}^n) + \frac{\nu}{2}\left(\frac{\partial^2 \mathbf{u}^*}{\partial y^2} + \frac{\partial^2 \mathbf{u}^n}{\partial y^2}\right). \tag{2.4.1}$$

The pressure correction step is given by

$$\frac{\mathbf{u}^{n+1} - \mathbf{u}^*}{\Delta t} = -\nabla \phi^{n+1} \tag{2.4.2}$$

Taking the divergence of (2.4.2),

$$\nabla \cdot \mathbf{u}^{n+1} - \nabla \cdot \mathbf{u}^* = -\Delta t \nabla \cdot \left(\nabla \phi^{n+1}\right) \tag{2.4.3}$$

and observing that the first term on the left-hand-side is zero by continuity, gives a Poisson equation for ϕ,

$$\nabla^2 \phi^{n+1} = \frac{1}{\Delta t} \nabla \cdot \mathbf{u}^* \tag{2.4.4}$$

The solution, $\mathbf{u}^{n+1}$ is obtained by solving (2.4.1) for $\mathbf{u}^*$, then (2.4.4) for ϕ^{n+1} and finally (2.4.2).

The question remains, how is ϕ related to the actual pressure? Add the Helmholtz and correction step equations (2.4.1) and (2.4.2) together:

$$\frac{\mathbf{u}^{n+1} - \mathbf{u}^n}{\Delta t} = -h(\mathbf{u}^n) + \frac{\nu}{2}\left(\frac{\partial^2 \mathbf{u}^*}{\partial y^2} + \frac{\partial^2 \mathbf{u}^n}{\partial y^2}\right) - \nabla \phi^{n+1} \tag{2.4.5}$$

This is almost the momentum equations with Crank-Nicholson time advancement except for that fact that the first viscous term involves $\mathbf{u}^*$. The viscous term with $\mathbf{u}^{n+1}$ can be recovered by taking the second derivative in y of (2.4.2)

$$\frac{\partial^2 \mathbf{u}^*}{\partial y^2} = \frac{\partial^2 \mathbf{u}^{n+1}}{\partial y^2} + \Delta t \frac{\partial^2}{\partial y^2}\left(\nabla \phi^{n+1}\right) \tag{2.4.6}$$

Substitute (2.4.6) into (2.4.5) to obtain

$$\frac{\mathbf{u}^{n+1}-\mathbf{u}^n}{\Delta t} = -h_i^n + \frac{\nu}{2}\left(\frac{\partial^2 \mathbf{u}^{n+1}}{\partial y^2} + \frac{\partial^2 \mathbf{u}^n}{\partial y^2}\right) \underbrace{-\nabla\phi^{n+1} + \frac{\nu\Delta t}{2}\left(\frac{\partial^2 \phi^{n+1}}{\partial y^2}\right)}_{-\frac{\partial P}{\partial x_i}}; \quad (2.4.7)$$

where the last two terms must equal the physical pressure term. This gives the relationship between P and ϕ introduced above (if the rotational form is used, P still contains also $u_i u_i/2$),

$$\frac{\partial P^{n+1}}{\partial x_i} = \nabla\phi^{n+1} - \frac{\nu\Delta t}{2}\left(\frac{\partial^2 \phi^{n+1}}{\partial y^2}\right) \quad (2.4.8)$$

Integration of the three equations in (2.4.8) gives

$$P^{n+1} = \phi^{n+1} - \frac{\nu\Delta t}{2}\frac{\partial^2 \phi^{n+1}}{\partial y^2} \quad (2.4.9)$$

The integration yields, at most, an additive constant which has been ignored since we are interested in the fluctuating pressure, and the constant would just add to the mean pressure. When using the rotational form of the nonlinear terms, the resolved kinetic energy $\mathbf{u}^{n+1}\cdot\mathbf{u}^{n+1}$ is added to the pressure term. Furthermore, for subgrid-scale models which only models the anisotropic part of the subgrid-scale stress tensor, the isotropic part $q_{sgs}^2 = \frac{1}{2}\left(\tau_{xx}+\tau_{yy}+\tau_{zz}\right)$ is added to the pressure term.

We are using a three step Runge-Kutta procedure for explicit time advancement and are interested in obtaining the pressure only after a complete time step. The effective Δt should be based on the last of the RK time increments. The third RK step advances the solution from $t_n + \frac{3\Delta t}{4}$ to $t_n + \Delta t$, thus the time increment to use in (2.4.9) is $\frac{\Delta t}{4}$, yielding the pressure equation

$$P^{n+1} + q_{sgs}^2 = \phi^{n+1} - \frac{\nu\Delta t}{8}\frac{\partial^2 \phi^{n+1}}{\partial y^2} - \frac{1}{2}\nabla\cdot\left(\mathbf{u}^{n+1}\mathbf{u}^{n+1}\right). \quad (2.4.10)$$

2.5 Derivation of Poisson equation for fluctuating pressure

The Poisson equation for fluctuating pressure is obtained by taking the divergence of the incompressible momentum equations, applying Reynolds decomposition to separate the mean and fluctuating quantities and then applying continuity. If we take the divergence of (2.1.1), and eliminate the viscous terms by applying continuity and the vector identity,

$$\nabla \times (\nabla \times \mathbf{U}) = 0, \tag{2.5.1}$$

the Poisson equation for the total pressure results:

$$\frac{\partial^2 p}{\partial x_i \partial x_i} = -\rho \frac{\partial}{\partial x_i} \left(\frac{\partial u_i u_j}{\partial x_j} \right). \tag{2.5.2}$$

We now decompose the total pressure and velocities into their mean and fluctuating quantities, where mean quantities are denoted by capital or overbar, the fluctuating quantities by primes, and the mean is a temporal- and planar-average; we have

$$\begin{aligned} p &= P + p' \\ u &= U + u' \end{aligned} \tag{2.5.3}$$

The spatial and temporal averaging satisfy the following properties characteristic of Reynolds averaging operators:

$$\begin{aligned} \overline{u_j'} &= 0 \\ \overline{U_i u_j'} &= 0 \\ \overline{\frac{\partial u_i}{\partial x_j}} &= \frac{\partial \overline{u_i}}{\partial x_j}. \end{aligned} \tag{2.5.4}$$

Expanding (2.5.2) we obtain

$$\frac{\partial^2 P}{\partial x_i \partial x_i} + \frac{\partial^2 p'}{\partial x_i \partial x_i} = -\rho \frac{\partial}{\partial x_i \partial x_j} \left(U_i U_j + U_i u_j' + u_i' U_j + u_i' u_j' \right). \tag{2.5.5}$$

We take the mean of (2.5.5), and use the properties (2.5.4) to obtain a Poisson equation for the mean pressure:

$$\frac{\partial^2 P}{\partial x_i \partial x_i} = -\rho \frac{\partial}{\partial x_i \partial x_j} \left(\overline{U_i U_j} + \overline{u_i' u_j'} \right). \tag{2.5.6}$$

Now substitute (2.5.6) into (2.5.5) to obtain the Poisson equation for the fluctuating pressure,

$$\frac{\partial^2 p'}{\partial x_i \partial x_i} = -\left\{ 2 \frac{\partial U_i}{\partial x_j} \frac{\partial u_j}{\partial x_i} + T^{TT} \right\} \tag{2.5.7}$$

where the first term on the right hand side is the mean-shear (MS) ("linear" or "rapid") source term, and the turbulence-turbulence (TT) ("nonlinear" or "slow") source term is given by

$$T^{TT} = \frac{\partial^2}{\partial x_i \partial x_j} \left(u_i' u_j' - \overline{u_i' u_j'} \right). \tag{2.5.8}$$

The TT term can be further simplified by expanding the derivatives of the terms within the parentheses and applying continuity to obtain

$$T^{TT} = \frac{\partial u_i'}{\partial x_j} \frac{\partial u_j'}{\partial x_i} - \frac{\partial^2}{\partial x_i \partial x_j} \overline{u_i' u_j'}. \tag{2.5.9}$$

Since the mean velocity for a channel flow is $U_i = (U, 0, 0)$, the final form for the Poisson equation for fluctuating pressure in a channel flow is

$$\frac{\partial^2 p}{\partial x_i \partial x_i} = -\left\{ T^{MS} + T^{TT} \right\}. \tag{2.5.10}$$

The MS term is defined as

$$T^{MS} = 2 \frac{dU}{dy} \frac{\partial v}{\partial x}, \tag{2.5.11}$$

the total TT term is the summation of all the TT terms,

$$T^{TT} = \sum_{i=1}^{3}\sum_{j=1}^{3} T_{ij}, \tag{2.5.12}$$

and the total source term is

$$T^{tot} = T^{MS} + T^{TT}. \tag{2.5.13}$$

For a plane channel the in-plane derivatives of the planar mean terms equal zero and the TT source terms become, explicitly,

$T_{11}^{TT} = \left(\frac{\partial u}{\partial x}\right)^2$	$T_{12}^{TT} = T_{21}^{TT} = \frac{\partial u}{\partial y}\frac{\partial v}{\partial x}$	$T_{13}^{TT} = T_{31}^{TT} = \frac{\partial u}{\partial z}\frac{\partial w}{\partial x}$
	$T_{22}^{TT} = \left(\frac{\partial v}{\partial y}\right)^2 - \frac{\partial^2}{\partial y^2}\overline{v^2}$	$T_{23}^{TT} = T_{32}^{TT} = \frac{\partial v}{\partial z}\frac{\partial w}{\partial y}$
		$T_{33}^{TT} = \left(\frac{\partial w}{\partial z}\right)^2$

(2.5.14)

Note that the primes on the fluctuating quantities have been dropped for convenience.

2.6 Solution for fluctuating pressure

In this section we will find a solution for the Poisson equation in terms of the unknown source terms, in order to find the attenuation of the source terms with wall-normal distance and wavenumber, and the influence that the source terms have on the wall pressure. The problem that we would like to solve is

$$\frac{\partial^2 p}{\partial x_i \partial x_i} = -T^{tot} \tag{2.6.1}$$

where $T^{tot} \equiv T^{MS} + T^{TT}$.

Boundary conditions

Boundary conditions at the top and bottom channel walls can be found from the wall-normal Navier-Stokes equation for the total velocities:

$$\frac{Dv}{Dt} = -\frac{\partial p}{\partial y} + \frac{1}{Re}\left(\frac{\partial^2 v}{\partial x^2} + \frac{\partial^2 v}{\partial y^2} + \frac{\partial^2 v}{\partial z^2}\right). \tag{2.6.2}$$

The LHS of the equation goes to zero at the walls because of the no-slip boundary conditions. Since $v = 0$ everywhere on the walls,

$$\left.\frac{\partial^2 v}{\partial x^2}\right|_{y=\pm 1} = \left.\frac{\partial^2 v}{\partial z^2}\right|_{y=\pm 1} = 0. \tag{2.6.3}$$

This leaves the condition

$$\left.\frac{\partial p}{\partial y}\right|_{y=\pm 1} = \left.\frac{1}{Re}\frac{\partial^2 v}{\partial y^2}\right|_{y=\pm 1}. \tag{2.6.4}$$

Solution method

We can transform the Poisson equation for the fluctuating pressure into Fourier space,

$$\left(\frac{\partial^2}{\partial y^2} - K^2\right)\widehat{p} = -\widehat{T} \tag{2.6.5}$$

where the $\widehat{\ }$ denotes a planar Fourier transform; $K \equiv \sqrt{k_x^2 + k_z^2}$; $k_x \equiv \frac{2\pi\delta}{L_x}$ and $k_z \equiv \frac{2\pi\delta}{L_z}$. (2.6.5) is a nonhomogenous, linear, second order, ordinary differential equation, which can be solved using variation of parameters. Note that there is no direct time dependence, meaning that disturbances in the flow given by $\widehat{T}$ are felt instantaneously at all points in the domain. The equation is elliptic; the pressure at a point is a function of all source points in the domain.

The complementary solution is given by

$$\widehat{p}_c(y) = A_1\widehat{p}_1(y) + A_2\widehat{p}_2(y) \tag{2.6.6}$$

where $\widehat{p}_1(y) \equiv e^{Ky}$ and $\widehat{p}_2(y) \equiv e^{-Ky}$. The particular solution is given by

$$\widehat{p}_p(y) = v_1(y)\widehat{p}_1(y) + v_2(y)\widehat{p}_2(y). \tag{2.6.7}$$

We solve for the particular solutions with

$$v_1(y) = -\int^y \frac{\widehat{T}^{tot}(\eta)\widehat{p}_2(\eta)d\eta}{a_o(\eta)W\left[\widehat{p}_1(\eta), \widehat{p}_2(\eta)\right]} \tag{2.6.8}$$

and

$$v_2(y) = -\int^y \frac{\widehat{T}^{tot}(\eta)\widehat{p}_1(\eta)d\eta}{a_o(\eta)W\left[\widehat{p}_1(\eta), \widehat{p}_2(\eta)\right]}. \tag{2.6.9}$$

W is the Wronskian and a_o is the coefficient of the second order term in (2.6.5). The Wronskian is $W = -2K$. The solution becomes

$$\widehat{p}(y) = A_1 e^{Ky} + A_2 e^{-Ky} + \left[\frac{1}{2K}\int^y \widehat{T}^{tot}(\eta)e^{-K\eta}d\eta\right] e^{Ky} - \left[\frac{1}{2K}\int^y \widehat{T}^{tot}(\eta)e^{K\eta}d\eta\right] e^{-Ky}. \tag{2.6.10}$$

This can be simplified to the form

$$\widehat{p}(y) = A_1 e^{Ky} + A_2 e^{-Ky} + \frac{1}{K}\int^y \widehat{T}^{tot}(\eta)\sinh\left[K(y-\eta)\right]d\eta. \tag{2.6.11}$$

Application of boundary conditions

We now apply the boundary conditions (2.6.4). We can set the lower limit of integration to anything that is convenient, as a long as we apply it consistently. We can see that setting it to $y = -1$ (the near-wall) will get rid of the integral term when we apply the boundary condition at $y = -1$. Applying the near-wall and far-wall ($y = 1$) boundary conditions, respectively, we obtain the set of equations:

$$\begin{aligned} A_1 K e^{-K} + A_2 K e^{K} &= G(-1) \\ A_1 K e^{K} + A_2 K e^{-K} &= G(1) \end{aligned} \tag{2.6.12}$$

where

$$G(-1) \equiv \left.\frac{\partial \widehat{p}}{\partial y}\right|_{y=-1}$$
$$G(1) \equiv \left.\frac{\partial \widehat{p}}{\partial y}\right|_{y=1} - \mathcal{I}_1 \tag{2.6.13}$$

$$\mathcal{I}_1 \equiv \frac{1}{K}\int_{-1}^{1} \widehat{T}^{tot}(\eta)\sinh\left[K(1-\eta)\right] d\eta \tag{2.6.14}$$

and

Solution

Finally, it can be shown that the fluctuating wall pressure can be expressed as two boundary terms and an integral over the wall-normal domain:

$$\widehat{p}(K, y=-1, \eta) = B_+ - B_- - \int_{-1}^{1} \widehat{T}^{tot}(\mathbf{K}, \eta) G(K, y=-1, \eta) d\eta, \tag{2.6.15}$$

where G is the Green's function,

$$G(K, y=-1, \eta) = \frac{\cosh[K(1-\eta)]}{K\sinh(2K)}. \tag{2.6.16}$$

The near- and far-wall upper boundary terms are given by

$$B_- \equiv \beta_-(K)\widehat{p}'(\mathbf{K}, y=-1)$$
$$B_+ \equiv \beta_+(K)\widehat{p}'(\mathbf{K}, y=1), \tag{2.6.17}$$

respectively, with the wavenumber-dependent functions given by

$$\beta_-(K) = \frac{1}{K\tanh(2K)}$$
$$\beta_+(K) = \frac{1}{K\sinh(2K)} \tag{2.6.18}$$

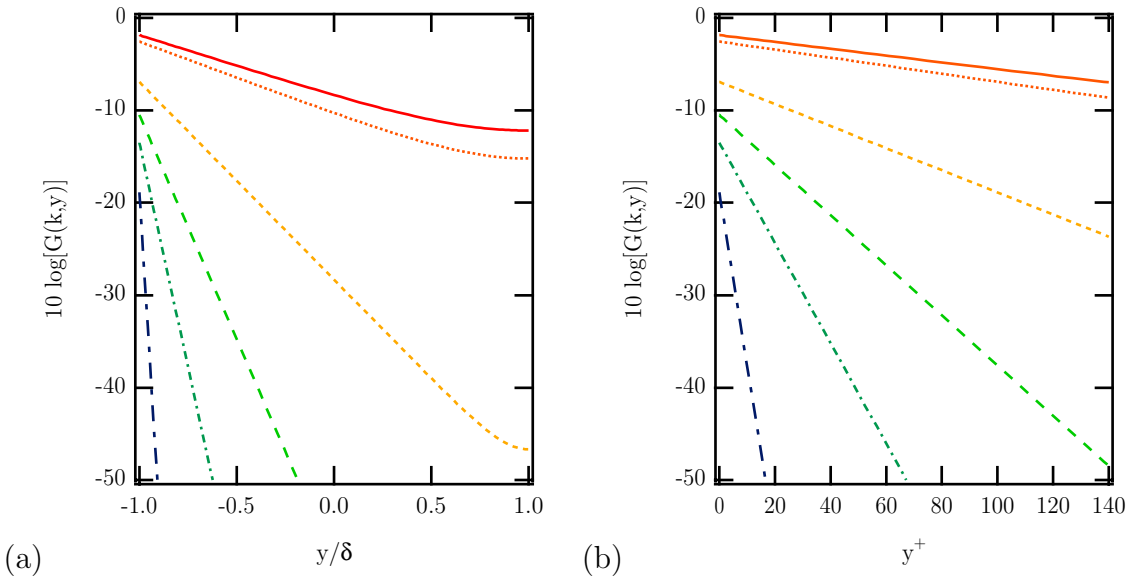

Figure 2.1: Wall-normal profiles of Green's function for wavenumber (k_x, k_z) combinations: —— : $(1/3, 3/2)$; ····· : $(1, 3/2)$; - - - - - : $(2, 9/2)$; – – – – : $(5, 10)$; –·– : $(10.5, 46.5)$ [cutoff for LES]; – – – : $(31.67, 70.5)$ [cutoff for DNS]. (a) Entire channel, (b) near-wall region.

Properties of the Green's function solution

The Green's function for fixed y, varies with η and K. Wall-normal profiles of G for K in the range occuring in the DNS, are shown in Figure 2.1(a) for the entire channel and in the near-wall region in Figure 2.1(b). Figure 2.1(a) shows that the attenuation in the lowest wavenumber is only about 12 dB across the channel, meaning that the lowest wavenumber sources may be felt all the way across the channel. However, the attenuation with increasing wavenumber is very rapid, as low wavenumbers *e.g*, $(k_x = 2, k_z = 9/2)$ are attenuated by 47 dB across the channel. Figure 2.1(b) shows the profiles out into the logarithmic region. If we classify disturbances as being insignificant if they get attenuated by 20 dB (*i.e.*, they become 1/100 of their original value at $\eta = y$), then we can see that in the buffer layer (say, $y^+ = 18$) only sources with wavenumbers less than $(k_x = 5, k_x = 10)$ are significant.

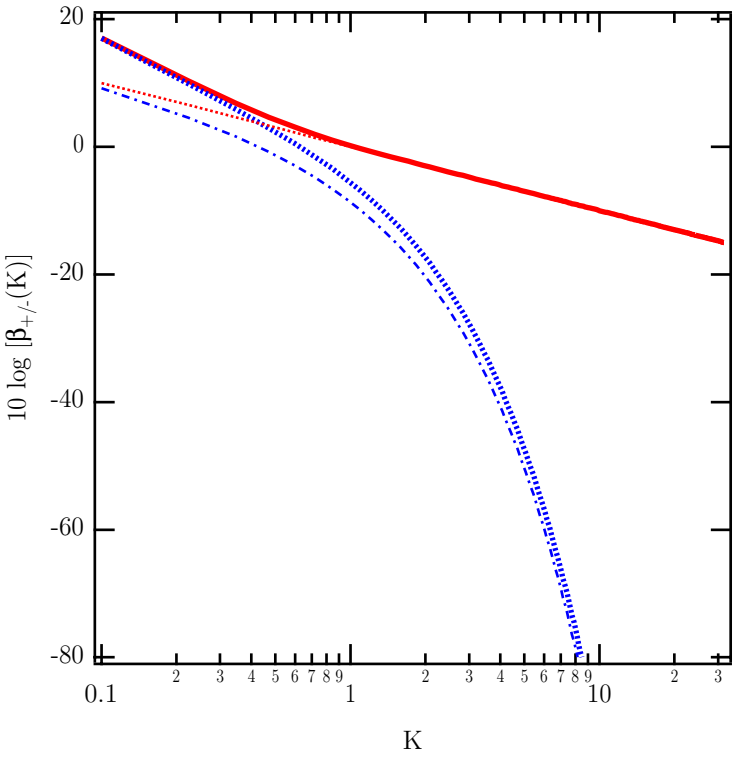

Figure 2.2: Wavenumber profiles of boundary terms: ——— : β_-; ····· : β_- (high-K limiting form); ▪▪▪▪▪ : β_+; –·– : β_+ (high-K limiting form).

Figure 2.2 shows the wavenumber-dependent functions, $\beta_-(K)$ and $\beta_+(K)$. The effect of the near-wall boundary term on the pressure at the near-wall is actually larger than 0 dB for $K \leq 1$ and then falls off slowly for larger values of K. The far-wall boundary term is greater than 0 dB for $K \leq 0.65$, and then decays rapidly for higher-K. The high-wavenumber limiting forms of $\beta(K)$ are given by

$$\beta_-(K) \approx \frac{1}{K} \tag{2.6.19}$$

and

$$\beta_+(K) \approx \frac{e^{-2K}}{K}. \tag{2.6.20}$$

The limiting forms should be used for $K > 10$. The conclusion that one can draw is that the wall-normal derivative of wall pressure at the far-wall only contributes to the near-wall pressure if it has low-K energy content.

For large values of K, G becomes a simple function:

$$G(K, y = -1, \eta) = \frac{1}{K} e^{-K(1+\eta)}. \tag{2.6.21}$$

It can be seen that G is singular as $K \to 0$, which means that it heavily weights the low-K boundary layer sources, and attenuates the high-K sources. For $K = 0$ Kim (1989) gives the formula

$$G(0, y, \eta) = 0.5(\eta - y). \tag{2.6.22}$$

Chapter 3

Characteristics of Plane Channel Flow

The purpose of this chapter is to describe the numerical simulations and to show comparisons between pressure and velocity data with those from the literature. The Chapter is divided into two sections: the first deals with validation of the velocity fields from which the wall pressure and velocity field source terms were computed; the second deals with the wall pressure fields from multiple large eddy and direct numerical simulations.

3.1 Velocity fields

In the course of this work multiple simulations were run, mainly for the purpose of studying the computational aspects of computing wall pressure wavenumber-frequency spectra. They will be discussed in Section 3.2. In this Section, only the velocity fields from LES7 and DNS5, which were used to compute the partial wall pressures and source terms in Chapters 4 and 5, respectively and for modelling of vertical velocity in Chapter 6 will be discussed.

In these simulations, the streamwise domain was $6\pi\delta$, 50 percent larger than

	LES7	DNS5	Kim *et al.* (1987)
$Re_\tau = u_\tau \delta/\nu$	171.8	179.8	~ 180
$u_\tau/U_o \times 10^2$	5.265	5.525	5.49
U_b/u_τ	16.29	15.57	15.63
U_o/U_b	1.17	1.16	1.16
δ^*/δ	0.1424	0.1396	0.141
θ/δ	0.0858	0.0858	0.087
$C_f \times 10^3$	7.54	8.25	8.18

Table I: Flow parameters for turbulence simulations

that used by Choi and Moin (1990) and Kim *et al.* (1987). The reason for the larger domain was to obtain better streamwise wavenumber resolution; the resolution for LES7 and DNS5 is $\Delta k_x \delta = 1/3$, (for a $4\pi\delta$ box it would be 1/2); the maximum value is $k_x\delta = 31.667$ for DNS5 and 11.667 for LES7. The spanwise domain for both simulations is $4/3\pi\delta$. The spanwise resolution for both simulations is $\Delta k_z \delta = 3/2$, with maximum values of $k_z\delta = 70.5$ for DNS5 and 46.5 for LES7.

DNS5 had $192 \times 96 \times 96$ collocation points in the streamwise, spanwise and wall-normal directions, respectively, whereas LES7 had $72 \times 64 \times 64$ points in each of the directions. The streamwise grid resolution for DNS5 is $\Delta x^+ = 17.6$, whereas it is 44.8 for LES7. The spanwise grid resolution for DNS5 is $\Delta z^+ = 7.8$; 11.2 for LES7. Piomelli (1993) showed that spanwise resolution $\Delta z^+ = 13$ was sufficient to resolve the near-wall streaky structures in LES. The grid point nearest the wall was $\Delta y^+ = 0.09$ for DNS5 and 0.21 for the LES7.

Both simulations used the rotational scheme and were dealiased in the streamwise and spanwise directions using the 2/3 dealiasing rule described in Section 2.2. Chang *et al.* (1994) showed that aliasing errors can significantly affect the high frequency and wavenumber components of the wall pressure spectra.

Some of the pertinent simulation parameters are listed in Table I. It shows

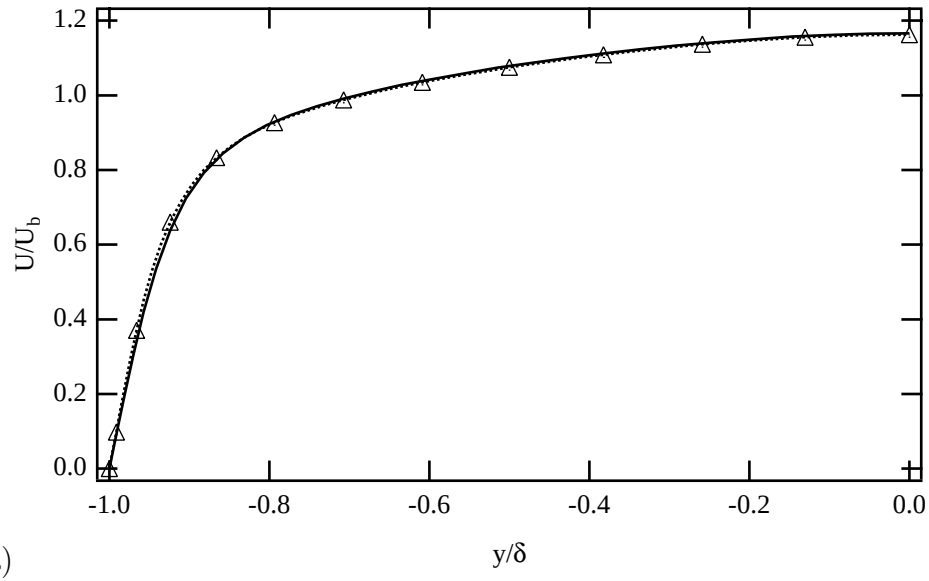

(a)

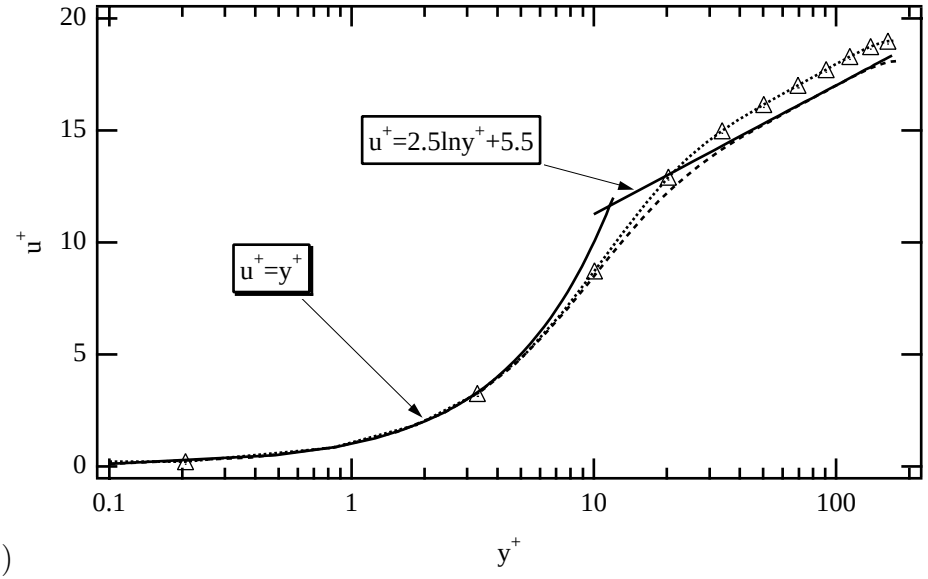

(b)

Figure 3.1: Mean velocity profiles. ····· DNS5; △ LES7. (a) Global coordinates; (b) wall coordinates.

that DNS5 and Kim *et al.* (1987) are in very good agreement. LES7 has a lower value of u_τ which is attributable to decreased grid resolution [Piomelli (1993)].

Mean velocity profiles

Figure 3.1 shows the mean streamwise velocity profiles in global and wall coordinates. In Figure 3.1(a), the velocity has been normalized by the bulk velocity,

$$U_b = \frac{1}{2}\int_{-1}^{1} U \, dy, \tag{3.1.1}$$

the comparison of velocities between DNS5 and LES7 is very good. The values of U_b/u_τ are 15.6 and 16.3 for DNS5 and LES7, respectively, in good comparison to the value of 15.6 obtained by Kim *et al.* (1987). The mean velocity profiles normalized by wall coordinates and plotted against the law of the wall $u^+ = y^+$, which defines the viscous shear-layer, and $u^+ = 2.5 \ln y^+ + B$, the logarithmic region, is shown in Figure 3.1(b). As can be seen, both DNS5 and LES7 agree very well in the viscous shear-layer but diverge slightly in the buffer layer and logarithmic region. The constant, B, is 5.5 for DNS5 and about 6 for LES7. The difference in intercepts is due primarily to u_τ; when U from LES7 is normalized by u_τ from DNS5, it collapses to the DNS5 curve. The logarithmic region extends out to the middle of the channel ($y^+ = 180$) with no trace of a wake region, as expected at this Reynolds number.

Two-point correlation coefficients

Two-point spatial correlations of velocities indicate the length scales of the turbulence structures within the channel. Since the channel flow is statistically stationary and homogenous in $x - z$ planes, the spatial correlations are only dependent upon the spatial separation between two points in that plane, and are shown only as functions of two variables: a streamwise or spanwise separation, (ξ and η, re-

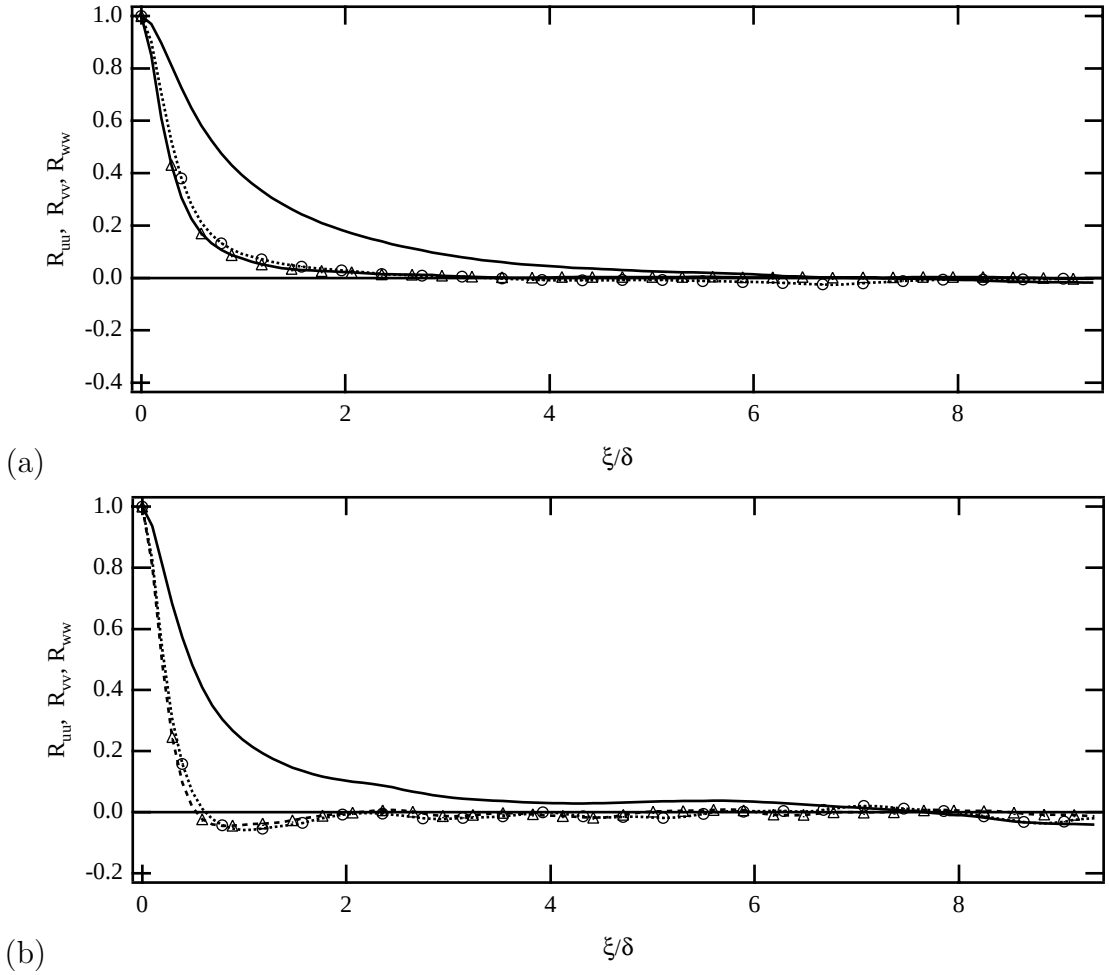

Figure 3.2: Two-point velocity correlations with streamwise separations; —— R_{uu}; $\triangle$ R_{vv}; $\circ$ R_{ww}. (a) $y^+ = 12$, (b) $y^+ = 150$.

spectively) and the wall-normal location, y. The autocorrelations are defined as

$$R_{uu}(\xi; y) \equiv \frac{< u(x; y)u(x + \xi; y) >}{< u(y)^2 >} \tag{3.1.2}$$

Shown in Figure 3.2 are the streamwise autocorrelations obtained from LES7 at $y^+ = 12$ and 150. They show that u has the largest streamwise correlations, which is probably due to the alternating low- and high- speed streaks in the near-wall region. The u correlations go to zero with a separation distance of about $\xi/\delta = 6$. This indicates that the the longest streamwise structures are less than half the box length ($L_x/\delta = 6\pi \approx 19$) and that the streamwise box-size is sufficient. The

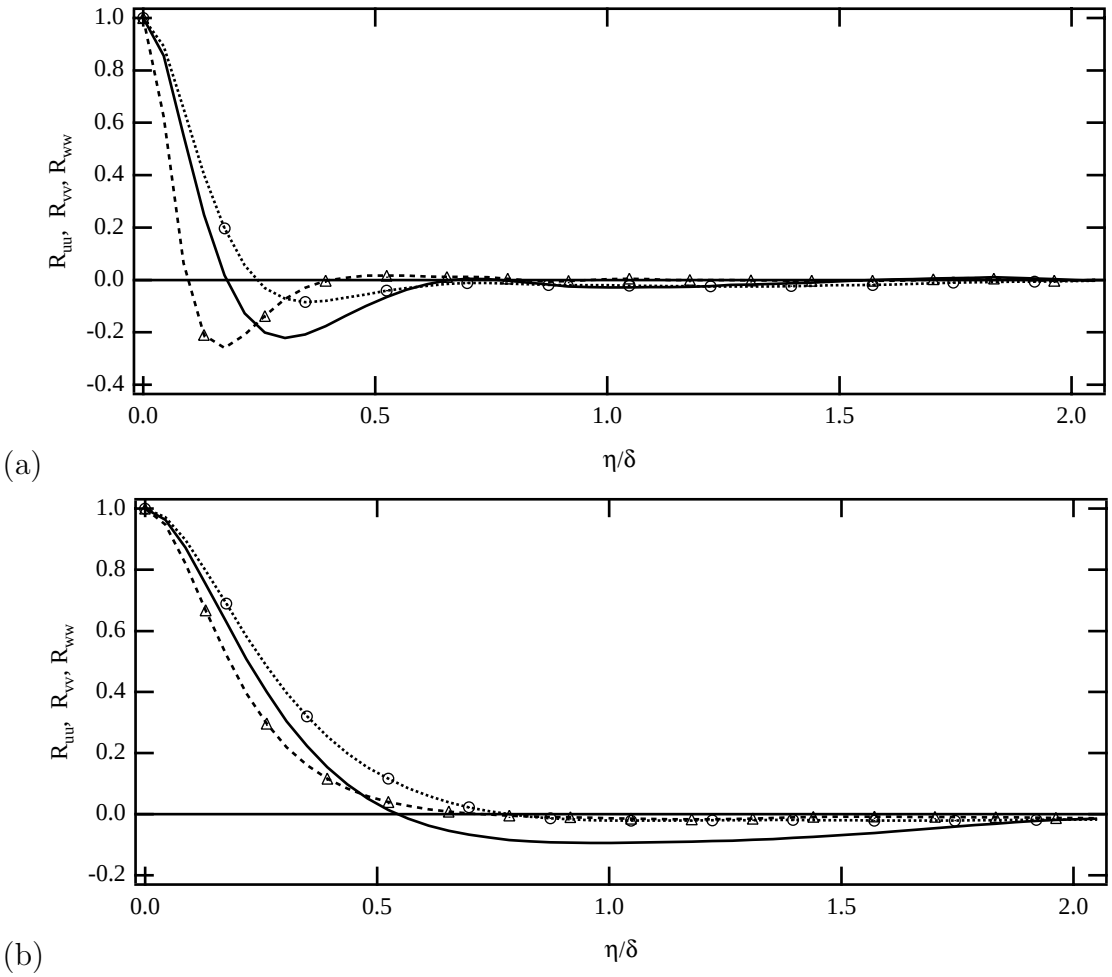

Figure 3.3: Two-point velocity correlations with spanwise separations; —— R_{uu}; $\triangle$ R_{vv}; $\circ$ R_{ww}. (a) $y^+ = 12$, (b) $y^+ = 150$.

spanwise autocorrelations of the velocities, shown in Figure 3.3, indicate that the spanwise correlation lengths are also much smaller than the streamwise lengths. The R_{uu} has a negative peak at $\eta^+ = 60$ ($\eta/\delta = 0.35$) which could be indicative of alternating streaks. These compare very well with Kim *et al.* (1987).

The streamwise and spanwise correlations of wall pressure, are shown in Figure 3.4. The streamwise correlations go to zero after about $\xi/\delta = 2 - 3$, whereas the spanwise correlations go to zero very slowly and do not reach zero for the

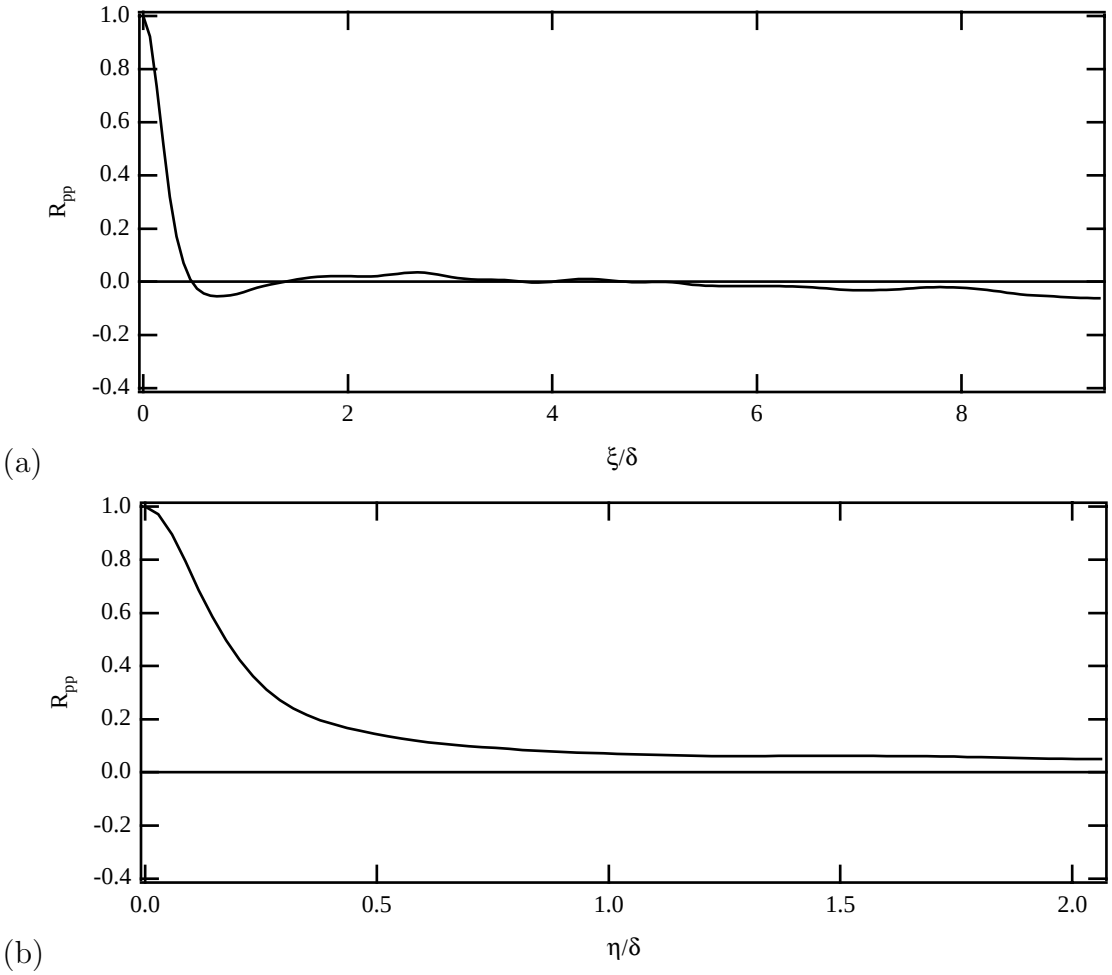

Figure 3.4: Two-point wall pressure correlations with (a) streamwise and (b) spanwise separations.

longest spanwise separations. The low correlation at $\eta/\delta = L_z/2$ (less than 0.05) is, however, acceptable, and the box was considered sufficiently wide.

Shear stress profiles

The total shear stress for a turbulence simulation, derived from the time- and space-averaged streamwise Navier-Stokes equation is given by

$$- <uv> - <\tau_{12}> + \frac{1}{Re}\frac{dU}{dy} = -y, \tag{3.1.3}$$

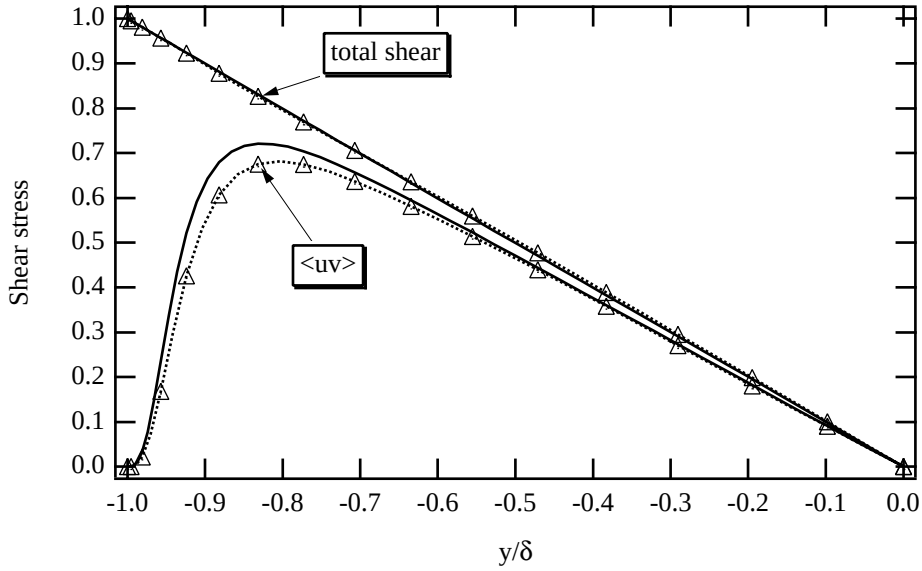

Figure 3.5: Shear stress profiles. —— DNS5; △ LES7

where u_τ, δ and ν have been used for normalization and $<\tau_{12}>$ is the subgrid scale stress, defined in (2.3.38). Thus, for a steady state solution, the average total shear stress converges to a linear function. Figure 3.5 shows that the total shear stress for DNS5 and LES7 are linear, indicating that the statistical samples are well converged. Also shown in Figure 3.5 are the Reynolds stress profiles, $<uv>$ normalized by u_τ^2. Figure 3.6 shows that the Reynolds stresses from DNS5 compare very well with DNS values from Kim *et al.* (1987). The resolved $<uv>$ profile from LES7 is slightly lower, as expected, but when the SGS stress is added ($<uv> + <\tau_{12}>$), the comparison is better.

Turbulence intensities

Wall-normal distributions of turbulence intensities show the energy distribution throughout the channel for each of the turbulent velocity components. They are defined as the square root of the planar mean of the squares of the fluctuating

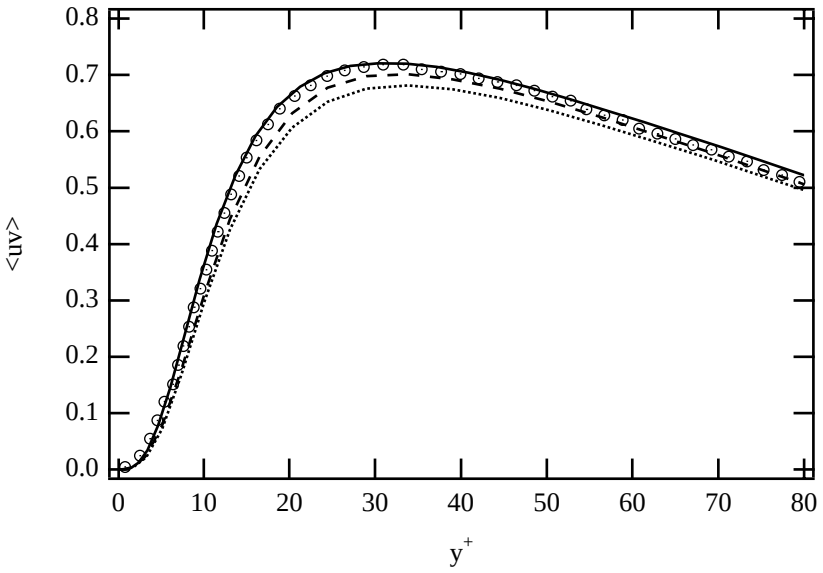

Figure 3.6: Reynolds stress profiles. —— DNS5; ····· LES7 ($< uv >$); - - - - - - LES7 ($<uv> + <\tau_{12}>$); ∘ Kim *et al.* (1987).

velocity components. Figure 3.7 shows the turbulence intensities for LES7 and DNS5 normalized by u_τ. The DNS5 data compares very well with the DNS data of Kim *et al.* (1987). The LES7 data has slightly higher values of $<uu>$, but lower values of $<vv>$ and $<ww>$.

Higher order moments

The third moment of the probability distribution, the skewness factor, denoted by S, is a measure of the anisotropy of the high amplitude velocity fluctuations. For instance, a positive skewness factor indicates a preference for high amplitude positive fluctuations (relative to the local r.m.s.). In this case, the skewness factors have been computed with the formula,

$$S_i = \frac{\langle u_i^3 \rangle}{\langle u_i^2 \rangle^{\frac{3}{2}}} \tag{3.1.4}$$

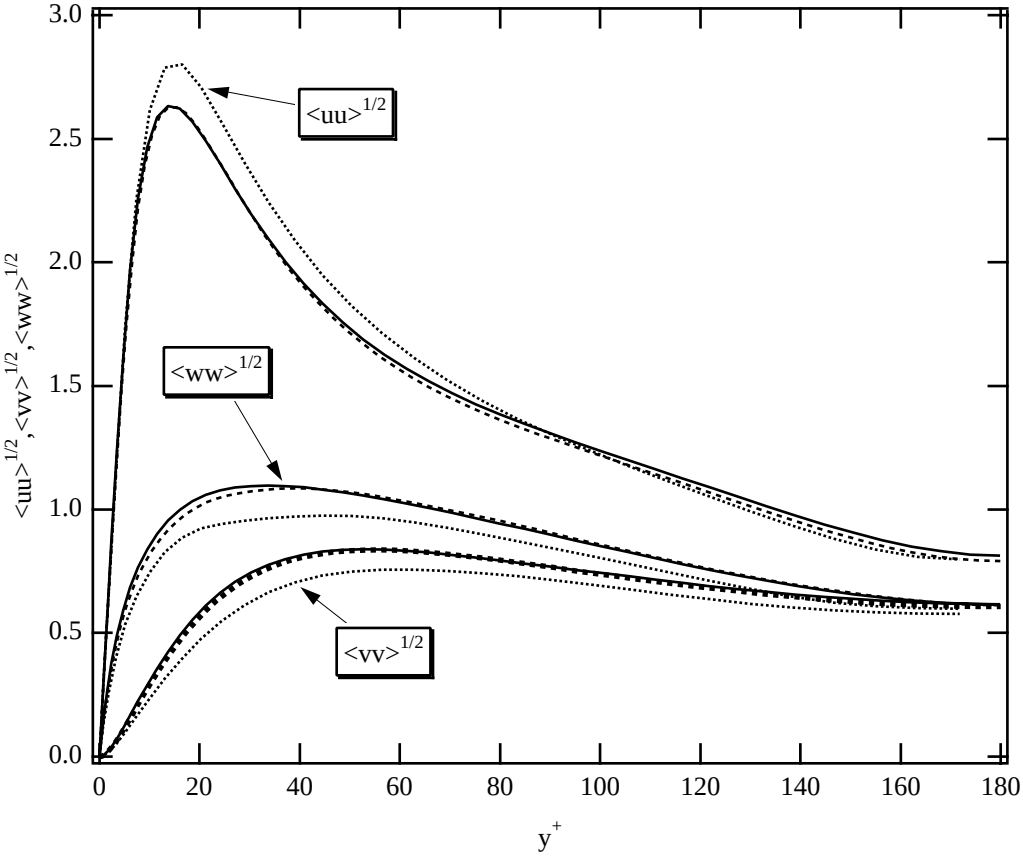

Figure 3.7: Turbulence intensity profiles. —— DNS5; ····· LES7; – – – – Kim *et al.* (1987).

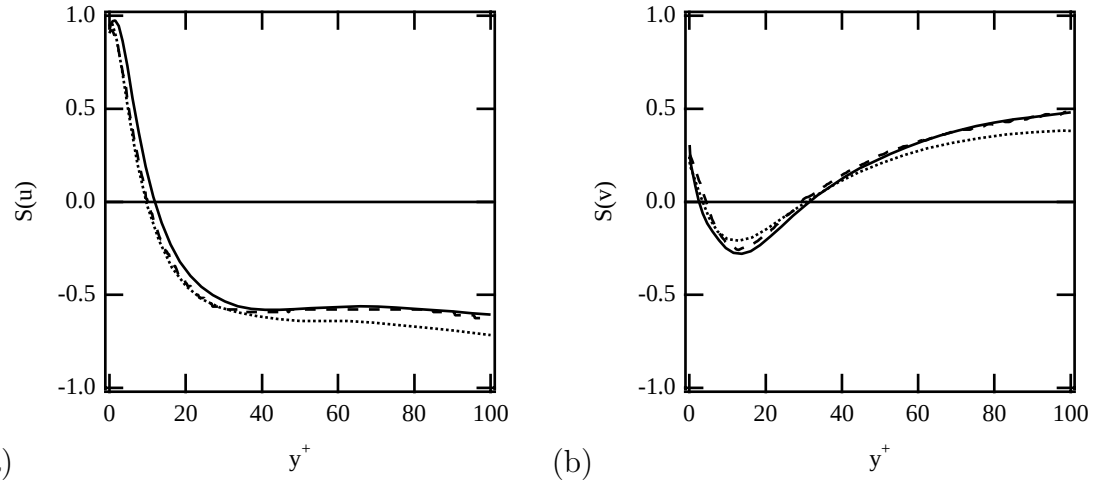

(a) (b)

Figure 3.8: Velocity skewness factors. —— DNS5; ····· LES7; – – – – Kim *et al.* (1987). (a) u (b) v.

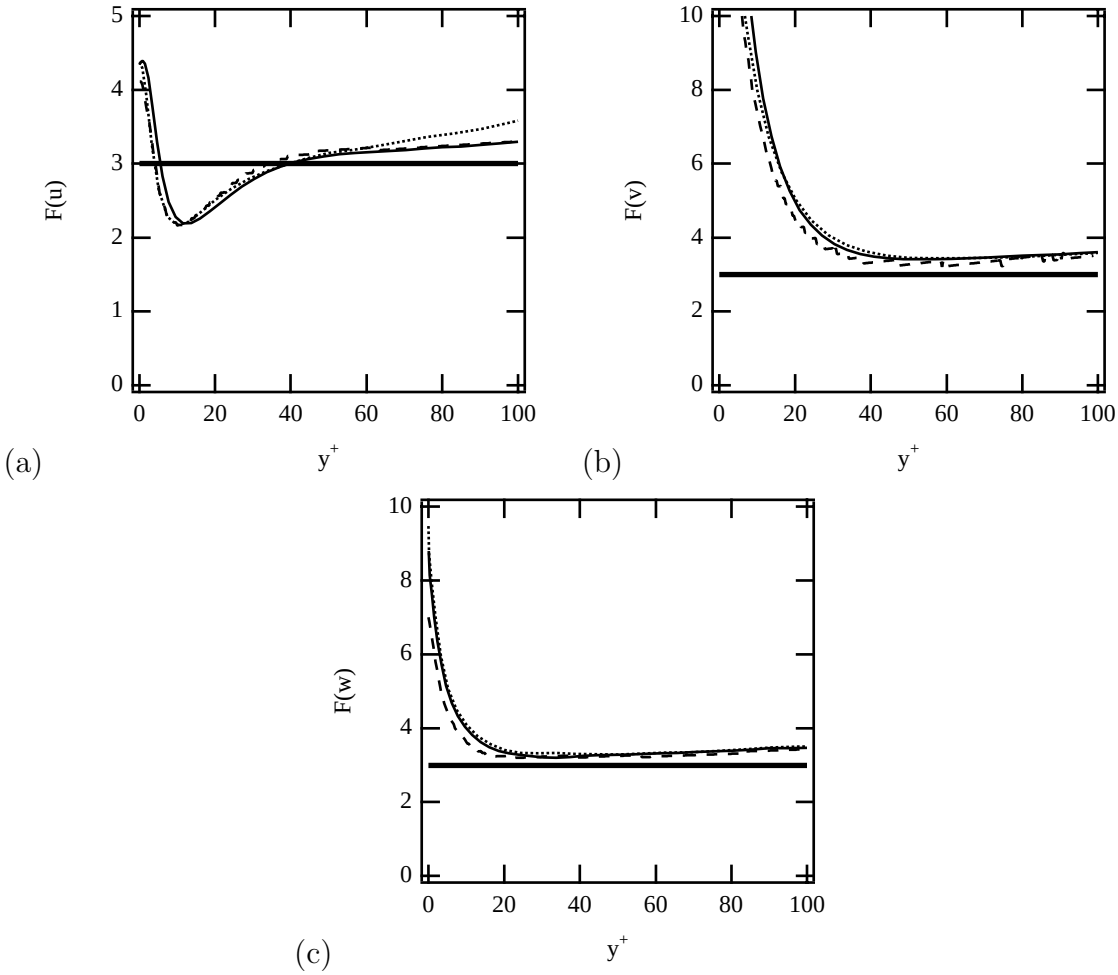

Figure 3.9: Velocity kurtosis. —— DNS5; ..... LES7; – – – – Kim *et al.* (1987). (a) u (b) v (c) w.

Figure 3.8 shows very good agreement between DNS5, LES7 and the DNS of Kim *et al.* (1987). The skewness factor for w is very close to zero, as required by spanwise symmetry, and is not shown.

The fourth moment of the probability distribution is the kurtosis or flatness factor, F, which was computed directly from the velocity fields,

$$F_i = \frac{\langle u_i^4 \rangle}{\langle u_i^2 \rangle^2}. \tag{3.1.5}$$

The kurtosis is a measure of the probability of high amplitude fluctuations. Figure 3.9 shows the the kurtosis distributions for the three velocity components. The

kurtosis value for a normal distribution ($F = 3$), is shown for comparison. The kurtosis for u is relatively near to 3, whereas the distributions for v and w are very large near the wall, but converge to values near 3 further from the wall. The very high values near the wall indicate processes which have very large and infrequent excursions from the local r.m.s.. The comparison between DNS5, LES7 and Kim *et al.* (1987) is very good.

Spectra

Since one of the objectives of this work is to relate the velocity fields to the wall pressures, in wavenumber space, validation of the velocity spectra is important. The spectra of turbulence has three ranges [see *e.g.*, Bradshaw (1971)]. First, the "energy-containing" range which contains the largest eddies, and is dependent upon the geometry, not upon viscosity. Second, a "dissipating" range which contains the smallest eddies and is dominated by viscosity; if there is a large enough wavenumber separation between the dissipating and energy-containing ranges (*i.e.*, the Reynolds number is high enough), the turbulence in the dissipating range may be isotropic and universal, *i.e.*, independent of the anisoptropic turbulence in the energy-containing range. Third, there may exist an "inertial subrange" between the energy-containing and dissipating ranges; the spectra in the inertial subrange decays as $k^{-5/3}$. Velocity spectra were computed for many wall-normal locations for both LES7 and DNS5. The spectra were averaged over approximately 50 realizations and normalized by $u_\tau^2 \delta$. Only spectra from $y^+ = 5$ and $y^+ = 150$ will be shown as these are the same locations shown in Kim *et al.* (1987).

Figures 3.10 through 3.13 show that the streamwise and spanwise spectra of the turbulent velocity fluctuations compare very well with those of Kim *et*

al. (1987). LES7 compares very well with DNS5, although for $y^+ = 150$ there is some attenuation in LES7 at the highest spanwise wavenumbers. Figure 3.10 shows that for the simulations, the region with a $k_x^{-5/3}$ decay rate is negligible, which is expected for low Reynolds number flows. At high wavenumbers the decay-rates increase with wavenumber, indicative of well resolved simulations (under-resolution would result in a an energy build-up in the highest wavenumbers). The dynamic SGS model depends on resolved velocity field information between the grid filter $\overline{\Delta}$ and the test filter $\widehat{\Delta}$. In the present LES, $\widehat{\Delta} = 2\overline{\Delta}$, which gives a streamwise wavenumber cutoff due to $\widehat{\Delta}$ of $k_x\delta = 6$. Figure 3.10 shows that the range $6 \leq k_x\delta < 12$ is in the dissipating range (i.e. at wavenumbers higher than where $k_x^{-5/3}$ decay rate is located). The spanwise spectra of u has a peak which corresponds to a wavelength of about 100 wall units which is about the expected spacing for low- and high- speed streaks. The peak in the spanwise spectra of v corresponds to a wavelength of about 60 wall units which could be due to streamwise vortices. The velocity spectra, in terms of the wall pressure source terms, will be explored in depth in Chapter 5.

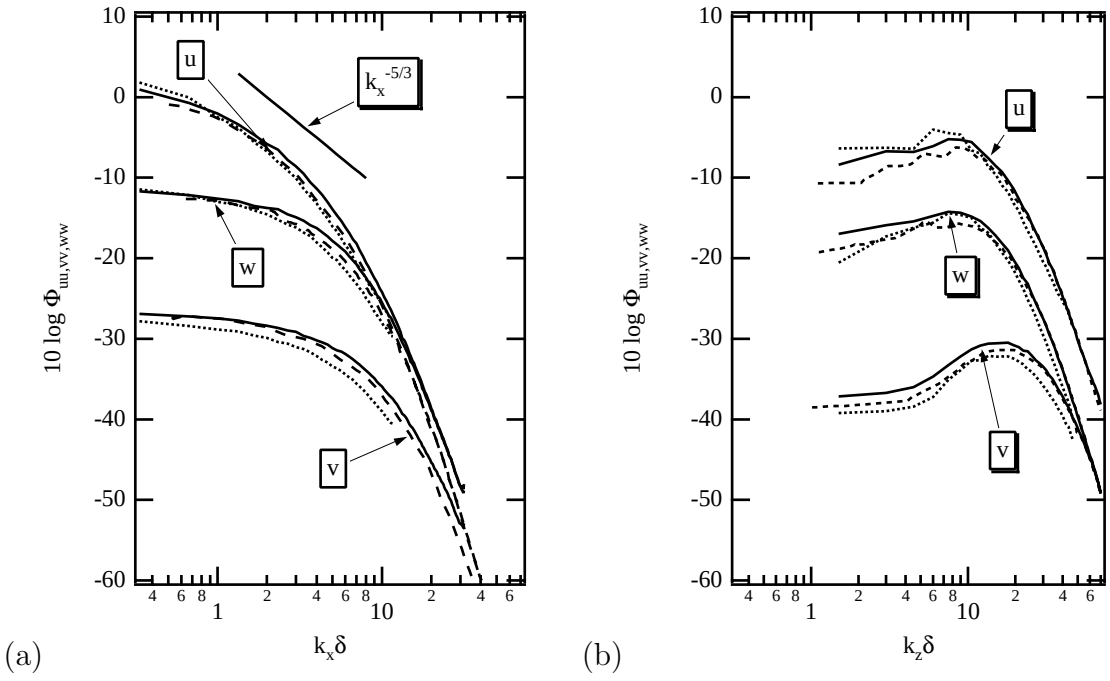

Figure 3.10: Velocity spectra at $y^+ = 5$. —— DNS5; ····· LES7; – – – – Kim *et al.* (1987). (a) Streamwise, (b) spanwise.

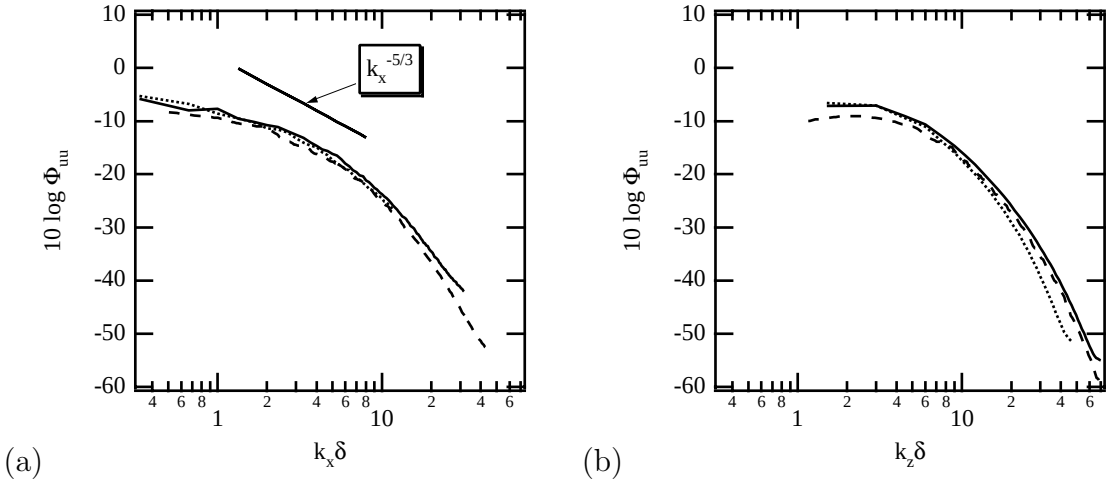

Figure 3.11: Spectra of u at $y^+ = 150$. —— DNS5; ····· LES7; – – – – Kim *et al.* (1987). (a) Streamwise, (b) spanwise.

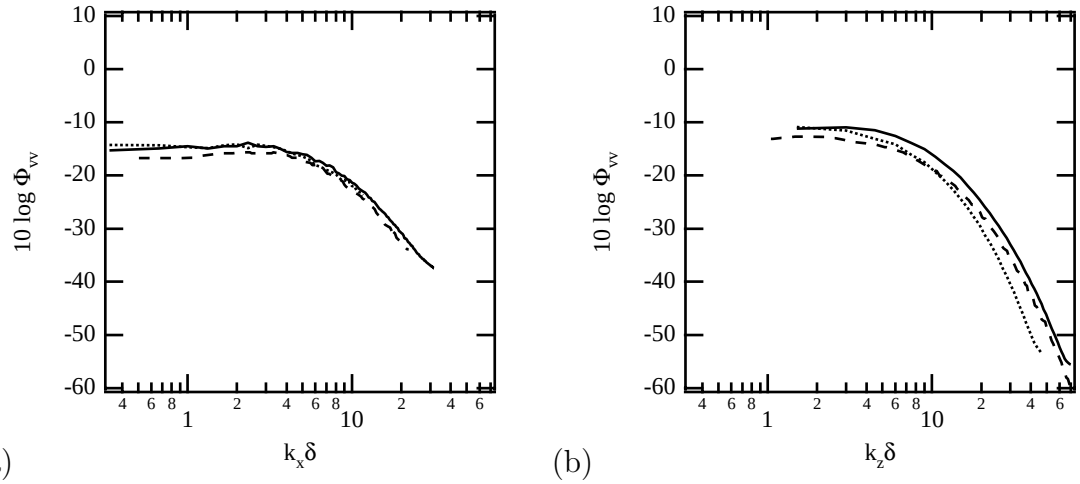

Figure 3.12: Spectra of v at $y^+ = 150$. —— DNS5; ····· LES7; – – – – Kim *et al.* (1987). (a) Streamwise, (b) spanwise.

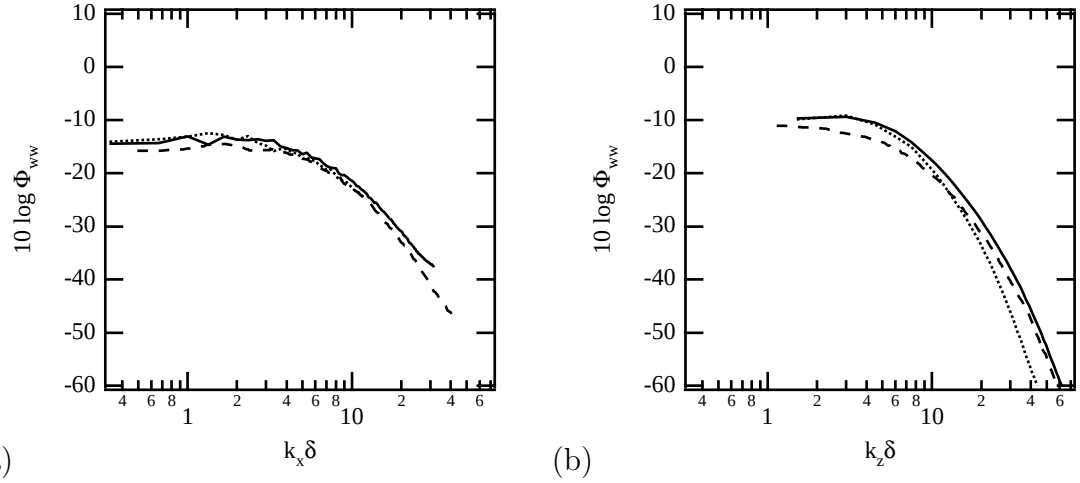

Figure 3.13: Spectra of w at $y^+ = 150$. —— DNS5; ····· LES7; – – – – Kim *et al.* (1987). (a) Streamwise, (b) spanwise.

3.2 Wall-pressure fields

In this section we will show the statistics and wavenumber-frequency spectra from multiple turbulence simulations. We will also describe how the spectra were computed.

Simulation	m.s.	Skew	Kurtosis
LES7	2.05	-0.06	5.37
DNS5	2.49	-0.10	5.23

Table II: Statistics for wall pressure from turbulence simulations. The m.s. values have bee normalized by τ_w^2,

Statistics of wall pressure

Table II is a tabulation of the wall pressure statistics. All the mean-square (m.s.) values are between 2 and 3, close to those computed by Kim *et al.* (1987) and Kim (1989). Handler (1984) obtained a value of 11 on a coarse grid ($\Delta x^+ = 31$) DNS, while Moin and Kim (1982) obtained 4.2 on a short box ($L_x = 2\pi\delta$) LES. The values presented here are much lower than those obtained from experiments conducted at much higher Reynolds numbers. For instance, Farabee and Casarella (1991) for a boundary layer flow at $Re_\tau = 1535$ obtained m.s. values of about 9. Singer (1996) obtains a value of 7.5 for a simulated boundary layer flow with $Re_\tau \approx 1000$. However, they are consistent with the trend, shown by Farabee and Casarella (1991), of decreasing m.s. as Re_τ decreases.

The skewness is an indicator of the asymmetry of high amplitude fluctuations. While it has been shown that the skewness of the turbulent pressure fluctuations is negative within the flow [see *e.g.*, Kim *et al.* (1987) and Kim (1989)] possibly due to negative pressure within the vortex cores, the skewness approaches very small negative values at the wall. It is reasonable that the skewness become less negative at the wall, because the probability of high amplitude positive pressure fluctuations, corresponding to sweep motions, increases as the wall is approached. Schewe (1983) showed that as transducer size increases (say for $d^+ > 100$), skewness approaches the Gaussian limit of 0; as transducer size decreases skewness approaches a value of approximately -0.2. As shown in Table II the skewness for

the simulations are small negative numbers.

The kurtosis shows that the wall pressure is a highly intermittent function where a large proportion (large compared with a Gaussian distribution) of the r.m.s. pressure comes from high amplitude fluctuations. Schewe (1983) showed values of kurtosis approaching 5 as the pressure transducer size decreased, while approaching the Gaussian limit of 3 as the size increased. However, one may also expect kurtosis to increase with increasing grid size. Piomelli (1993) explains that high kurtosis for velocities may be the result of not resolving the smaller scales of turbulence. These scales tend to be more isotropic than the larger scales, and if resolved would decrease the kurtosis. The kurtosis values of wall pressure are around 5 for all the simulations, which, based on the values of Δx^+, are higher than Schewe's trend. However, the kurtosis from the simulations do not show any dependency on streamwise grid size.

Spectra

Computation of spectra

The wavevector-frequency spectra shown in this Section were computed by the following methodology: the data were divided into $N_t = 384$ point segments spanning the period, T, with 50 percent overlap. This gave a reasonable compromise between number of spectra realizations and frequency resolution. A Hanning window was used on the time segments, while no windowing was necessary in the x and z directions in which the flow is periodic. The Hanning window was applied in time to the total, resolved pressure, $\bar{p}$, normalized by the long time average value

of τ_w,

$$\tilde{p}\,(x_i, z_j, t_l) = \bar{p}\,(x_i, z_j, t_l)\,\frac{1}{2}\left(1 - \cos\frac{2\pi l}{N_t}\right) \tag{3.2.6}$$

where $i = 1 \ldots N_x$, $j = 1 \ldots N_z$, and $l = 1 \ldots N_t$. A three-dimensional Fourier wavenumber-frequency transform of each time segment was taken and from that, an averaged spectral density was obtained from the mean of the spectral densities from the m overlapping segments

$$\Psi\,(i\Delta k_x, j\Delta k_z, l\Delta\omega) = \frac{1}{m}\sum_{s=1}^{m}\left(\hat{p}\,\hat{p}^*\right)_s . \tag{3.2.7}$$

Here $\hat{p}$ denote the Fourier coefficients of the pressure and $\hat{p}^*$ are their complex conjugates. The spectral density was computed for both top and bottom of the channel, resulting in $2m$ time segments

The three-dimensional spectral density should satisfy Parseval's identity

$$\frac{1}{L_x L_z T}\int_0^T\int_0^{L_z}\int_0^{L_x} p^2\;dx\;dz\;dt = \int_{-\infty}^{\infty}\int_{-\infty}^{\infty}\int_{-\infty}^{\infty}\Psi(k_x, k_z, \omega)\;d\omega\;dk_z\;dk_x \tag{3.2.8}$$

which, in discretized form, is given by

$$\frac{1}{N_x N_z N_t}\sum_{l=1}^{N_t}\sum_{j=1}^{N_z}\sum_{i=1}^{N_x} p^2\,(x_i, z_j, t_l) = \Delta\omega\;\Delta k_z\;\Delta k_x \sum_{l=1}^{N_t}\sum_{j=1}^{N_z}\sum_{i=1}^{N_x}\Psi\,(i\Delta k_x, j\Delta k_z, l\Delta\omega) \tag{3.2.9}$$

where the left hand side is the mean-square (m.s.) pressure. Since the pressure has been windowed in time, its spectral density does not satisfy (3.2.9) exactly; Ψ is then normalized to satisfy (3.2.9). The two-dimensional $k_x - \omega$ spectra is given by the integral over all the spanwise wavenumber modes, which, in discretized form, results in the summation over all the modes multiplied by Δk_z,

$$\Phi(i\Delta k_x, l\Delta\omega) = \Delta k_z \sum_{j=1}^{N_z}\Psi. \tag{3.2.10}$$

The two-dimensional spectral density extends over $l = 1 \ldots N_t$ frequency bins and $i = 1 \ldots N_x$ wavenumber bins and has the symmetry property

$$\Phi(i\Delta k_x, l\Delta\omega) = \Phi\left[(N_x - i + 2)\Delta k_x, (N_t - l + 2)\Delta\omega\right] \tag{3.2.11}$$

In the $k_x - \omega$ plots the wavenumber bins $N_x/2 + 2 \leq i \leq N_x$ have been translated to the bins $-N_x/2 + 1 \leq i \leq -1$; with this convention, a wave that is convecting downstream will have either ω or k_x negative. In the two-dimensional spectra plots, the convective ridge, representing energy convecting downstream, is shown in the negative k_x, positive ω quadrant.

DNS1 is the database used Choi and Moin (1990), which was reduced by Bruce Abraham of Naval Underwater Systems Command and presented here as well as in Chang *et al.* (1994). The DNS1 spectra were computed using the MATLAB* software package. The data were divided into four 512 point time segments with no overlap and the two-dimensional spectral density for each segment computed. This two-dimensional $k_x - \omega$ spectral density was then averaged over the $m = 4$ segments and over every other spanwise location:

$$\Phi(i\Delta k_x, l\Delta\omega) = \frac{2}{N_z} \sum_{\substack{j=1 \\ j \text{ even}}}^{N_z} \left[\frac{1}{m} \sum_{r=1}^{m} \Phi(i\Delta k_x, j\Delta k_z, l\Delta\omega, r)\right]. \tag{3.2.12}$$

Two-dimensional wall pressure spectra

One of the reasons for running the simulations was to study the fidelity of the wavenumber-frequency characteristics of the wall pressure fields, particularly in the subconvective wavenumber range†. Table III lists the number of grid points,

*MATLAB is a registered trademark of The MathWorks, Inc.

†The subconvective wavenumber range is the region of the wavenumber-frequency plane where $k_x \ll k_{xc}$ where $k_{xc} \equiv \omega/U_c$, is the location of the convective ridge; U_c is the convection velocity

Simulation	Grid Points $N_x \times N_y \times N_z$	Box Size $\frac{L_x}{\delta} \times \frac{L_y}{\delta} \times \frac{L_z}{\delta}$	Dealiasing
LES1	$48 \times 64 \times 64$	$4\pi \times 2 \times \frac{4\pi}{3}$	none
LES2	$48 \times 64 \times 64$	$4\pi \times 2 \times \frac{4\pi}{3}$	x
LES3	$48 \times 64 \times 64$	$4\pi \times 2 \times \frac{4\pi}{3}$	x, z
LES7	$72 \times 64 \times 64$	$6\pi \times 2 \times \frac{4\pi}{3}$	x, z
DNS1	$128 \times 129 \times 128$	$4\pi \times 2 \times \frac{4\pi}{3}$	x, z
DNS2	$64 \times 64 \times 64$	$\pi \times 2 \times \frac{4\pi}{3}$	none
DNS3	$192 \times 96 \times 96$	$6\pi \times 2 \times \frac{4\pi}{3}$	none
DNS5	$192 \times 96 \times 96$	$6\pi \times 2 \times \frac{4\pi}{3}$	x, z

Table III: Simulation designations and details

the box sizes and dealiasing used in the simulations. To understand why the various simulations were run, the two-dimensional wavenumber-frequency spectra of wall pressure will be shown, since it was found that numerical issues (namely, aliasing errors in the pseudo-spectral method as well as grid resolution) affected the behavior of the spectra, particularly in the subconvective wavenumber range.

LES1 and LES2 were run on a $4\pi\delta$ streamwise box size, whereas LES7 was run on a $6\pi\delta$ streamwise box size. Figure 3.14 shows plots of the wavenumber-frequency spectra of wall pressure. The wavenumber-frequency spectra is displayed as contours of

$$10 \log \frac{\Phi(i\Delta k_x, l\Delta\omega)}{\tau_w^2 \delta^2 / u_\tau}. \tag{3.2.13}$$

Figure 3.14(a) the wavenumber-frequency spectra from LES1 has energy in the positive-k_x quadrant which was shown by Chang *et al.* (1994) to be due to aliased energy. LES2 and LES7 were run with dealiasing in x, and $x - z$, respectively. As can be seen from Figure 3.14(b) and Figure 3.15, the energy in the positive-k_x quadrant is significantly reduced by dealiasing.

The wavenumber-frequency spectra for DNS1 are shown in Figure 3.16. The

and ω denotes the radian frequency.

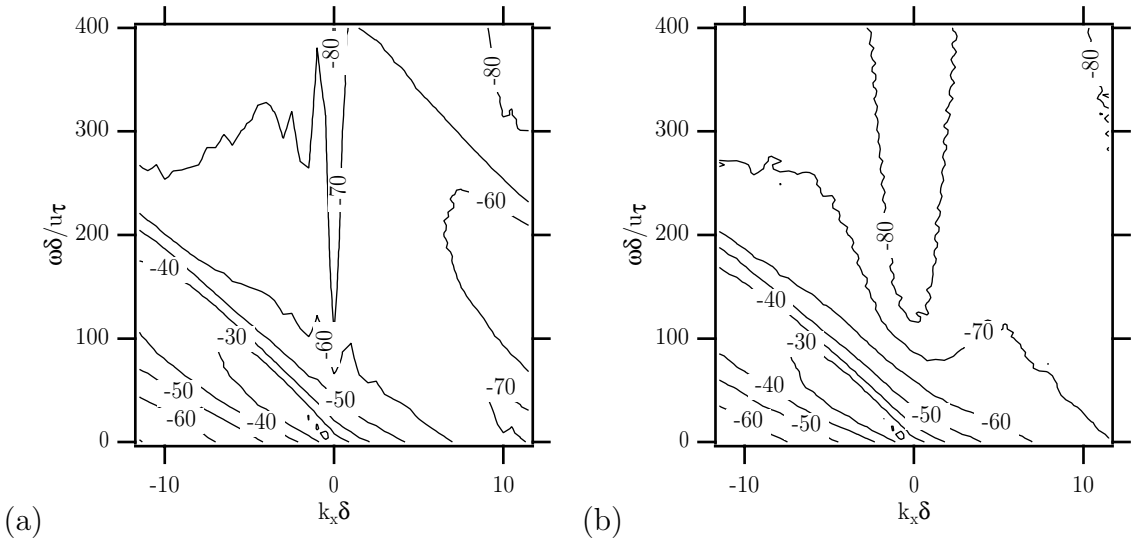

Figure 3.14: $k_x - \omega$ contour plots of wall pressure spectra from (a) LES1 and (b) LES2.

high energy build-up around $k_x\delta = 0$ and the high subconvective-wavenumber energy levels could not be explained by Choi and Moin (1990). DNS2 was run on a very short box ($2\pi\delta$) with a high grid density to see the effect of grid resolution on the wavenumber-frequency characteristics. As can be seen from Figure 3.17, DNS2 also presents an energy build-up in the positive-k_x quadrant, and high energy levels in the subconvective wavenumber range. DNS3 was run on a $6\pi\delta$ box without dealiasing; as Figure 3.18 shows, it has energy in the positive-k_x quadrant, due to aliasing, as well as an energy buildup in the subconvective wavenumber range. DNS5 was dealiased in both x and z, and as shown in Figure 3.19, it has no energy in the positive-k_x quadrant (except for that related to the convective ridge) and shows no energy buildup in the subconvective wavenumber range.

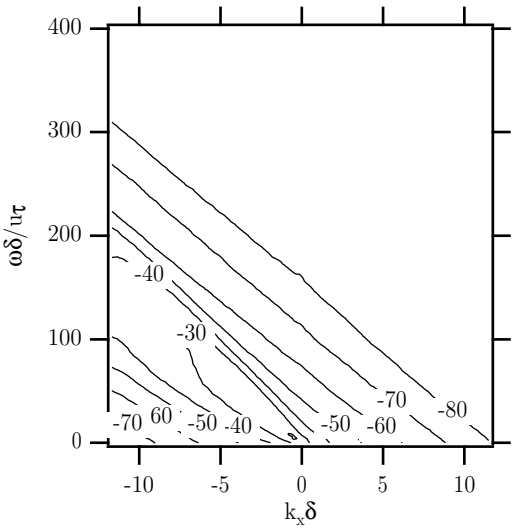

Figure 3.15: $k_x - \omega$ contour plot of wall pressure spectra from LES7.

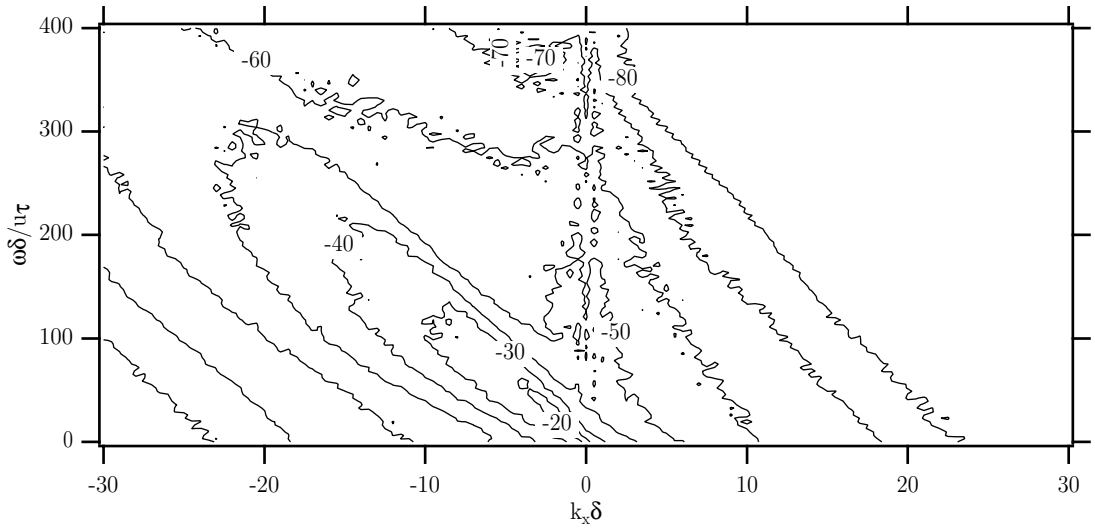

Figure 3.16: $k_x - \omega$ contour plot of wall pressure spectra from DNS1.

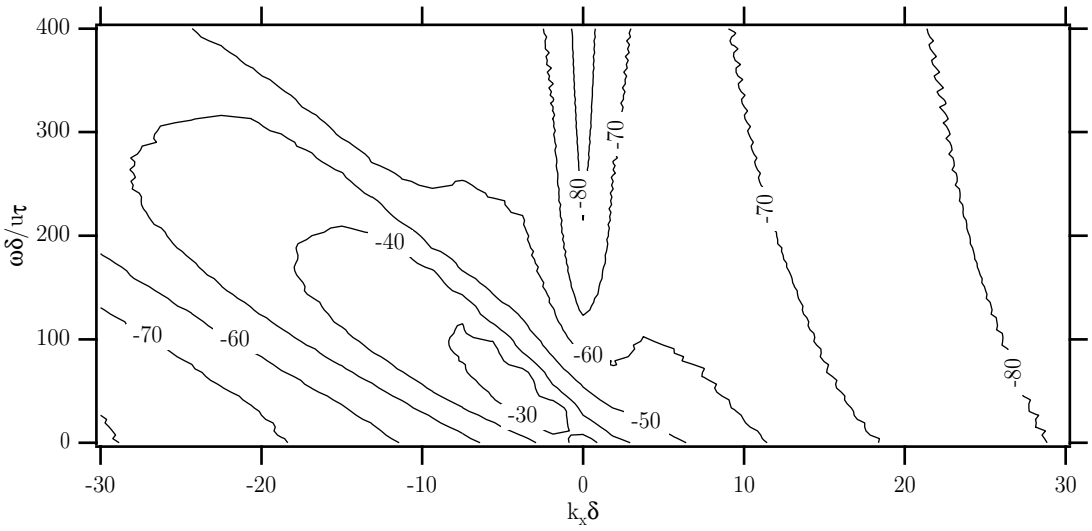

Figure 3.17: $k_x - \omega$ contour plot of wall pressure spectra from DNS2.

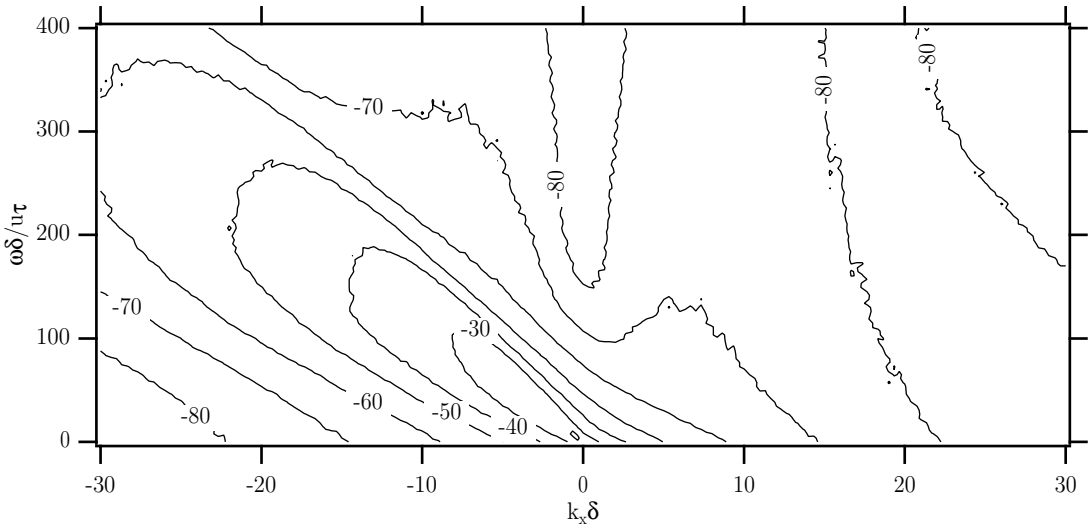

Figure 3.18: $k_x - \omega$ contour plot of wall pressure spectra from DNS3.

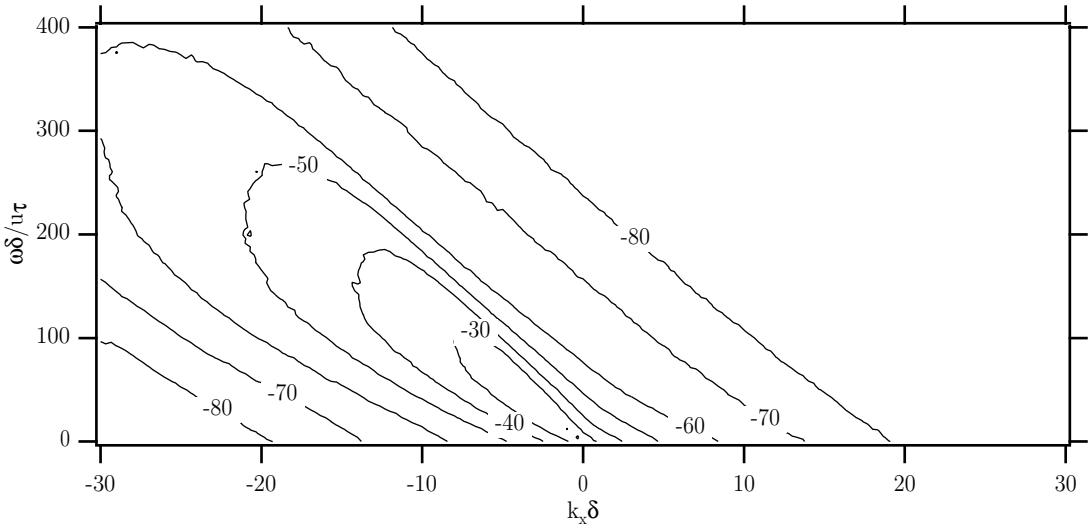

Figure 3.19: $k_x - \omega$ contour plot of wall pressure spectra from DNS5.

Chapter 4

Partial Wall-Pressures

The objective of this chapter is to determine which velocity source terms are most important for the generation of wall pressure, and where in the channel these sources are acting. In order to do this, partial wall pressures, *i.e.*, the contributions due to individual source terms at various horizontal layers of the channel, have been computed and are compared in planar wavenumber space. Partial pressures are the product of the wall pressure Green's function and the individual source terms, integrated over vertical regions, corresponding to various regions of the channel. Comparisons of the partial pressures show which sources are most significant, while partial pressures are combined and compared to the total pressure to determine which subset of sources is necessary to reconstitute the total pressure.

Section 4.1 describes how the partial pressures are computed; Section 4.2 shows the relative importance of the Stokes' pressures; Section 4.3 compares the total, TT and MS partial pressures; Section 4.4 compares the partial pressures due to individual terms and regions; Section 4.5 summarizes the findings.

Region	Limits	Description
1	$0 \leq y^+ < 5$	Viscous shear-layer
2	$5 \leq y^+ < 30$	Buffer layer
3	$30 \leq y^+ < 180$	Logarithmic region
4	$180 \leq y^+ < 360$	Upper channel

Table I: Regions of the channel.

4.1 Computation of partial pressures

Since the wall pressure depends on sources distributed throughout the entire flow domain it is difficult to ascertain where in the boundary layer the dominant sources are located. One advantage of turbulence simulations is that they generate three-dimensional velocity fields from which all the source terms can be computed. In this investigation the product of the sources by the Green's function, which is the true measure of the influence of the sources on the wall pressure, has been computed. The channel was divided into four regions (Table I) roughly corresponding to the viscous shear-layer, buffer and logarithmic regions, and the upper part of the channel. The contribution of the source terms was integrated over each region. It is assumed that the partial pressures are evaluated at the lower channel wall, even though symmetry has been used in the data reduction and partial pressures have been averaged over both the upper and lower channel walls. The lower wall will be referred to as the "near-wall," the upper wall, the "far-wall."

The source terms, $T_{ij}(x, y, z)$, were computed from 110 realizations of DNS5 data, in three-dimensional physical space, using the 2/3 rule to eliminate aliasing errors. Nine terms were computed: the six TT terms, their sum, the MS term and the total. They were then Fourier-transformed to yield their complex coefficients

in planar wavenumber space, $\widehat{T_{ij}}(\mathbf{K}, y)$. The integral of the product of the source terms and Green's function

$$\widehat{p}_{ij}(\mathbf{K}, Rr) = \int_{\eta_1(r)}^{\eta_2(r)} \widehat{T}_{ij}(\mathbf{K}, \eta) G(K, y = -1, \eta) d\eta. \tag{4.1.1}$$

(where $\eta_1(r)$ and $\eta_2(r)$ are the lower and upper integration limits for each region, and r denotes the vertical regions described in Table I) was then computed using Chebychev integration. The complex partial pressure spectrum due to the source term T_{ij} from region r is denoted by $\widehat{p}(\mathbf{K}, Rr)$. The complex spectra for the various terms and regions could then be combined; *e.g.*, the partial pressure due to T_{12} from regions 2, 3 and 4 is

$$\widehat{p}_{12}^{TT}(\mathbf{K}, R234) = \widehat{p}_{12}^{TT}(\mathbf{K}, R2) + \widehat{p}_{12}^{TT}(\mathbf{K}, R3) + \widehat{p}_{12}^{TT}(\mathbf{K}, R4). \tag{4.1.2}$$

The total TT partial pressure is the summation of all the TT partial pressures,

$$\widehat{p}^{TT}(\mathbf{K}, Rr) = \sum_{i=1}^{3} \sum_{j=1}^{3} \widehat{p}_{ij}^{TT}(\mathbf{K}, Rr), \tag{4.1.3}$$

and the total partial pressure is

$$\widehat{p}^{tot}(\mathbf{K}, Rr) = \widehat{p}^{MS}(\mathbf{K}, Rr) + \widehat{p}^{TT}(\mathbf{K}, Rr). \tag{4.1.4}$$

The total pressure is $\widehat{p}^{tot}(\mathbf{K}, R1234)$. The magnitudes of the complex spectra were computed by

$$\Pi(\mathbf{K}, Rr) = \widehat{p}_{ij}^{*}(\mathbf{K}, Rr) \widehat{p}_{ij}(\mathbf{K}, Rr) \qquad \text{(no summation)} \tag{4.1.5}$$

(where $\widehat{f}^*$ is the complex conjugate of $\widehat{f}$), and averaged over multiple realizations. It should be noted that the partial pressures are defined by the integral over all frequencies,

$$\Pi(\mathbf{K}, Rr) = \int_{-\infty}^{\infty} \Pi(\mathbf{K}, \omega, Rr) d\omega \tag{4.1.6}$$

where $\Pi(\mathbf{K}, \omega, Rr)$ is the partial pressure in four-space. The one-dimensional spectra were obtained by the integrations

$$\pi(k_x, Rr) = \int_{-\infty}^{\infty} \Pi(\mathbf{K}, Rr) dk_z \tag{4.1.7}$$

and

$$\pi(k_z, Rr) = \int_{-\infty}^{\infty} \Pi(\mathbf{K}, Rr) dk_x \tag{4.1.8}$$

The one-dimensional spectra were normalized by $\tau_w^2 \delta$.

4.2 Stokes Pressure

The partial pressure due to the boundary terms (2.6.17) is called the Stokes pressure [Kim (1989)]. Kraichnan (1956) estimated that the Stokes pressure should be much smaller than the total (due to velocity field sources) pressure. Kim (1989), using DNS data from a channel flow, computed the r.m.s. of the Stokes wall pressure and found it to be about 1/10 of the total pressure. In his analytical model, Chase (1980) assumed it was small and neglected it. In this subsection we will show the wavenumber distribution of the Stokes pressure and compare it to the total pressure.

The pressure gradients in (2.6.17) can be expressed in terms of velocities as a result of the wall normal momentum equation evaluated at the walls,

$$\left.\frac{\partial p}{\partial y}\right|_{y=\pm 1} = \frac{1}{Re} \left.\frac{\partial^2 v}{\partial y^2}\right|_{y=1}. \tag{4.2.9}$$

In planar wavespace, the far-wall boundary term, evaluated at the near-wall, becomes

$$B_+(\mathbf{K}, y=-1) = \frac{1}{K \sinh(2K)} \frac{1}{Re} \frac{\partial^2 \widehat{v}}{\partial \eta^2}(\mathbf{K}, \eta = 1) \tag{4.2.10}$$

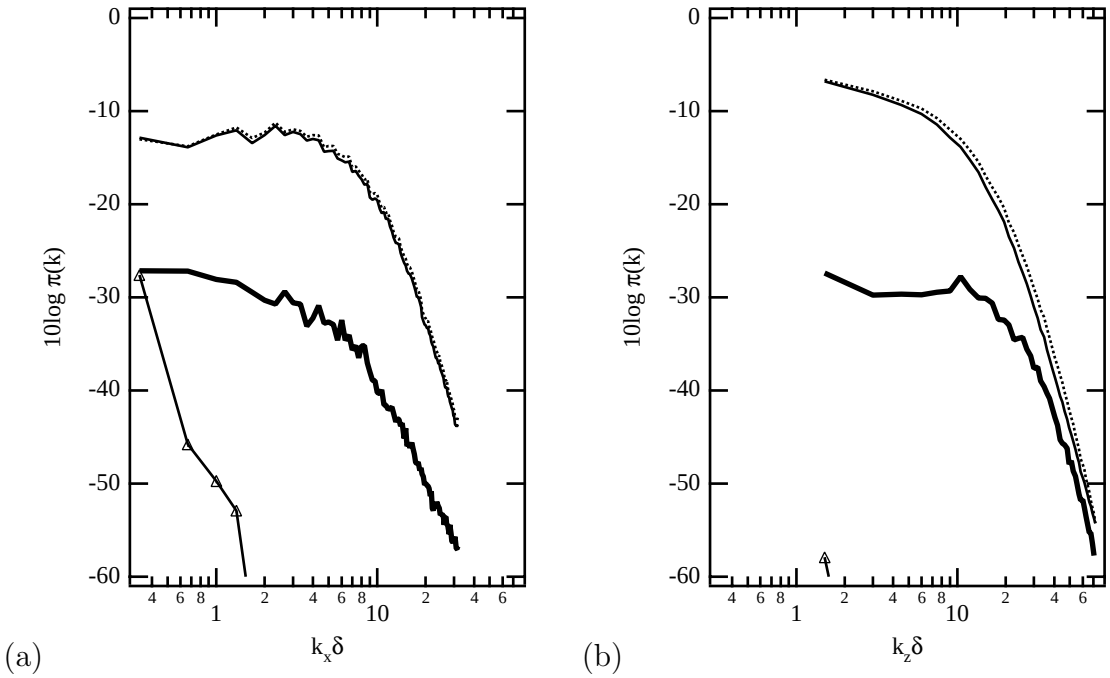

Figure 4.1: Partial near-wall wall pressure due to boundary condition terms and total pressure with and without boundary condition terms; ▬ : near-wall boundary condition term; △ : far-wall boundary condition term; —— : $\hat{p}_{tot}$ with boundary condition terms; ····· : $\hat{p}_{tot}$ without boundary condition terms; (a) k_x (b) k_z.

and the near-wall boundary term, evaluated at the near-wall, becomes

$$B_{-}(\mathbf{K}, y=-1) = \frac{1}{K\tanh(2K)}\frac{1}{Re}\frac{\partial^2 \widehat{v}}{\partial \eta^2}(\mathbf{K}, \eta=-1). \tag{4.2.11}$$

The magnitudes of the complex spectra (4.2.10) and (4.2.11), were taken and then integrated appropriately to obtain either the streamwise or spanwise one-dimensional spectra. Figure 4.1 shows the one-dimensional spectra for the near- and far-wall boundary terms computed from 11 widely spaced (in time) realizations of DNS5. The streamwise spectra show the near-wall term is about $15-20$ dB less than the total pressure. The difference between the total pressure with and without the boundary terms is less than 1 dB throughout the entire streamwise wavenumber range. The far-wall boundary term is about 18 dB lower than the

total pressure, at the lowest wavenumber, and then falls off rapidly. The spanwise spectra shows that the near-wall term comes to within $2-3$ dB of the total pressure at the high wavenumbers. The difference between the total pressure with and without the boundary term is as great as 2 dB. The conclusion that can be drawn from this is that, for the wall pressure at the near-wall, the far-wall boundary term is insignificant, while the near-wall boundary term has a small, but discernible affect on the near-wall wall pressure spectra. For all practical purposes, neglecting the Stokes pressure is a reasonable assumption.

4.3 Total, MS and TT partial pressures

All regions

It was first estimated by Kraichnan (1956) that the mean-square of the MS pressure should be approximately 68 times larger than the TT pressure. Using DNS data however, Kim (1989) found that the one-dimensional spectra of the MS and TT pressures were the same order of magnitude throughout the wavenumber range. One reason that Kraichnan's (1956) estimate does not compare well with more recent data may be because it was dependent upon estimates of fluctuating velocity correlation lengths obtained for homogenous, isotropic turbulence.

Figure 4.2 shows the total, MS and TT pressures summed over all regions, $\pi_{ij}(k_x, R1234)$ and $\pi_{ij}(k_z, R1234)$. Consistent with the results of Kim (1989), the MS and TT terms are of the same order of magnitude throughout the wavenumber range. The MS term is larger than the TT term throughout the streamwise wavenumber range while in the spanwise spectra, for $k_z\delta > 25$, the TT term be-

comes larger.

The low-wavenumber range of the streamwise spectra is fairly flat, with a peak at $k_x\delta \simeq 3$. Farabee and Casarella (1991) used u_τ, τ_w and δ (where δ is the boundary layer thickness) to normalize the frequency spectra, and found that, for a range of Reynolds numbers, the spectra collapsed in a mid-frequency range. The peak of their spectra was at $\omega u_\tau/\delta \approx 50$. Assuming a convection velocity $U_c \approx 13u_\tau$ (based on the location of the convective ridge in the $k_x - \omega$ plane) the spectral peak they obtained corresponds to $k_x\delta \simeq 4$, in good agreement with the data presented here.

The total, MS and TT pressures do not appear to have significant regions of k_x^{-1} or k_z^{-1} behavior predicted by Bradshaw (1967) for the overlap region. This is due to Reynolds number effects; Farabee and Casarella (1991) define the overlap region as

$$100 \leq \omega\delta/u_\tau \leq 0.30Re_\tau \tag{4.3.12}$$

which for $Re_\tau = 180$ and $U_c \approx 13u_\tau$, gives a lower limit $k_x\delta \approx 8$ and an upper limit $k_x\delta \approx 4$.

Both the streamwise and spanwise spectra have wavenumber ranges with a k^{-5} decay rate. This range has been shown to scale with inner variables [Farabee and Casarella (1991), Keith *et al.* (1992), Olivero-Bally (1993), Chang *et al.* (1994)] indicating that it is due to sources in a region that scales accordingly, such as the viscous shear-layer. The MS spanwise spectra has a significant range of k_z^{-5} whereas the TT spanwise spectra only passes through a k_z^{-5} rolloff. This will be investigated further in the next subsection.

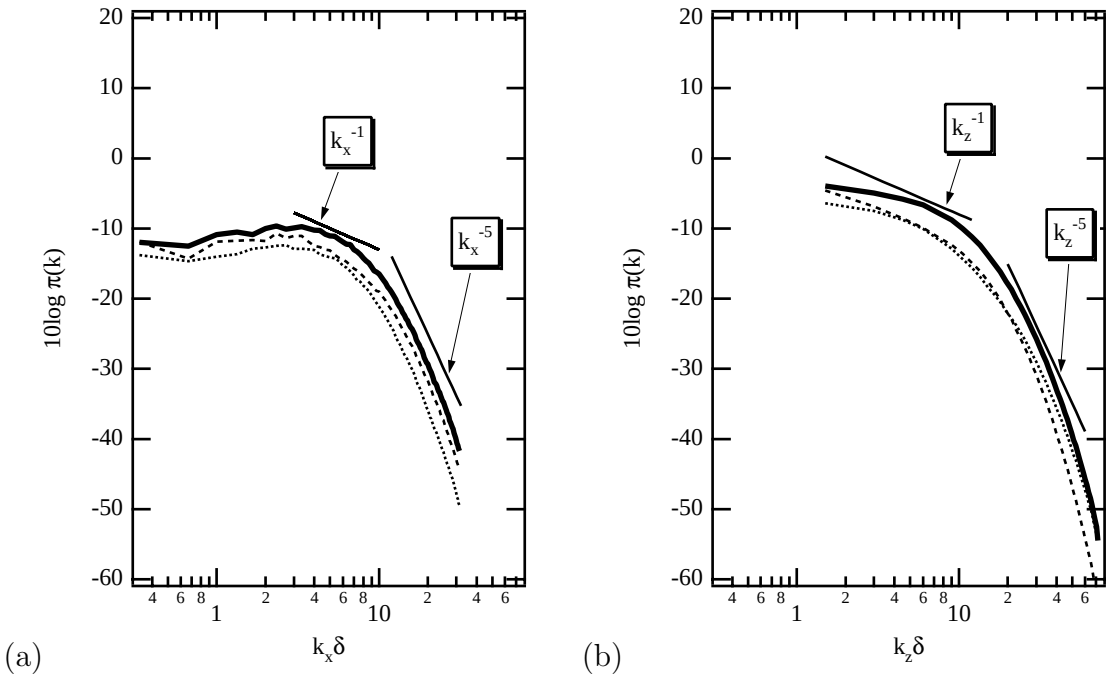

Figure 4.2: Total, MS and TT one-dimensional pressure spectra. ——— π^{tot}; ····· π^{TT}; - - - - - - π^{MS}. (a) Streamwise, (b) spanwise.

Contribution of the regions

To determine where in the boundary layer the MS and TT pressures are generated, we will now examine the partial pressures from the four regions.

Total partial pressures

The spectra of the contribution to the total pressure from each of the four regions, $\pi^{tot}(Rr)$, and for all four regions combined, $\pi^{tot}(R1234)$, are shown in Figure 4.3. For $k_x\delta > 5$ and $k_z\delta \leq 50$ the buffer layer accounts for most of the total pressure spectrum; for $k_x\delta > 55$, however, the viscous shear-layer becomes the most important contribution. The high-wavenumber behavior of the viscous shear-layer is consistent with the notion that the near-wall regions are responsible for the higher-wavenumber pressure, since the high-wavenumber contributions to the pressure

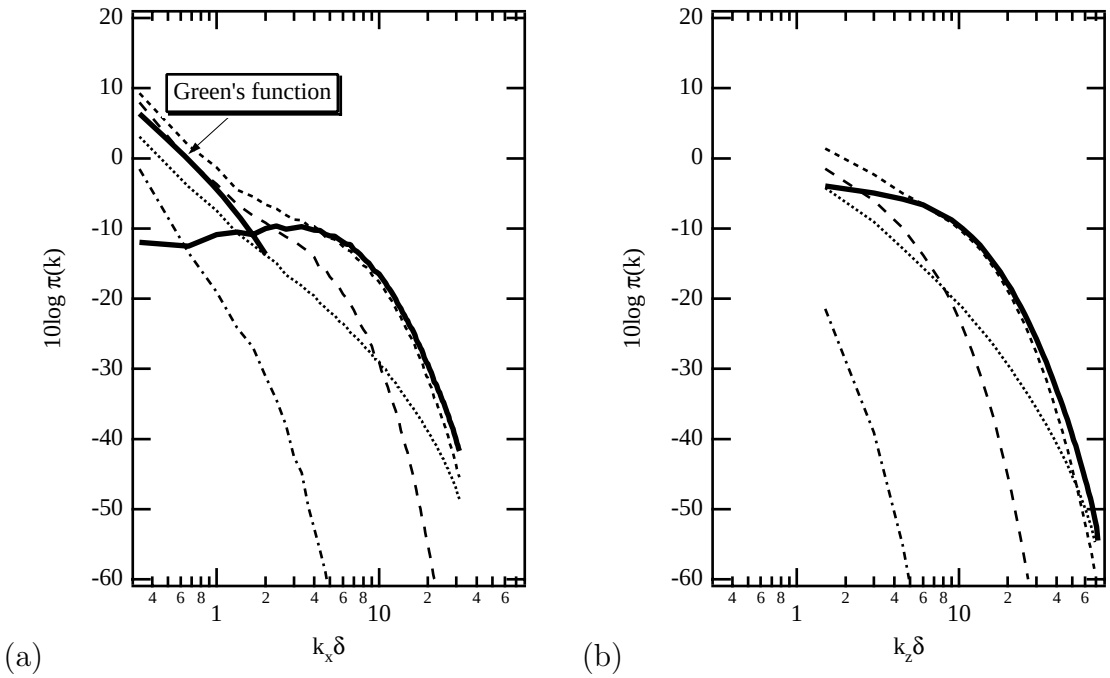

Figure 4.3: One-dimensional spectra of the total pressure for the various regions. ——— All regions (R1234); ····· viscous shear-layer (R1); - - - - - - buffer layer(R2); – – – – logarithmic region(R3); –·– upper channel(R4). (a) Streamwise, (b) spanwise.

from regions further from the wall are strongly attenuated by the Green's function. At low wavenumbers ($k_x\delta \leq 5, k_z\delta \leq 5$) the partial pressures show very little resemblance to $\pi^{tot}(R1234)$. There, the total source term T^{tot}, shown in Figure 4.4 at several y locations, is nearly flat, and $\pi^{tot}(Rr)$ must have the same slope as the Green's function, as shown in Figure 4.3.

MS partial pressures

In Figure 4.5 the spectra of the MS pressure are shown for each of the four regions. Except at the lowest wavenumbers, $\pi^{MS}(k_x)$ is due primarily to buffer layer sources. This is also true for $\pi^{MS}(k_z)$, except at the highest wavenumbers ($k_z\delta > 50$), where the viscous shear-layer contributions become significant. It has been conjectured

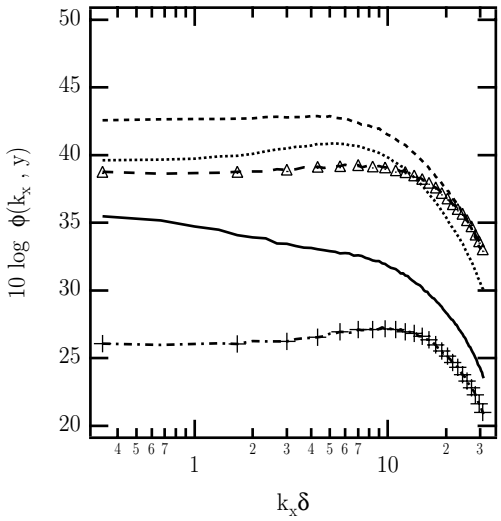

Figure 4.4: Streamwise wavenumber spectra of total source terms at selected locations. —— $y^+ = 5$; ····· $y^+ = 11$; - - - - - $y^+ = 21$; △ $y^+ = 49$; + $y^+ = 145$.

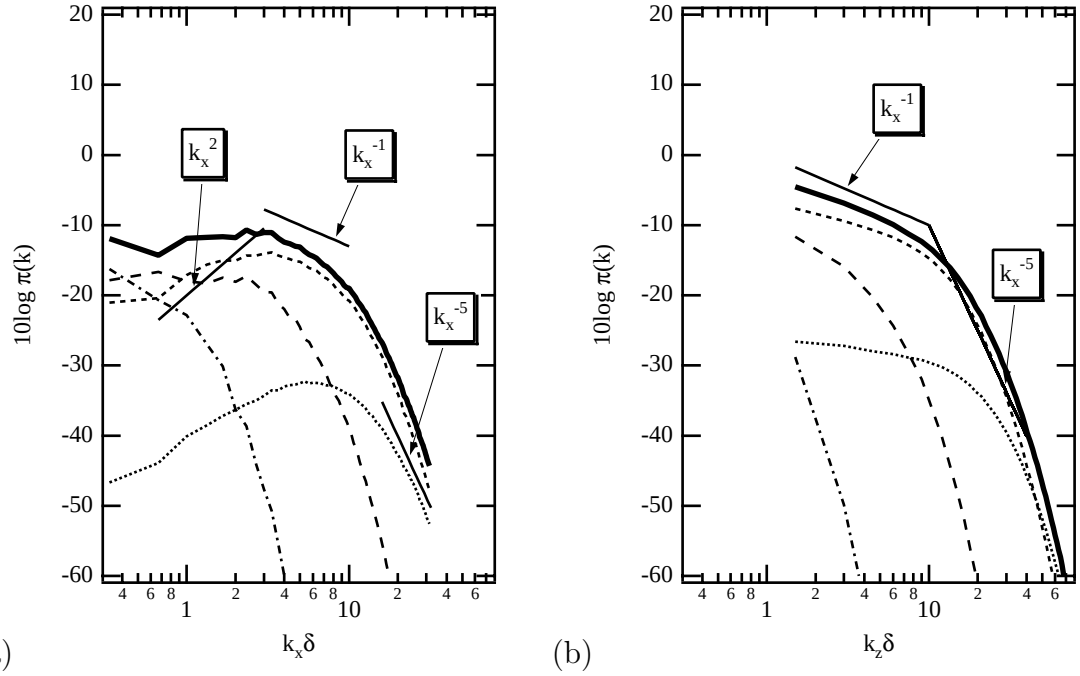

Figure 4.5: One-dimensional spectra of the MS pressure for the various regions. —— All regions (R1234); ····· viscous shear-layer (R1); - - - - - buffer layer (R2); – – – – logarithmic region (R3); –·– upper channel (R4). (a) Streamwise, (b) spanwise.

(*e.g.*, by Blake (1986), p. 518) that at the low wavenumbers the MS sources follow a k^2 behavior. Figure 4.5(a) shows that in the low wavenumbers the partial pressure from the buffer layer has a k^2 slope. The figure also shows that the buffer layer also has a very short region with a k^{-1} slope, which is consistent with Bradshaw's (1967) prediction. The partial pressure from the viscous shear-layer has a range of k^{-5} behavior, which confirms that the approximations involved in MS source term modelling in the viscous shear-layer [Blake (1986)] are essentially correct. However, as can be seen, in the k^{-5} wavenumber range, the sources from the buffer layer are dominant, rather than those from the viscous shear-layer. It can also be seen, in Figure 4.5(b), that the spanwise partial pressure spectra due to the buffer layer has wavenumber ranges that decay as k^{-1} and k^{-5}.

Now that we know which regions dominate the MS partial pressure it is of interest to see which combinations of regions are necessary to obtain the total MS partial pressure. This is particularly of interest for modelling purposes, since it would give indications as to which minimum subset of regions is necessary to model the MS pressure. Figure 4.6 shows the MS partial pressures for combinations of the regions. For discussion purposes, wavenumber ranges are defined in Table II. In the intermediate and high streamwise and spanwise wavenumbers, contributions from the viscous shear-layer and buffer layer are necessary to reconstitute the MS partial pressure. This confirms the dominance of the buffer layer and refutes the notion that only the viscous shear-layer sources are important at the high wavenumbers. In the lowest and low wavenumber range only the buffer layer and logarithmic region sources are necessary.

TT partial pressures

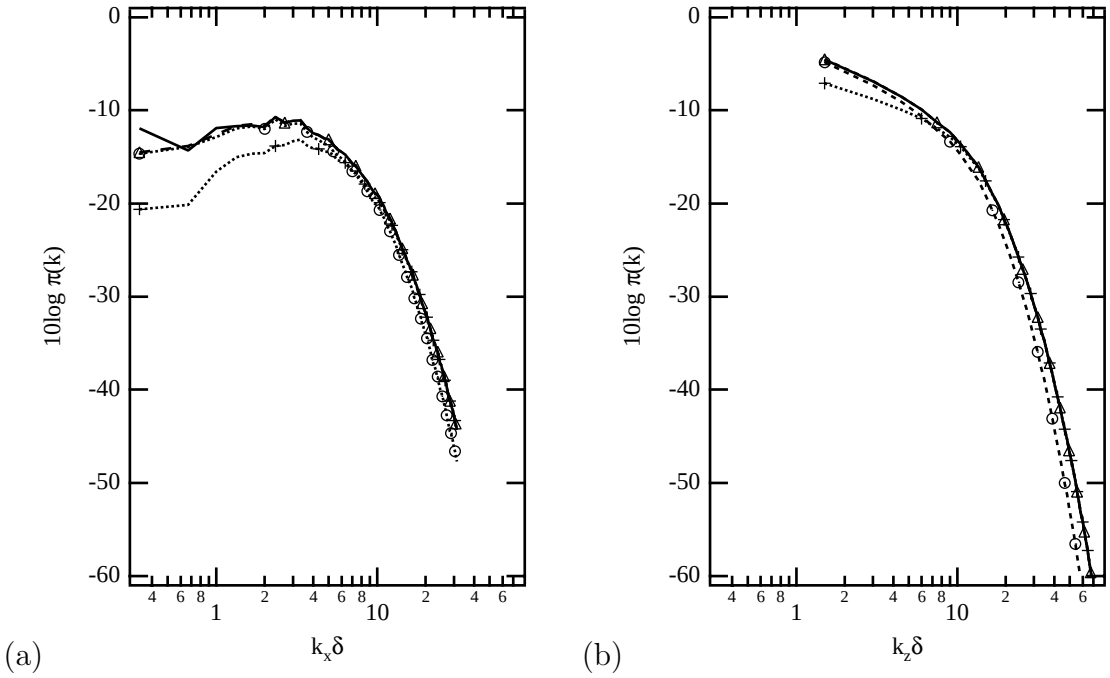

Figure 4.6: One-dimensional spectra of the MS pressure for combinations of regions. ▬ All regions (R1234); △ viscous shear-layer, buffer layer and logarithmic region(R123); + viscous shear-layer and buffer layer(R12) ∘ buffer layer and logarithmic region(R23). (a) Streamwise, (b) spanwise.

Spectra	Wavenumber range			
	Lowest	Low	Intermediate	High
	$k_x\delta < 1$	$1 < k_x\delta, k_z\delta < 5$	$5 < k_x\delta, k_z\delta < 30$	$30 < k_z\delta < 70$
π^{MS}	2+3	2+3	1+2	1+2
π^{TT}	1+2+3+4	1+2+3	1+2	1+2

Table II: Regions of channel which dominate the MS and TT spectra. 1: viscous shear-layer; 2: buffer layer; 3: logarithmic region; 4: upper channel.

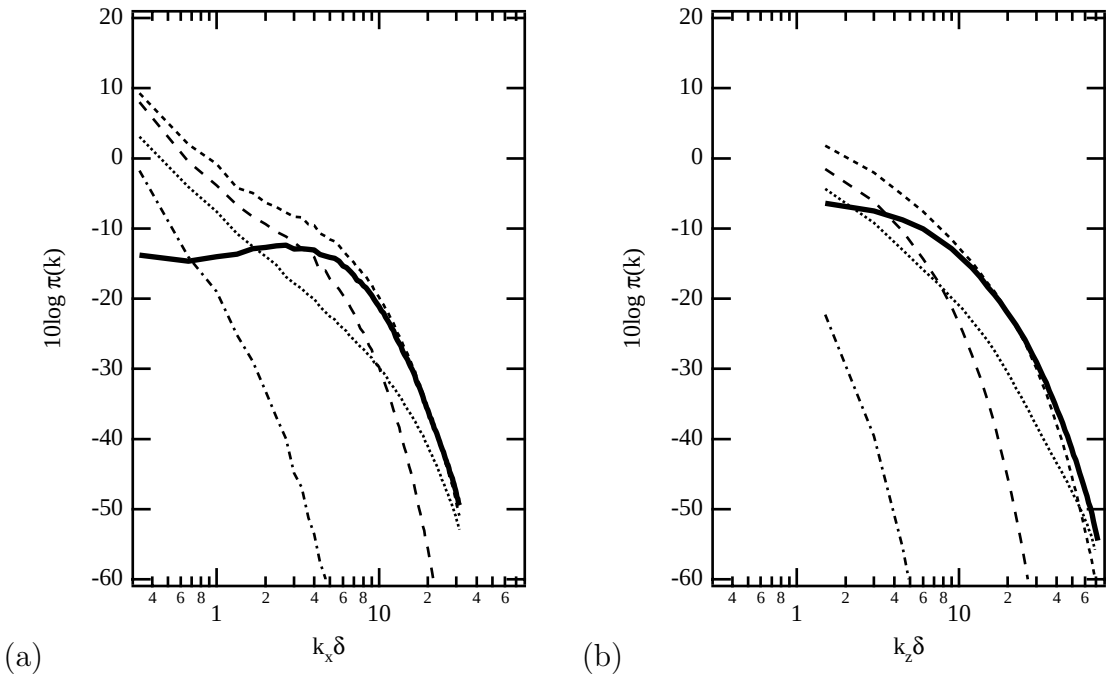

Figure 4.7: One-dimensional spectra of the TT pressure for the various regions. ——— All regions (R1234); ····· viscous shear-layer(R1); - - - - - - - - buffer layer (R2); – – – – logarithmic region (R3); —·— upper channel (R4). (a) Streamwise, (b) spanwise.

Figure 4.7 shows the spectra of the partial contributions to the TT pressure for each of the four regions. In this case the individual curves have a significantly different behavior than their sum. The buffer layer gives the largest contribution, except at the highest spanwise wavenumbers, where the viscous shear-layer becomes important. Since, at low wavenumbers, the sum of the contributions to the total pressure from the various regions results in spectral values much lower than those of each region, the contributions of the individual regions must cancel each other out, indicating that long-wavelength turbulent structures may have coherence over the entire channel. The high levels of the total pressure spectra at low wavenumbers shown previously in Figure 4.3 are due to the TT contribution, since the MS pressure spectra were previously shown to be flat at low wavenumbers.

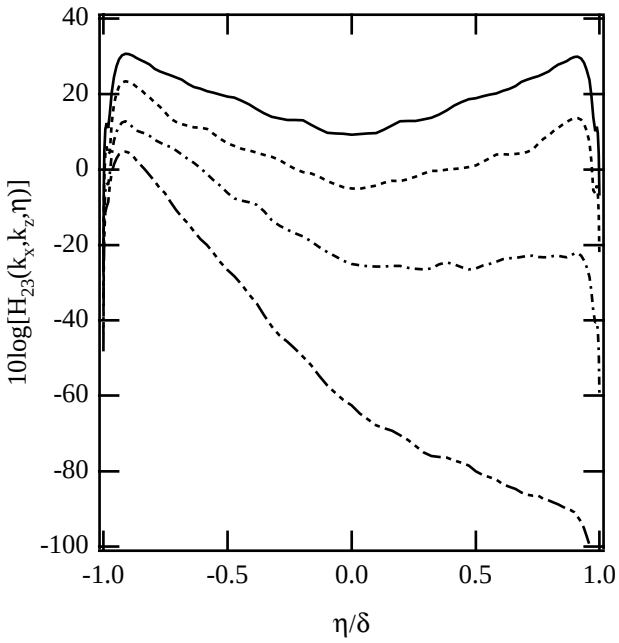

Figure 4.8: Wall-normal distribution of $H_{23}^{TT}(\mathbf{K},\eta)$. —— $k_x\delta = 1/3,\ k_z\delta = 0$; ····· $k_x\delta = 1/3,\ k_z\delta = 3/2$; –·– $k_x\delta = 1,\ k_z\delta = 9/2$; –··– $k_x\delta = 3,\ k_z\delta = 12$.

The high levels of the total- and TT-pressure spectra from the upper channel that are seen in Figures 4.3(a) and 4.7(a) can be explained by examining the integrand of (4.1.1), $H_{ij}^{TT}(\mathbf{K},\eta) = \widehat{h}_{ij}^{*}\widehat{h}_{ij}$, where $\widehat{h}_{ij}$ is the product of the T_{ij}^{TT} source term and the Green's function,

$$\widehat{h}_{ij}(\mathbf{K},\eta) = \widehat{T}_{ij}^{TT}(\mathbf{K},\eta)G(K, y=-1, \eta). \tag{4.3.13}$$

Figure 4.8 shows $H_{23}^{TT}(\mathbf{K},\eta)$ for various values of $\mathbf{K}$. The lowest $\mathbf{K}$ combination, which represents a planar wave with wavelength equal to the streamwise box size, presents very little attenuation across the channel, indicating that the pressure at the lowest wavenumbers at one wall is affected by sources from the buffer layer on the opposite one, *i.e.*, that the Green's function is a low-pass filter that is almost transparent to the low-wavenumber sources. This does not explain, however, why the TT partial pressures from all the regions cancel each other out.

Figure 4.9 shows the TT partial pressure spectra obtained by combinations

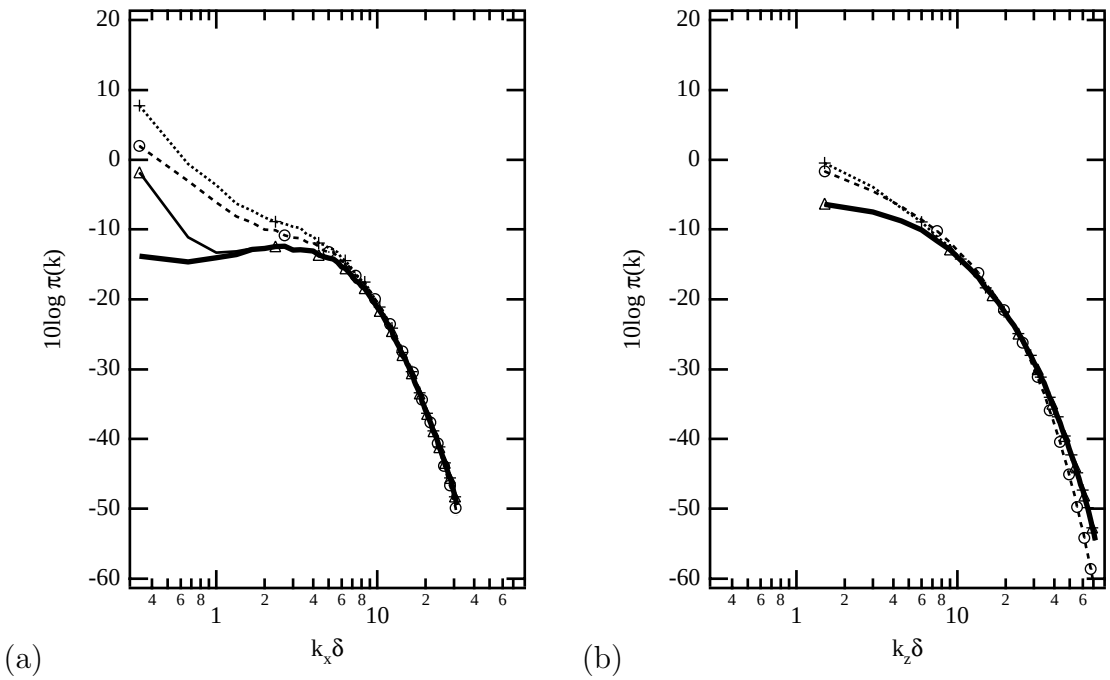

Figure 4.9: One-dimensional spectra of the TT pressure due to combinations of regions. ━━ All regions (R1234); △ viscous shear-layer, buffer layer and logarithmic region (R123); + viscous shear-layer and buffer layer (R12) ∘ buffer layer and logarithmic region (R23). (a) Streamwise, (b) spanwise.

of the various regions. The sum of the partial pressures due to viscous shear-layer and buffer layer, $\pi^{TT}(R12)$, matches $\pi^{TT}(R1234)$ for intermediate and high wavenumbers ($k_x\delta, k_z\delta > 5$). In the low-wavenumber range, however, the sources from the logarithmic region become important, as shown by the agreement between $\pi^{TT}(R123)$ and $\pi^{TT}(R1234)$. The present results indicate that the viscous shear-layer gives a very significant contribution to the turbulent-pressure spectra: the partial-pressure spectrum due to the buffer and logarithmic layers alone, $\pi^{TT}(R23)$, diverges from $\pi^{TT}(R1234)$ and $\pi^{TT}(R123)$ even at low wavenumbers. All regions give significant contributions to the lowest wavenumbers, again due to the small amount of attenuation provided by the Green's function. The partial-pressure spectra due to each region are higher than those due to their combination, as also observed before. Table II summarizes the regions that were found to affect most

the spectra of the MS and TT pressure. The wavenumber ranges defined in the Table will be used throughout the rest of this dissertation.

4.4 Contribution of individual TT partial pressures

In this section we will investigate which of the TT components affects most the TT partial pressure spectra, by first examining the terms singly, then by combining them in various ways and comparing them to the total- or TT-pressure spectra.

Figure 4.10 shows the spectra of the most significant TT terms and regions. Similar to what was observed before, the spectra of the individual TT terms have higher low-wavenumber content (in the streamwise direction) than their combination. In the lowest- and low-wavenumber ranges $\pi_{23}^{TT}(R2)$, $\pi_{23}^{TT}(R3)$ and $\pi_{13}^{TT}(R2)$ are the dominant terms; all the TT terms, particularly those due to the logarithmic and buffer regions, have similar behavior and are higher than $\pi^{TT}(R4)$ at the lowest wavenumbers. In the range $10 < k_z\delta < 20$, $\pi_{23}^{TT}(R2)$ and $\pi_{13}^{TT}(R2)$ are the most significant while for $20 < k_x\delta < 30$, three terms, $\pi_{23}^{TT}(R2)$, $\pi_{13}^{TT}(R2)$, and $\pi_{12}^{TT}(R2)$ dominate. $\pi_{23}^{TT}(R2)$ is the largest term for the spanwise spectra as well, except at the highest wavenumbers ($k_z\delta > 60$), where contributions from the viscous shear-layer become important. Figure 4.11 shows that $\pi_{22}^{TT}(R1)$, $\pi_{33}^{TT}(R1)$ and $\pi_{23}^{TT}(R1)$ are the dominant terms in the highest k_z wavenumber range. It is interesting to observe that the diagonal terms $\pi_{22}^{TT}(R1)$ and $\pi_{33}^{TT}(R1)$ decay like k_z^{-5}, whereas the off-diagonal terms, $\pi_{13}^{TT}(R1)$ and $\pi_{23}^{TT}(R1)$, decay at a steeper rate, roughly k_z^{-7}.

Once the dominant terms and regions were identified, they were combined to

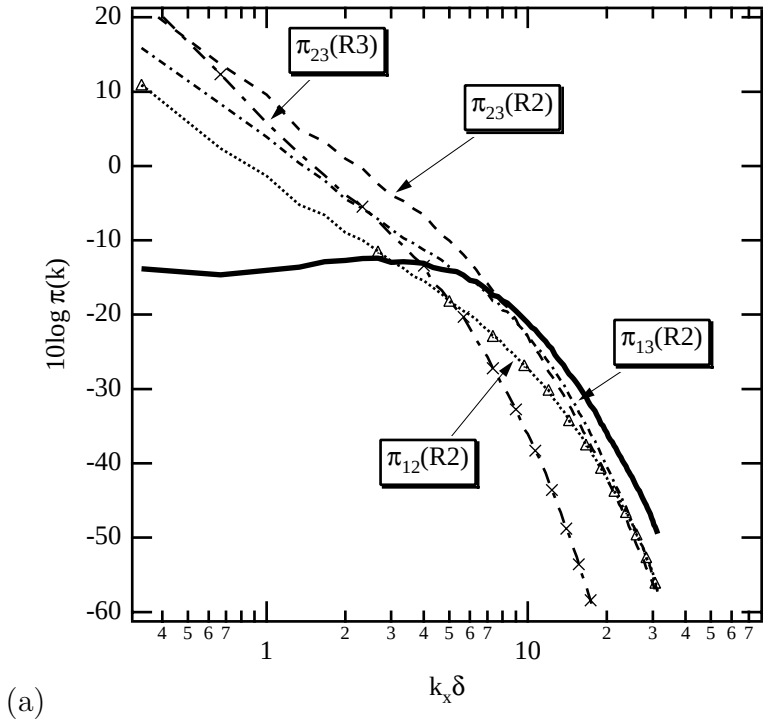

(a)

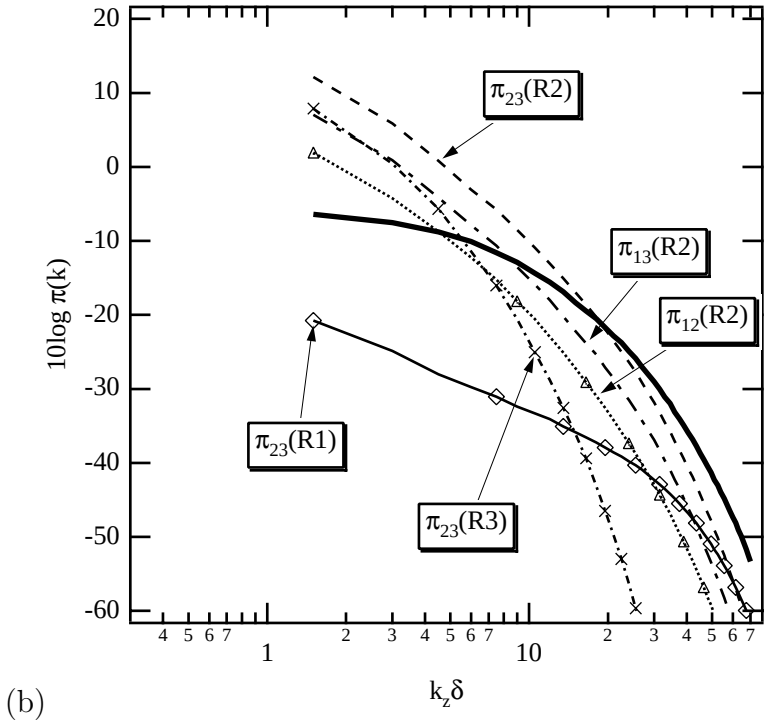

(b)

Figure 4.10: One-dimensional partial pressure spectra due to dominant TT source terms and regions. ▬▬ $\pi^{TT}(R1234)$; ◇ $\pi_{23}^{TT}(R1)$; – – – – $\pi_{23}^{TT}(R2)$; × $\pi_{23}^{TT}(R3)$; △ $\pi_{12}^{TT}(R2)$; –·– $\pi_{13}^{TT}(R2)$. (a) Streamwise, (b) spanwise.

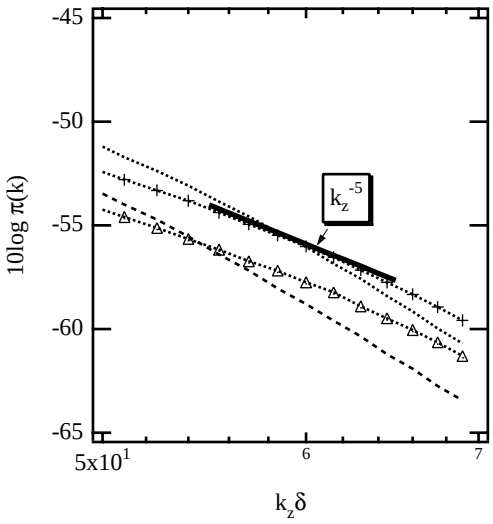

Figure 4.11: Partial pressures for sources in the viscous shear-layer. - - - - - - - - - : $\pi_{13}^{TT}(R1)$; $\triangle$: $\pi_{22}^{TT}(R1)$; ..... : $\pi_{23}^{TT}(R1)$; + : $\pi_{33}^{TT}(R1)$.

determine whether subsets of terms or regions could re-constitute the total pressure. The combinations are summarized in Table III. Combination 4, C4, which combines $\pi^{MS}(R2)$, $\pi_{23}^{TT}(R2)$ and $\pi_{13}^{TT}(R2)$ is shown in Figure 4.12. The addition of $\pi^{MS}(R1)$ (C17), which is the dominant term at higher wavenumbers (see Figure 4.5) gives significant improvement. Additional terms, such as $\pi^{MS}(R3)$ (C18) and $\pi_{23}^{TT}(R3)$ and $\pi_{13}^{TT}(R3)$ (C19) did not give further improvements. The spanwise spectra extend to much higher wavenumbers than the streamwise ones; to obtain agreement for the highest wavenumbers it was necessary to add the contribution of $\pi_{33}^{TT}(R123)$. (In Figure 4.11, $\pi_{33}^{TT}(R1)$ was shown to be the dominant partial pressure above $k_z\delta = 60$; in the high wavenumber range $\pi_{33}^{TT}(R23)$ is much smaller than $\pi_{33}^{TT}(R1)$ and the fact that $\pi_{33}^{TT}(R123)$ was added instead of $\pi_{33}^{TT}(R1)$ should not make an appreciable difference to our conclusions).

While the dominant contributions to the high-wavenumber regions of the pressure spectra could be identified and isolated, no such simplification could be made for the low-wavenumber range. Numerous combinations were tried; Figure 4.13

Combination	Terms
C1	$\widehat{p}_{23}^{TT}(R2) + \widehat{p}_{13}^{TT}(R2)$
C2	$\widehat{p}_{23}^{TT}(R3) + \widehat{p}_{13}^{TT}(R3)$
C3	$\widehat{p}_{23}^{TT}(R23) + \widehat{p}_{13}^{TT}(R23)$
C4	$\widehat{p}^{MS}(R2) + \widehat{p}_{23}^{TT}(R2) + \widehat{p}_{13}^{TT}(R2)$
C17	$\widehat{p}^{MS}(R12) + \widehat{p}_{23}^{TT}(R2) + \widehat{p}_{13}^{TT}(R2)$
C18	$\widehat{p}^{MS}(R123) + \widehat{p}_{23}^{TT}(R2) + \widehat{p}_{13}^{TT}(R2)$
C19	$\widehat{p}^{MS}(R123) + \widehat{p}_{23}^{TT}(R23) + \widehat{p}_{13}^{TT}(R23)$
C26	$\widehat{p}^{MS}(R123) + \widehat{p}_{23}^{TT}(R123) + \widehat{p}_{13}^{TT}(R123)$
C27	$C17 + \widehat{p}_{33}^{TT}(R123)$
C20	$\widehat{p}^{TT}(R123) - \widehat{p}_{11}^{TT}(R123)$
C21	$\widehat{p}^{TT}(R123) - \widehat{p}_{22}^{TT}(R123)$
C22	$\widehat{p}^{TT}(R123) - \widehat{p}_{33}^{TT}(R123)$
C23	$\widehat{p}^{TT}(R123) - \widehat{p}_{12}^{TT}(R123)$
C24	$\widehat{p}^{TT}(R123) - \widehat{p}_{13}^{TT}(R123)$
C25	$\widehat{p}^{TT}(R123) - \widehat{p}_{23}^{TT}(R123)$

Table III: Combinations of terms used in attempts to reconstitute the total wall pressure spectra.

shows that even removal of the $\pi_{11}^{TT}(R123)$ contribution, which was shown to be the least significant, changes the spectra from a flat one, $[\pi^{TT}(R1234)]$ to one that has high energy in the low wavenumbers.

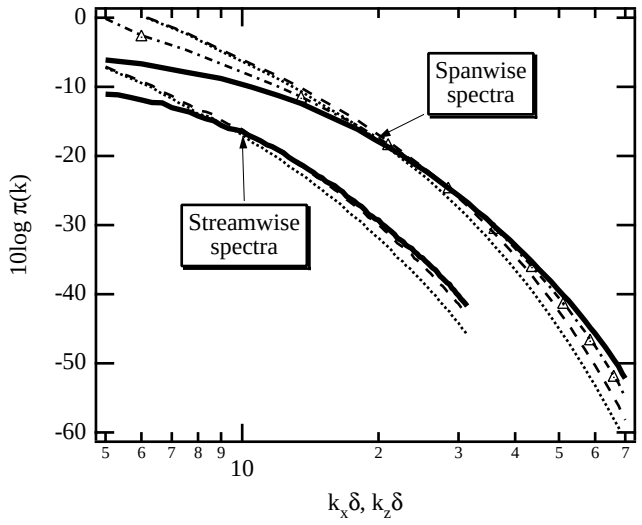

Figure 4.12: One-dimensional spectra of the total pressure compared with various combinations of source terms and regions. ——— All regions and source terms; ..... C4 – – – – C17; △ C27.

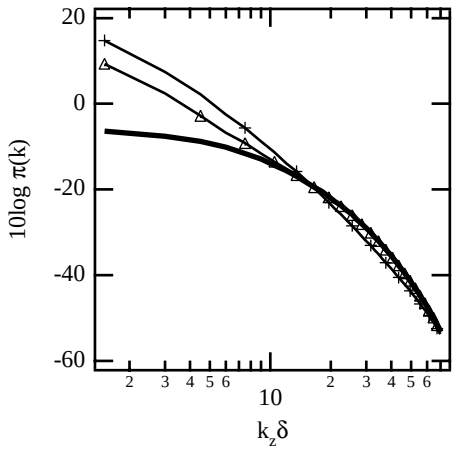

Figure 4.13: One-dimensional spanwise spectra of the TT pressure for regions 1 through 3 with various source terms removed. ——— All source terms; △ $\pi_{11}^{TT}(R123)$ removed; ◇ $\pi_{23}^{TT}(R123)$ removed.

4.5 Summary

The MS and TT terms are of the same order of magnitude throughout the wavenumber range; both have the same shape as the total pressure. The medium and high wavenumber ($k_x\delta, k_z\delta \geq 5$) MS partial pressure is generated in the viscous shear-layer and buffer layer, whereas the lower wavenumber ($k_x\delta, k_z\delta \leq 5$) MS partial pressure is generated in the buffer region and logarithmic region. The contribution of the viscous shear-layer to the low wavenumber MS partial pressure is insignificant while the upper channel contribution to the low wavenumber MS partial pressure is small.

The medium and high wavenumber TT partial pressures are generated in the viscous shear-layer and in the buffer layer. In the low wavenumbers the TT partial pressure is due to the buffer region and logarithmic region with a significant contribution from the viscous shear-layer. In the lowest wavenumbers ($k_x\delta \leq 1$), all regions of the channel are important. The dominant TT partial pressures in the medium wavenumber range are due to π_{23}^{TT} and π_{13}^{TT} from the buffer region. In the highest streamwise wavenumbers π_{12}^{TT} is about the same magnitude as π_{23}^{TT} and π_{13}^{TT}.

The very highest spanwise wavenumber ($k_z\delta > 60$) partial pressures are dominated by π_{23}^{TT}, π_{22}^{TT} and π_{33}^{TT} from the viscous shear-layer.

The individual TT terms and the TT partial pressures for various regions are very high in the low wavenumbers. This is in contrast to the total TT spectra which is flat in the low wavenumbers. It appears that the the low wavenumber sources are coherent across the channel.

Chapter 5

Characteristics of Source Terms

In the previous Chapter the characteristics of the partial pressures, due to the individual terms from four regions of the channel, were examined. From that investigation, the dominant terms and regions which contribute to the wall pressure were discovered. In this chapter, the source terms themselves are studied, particularly those related to the dominant partial pressures. The examination will take place primarily in one-dimensional spectral space at certain characteristic wall-normal locations, which will give indications as to the most important length scales of the source terms. These length scales will then be related to current notions of boundary-layer turbulence structures.

The source terms, $T_{ij}(x, y, z)$, were computed in three-dimensional physical space using the 2/3 rule to eliminate aliasing errors. Nine terms were computed: the six TT terms, their sum, the MS term and the total. They were then Fourier-transformed to yield their complex coefficients in planar wavenumber space, $\widehat{T_{ij}}(\mathbf{K}, y)$. The two-dimensional spectrum of the source terms is given by

$$\Phi_{ij}(\mathbf{K}, y) = \widehat{T}^*_{ij}(\mathbf{K}, y)\widehat{T}_{ij}(\mathbf{K}, y) \qquad \text{(no summation)} \tag{5.0.1}$$

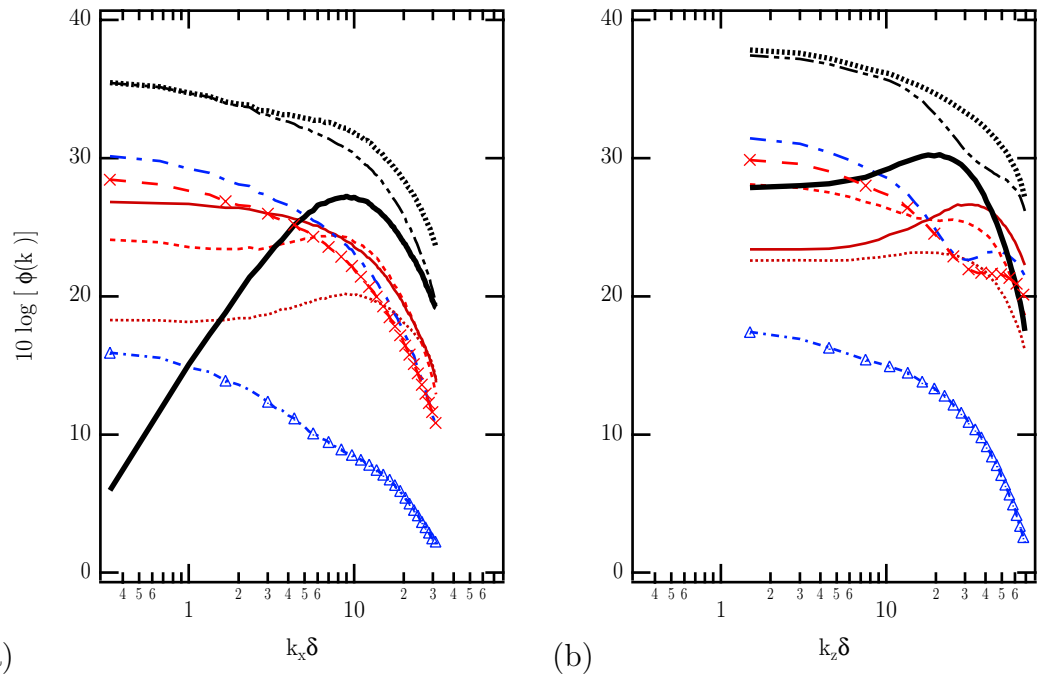

Figure 5.1: Source term spectra at $y^+ = 5$ (a) streamwise (b) spanwise; $\triangle$: T_{11}^{TT}; ..... : $2T_{12}^{TT}$; ---------- : $2T_{13}^{TT}$; $\times$: T_{22}^{TT}; —— : $2T_{23}^{TT}$; – – – : T_{33}^{TT}; ▬▬ : T^{MS}; —·— : T^{TT}; ▪▪▪▪▪▪▪▪▪▪ : T^{Tot}.

The one-dimensional spectra $\phi_{ij}(k_x, y)$ and $\phi_{ij}(k_z, y)$ were obtained by integrations, similar to (4.1.7) and (4.1.8) and normalized by u_τ^4/δ^4. The one-dimensional spectra of all the source terms, at representative wall-normal locations, are shown in Figures 5.1 through 5.5. The locations are in the viscous shear-layer ($y^+ = 5$); in the buffer layer ($y^+ = 12$ and 21), which correspond to the peaks of the m.s. distributions of the MS and total source terms, respectively; and two locations in the logarithmic region, one in the inner part, $y^+ = 49$, and one near the channel centerline, $y^+ = 145$. We will now discuss the physics of the MS term, followed by a discussion of the TT terms.

5.1 MS sources

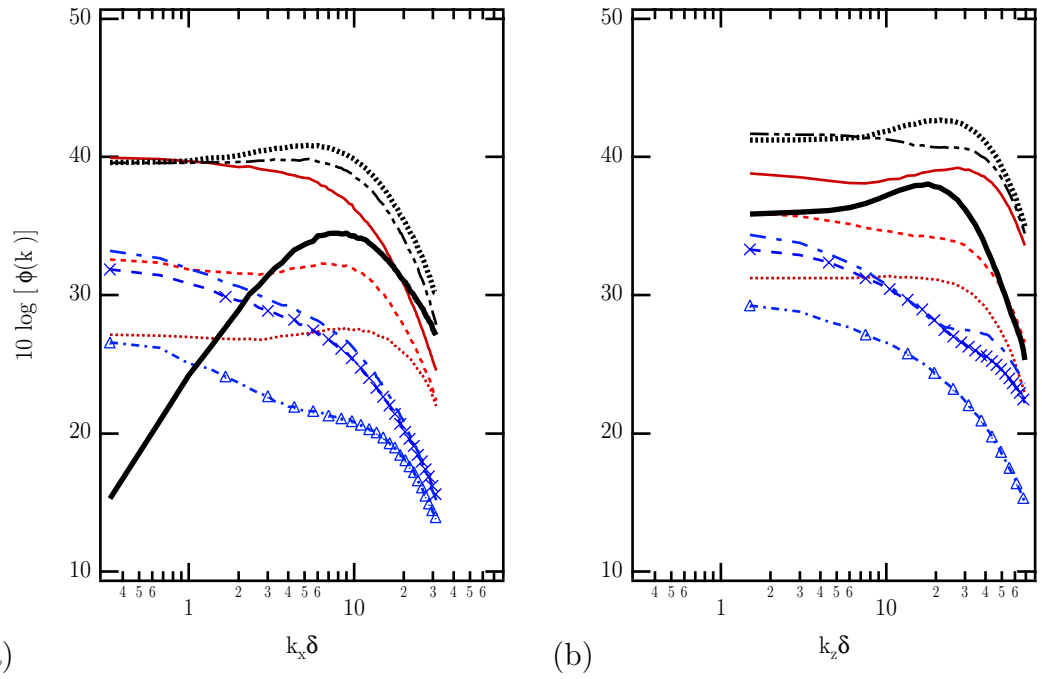

Figure 5.2: Source term spectra at $y^+ = 12$ (a) streamwise (b) spanwise. Same legend as Figure 5.1.

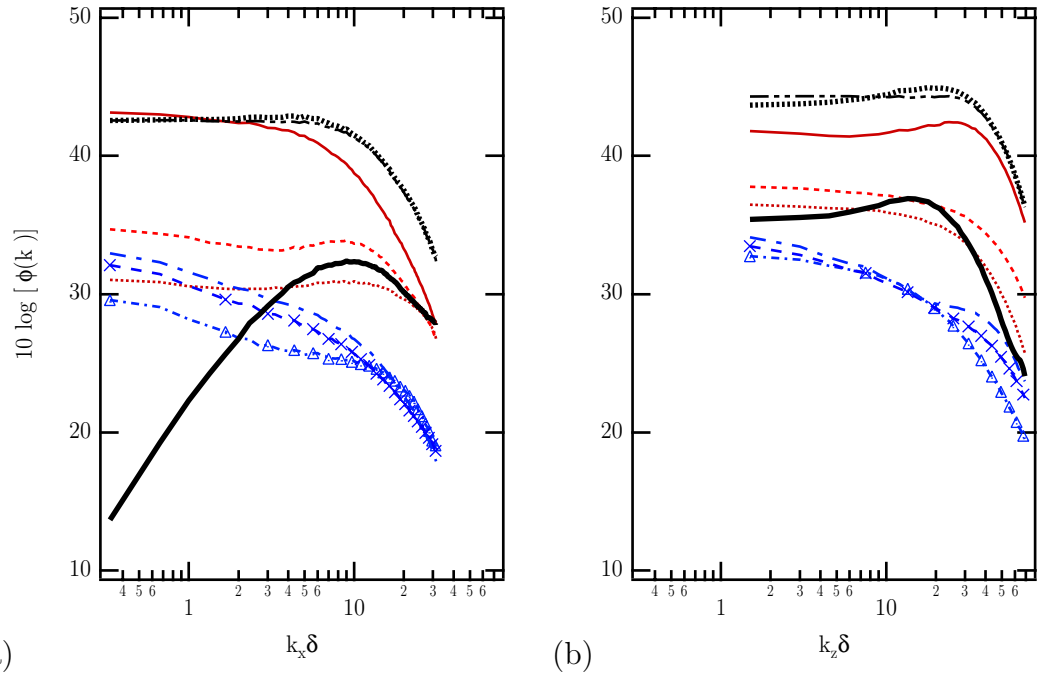

Figure 5.3: Source term spectra at $y^+ = 21$ (a) streamwise (b) spanwise. $\triangle$: T_{11}^{TT}; ····· : $2T_{12}^{TT}$; - - - - - : $2T_{13}^{TT}$; $\times$: T_{22}^{TT}; —— : $2T_{23}^{TT}$; – – – : T_{33}^{TT}; ▬▬ : T^{MS}; —·— : T^{TT}; ▪▪▪▪▪ : T^{Tot}.

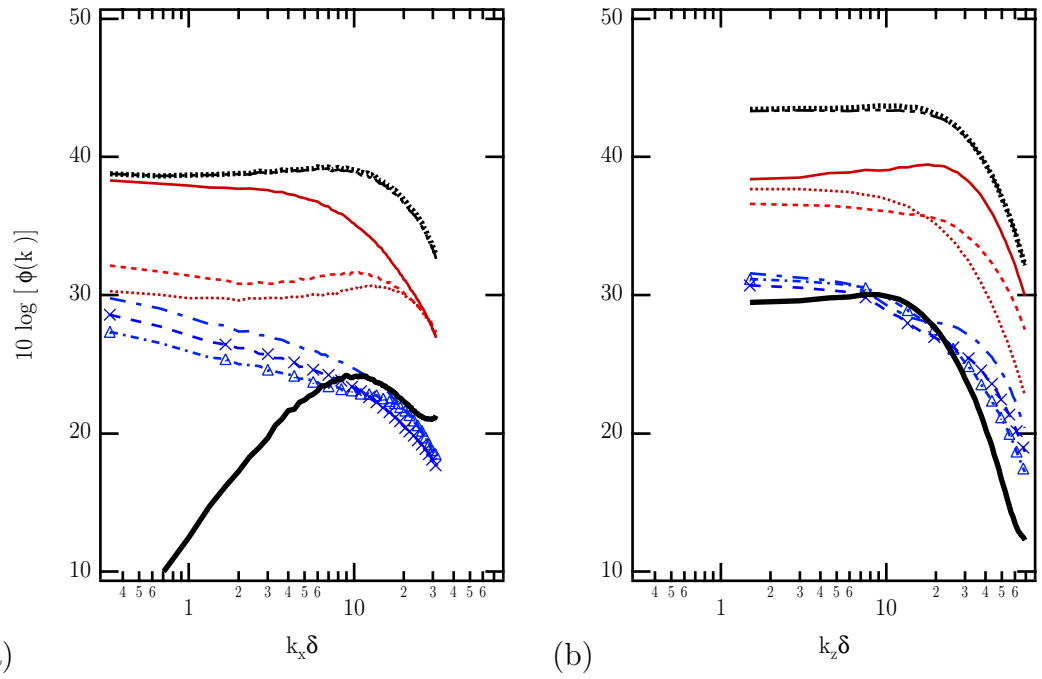

Figure 5.4: Source term spectra at $y^+ = 49$ (a) streamwise (b) spanwise. Same legend as Figure 5.3.

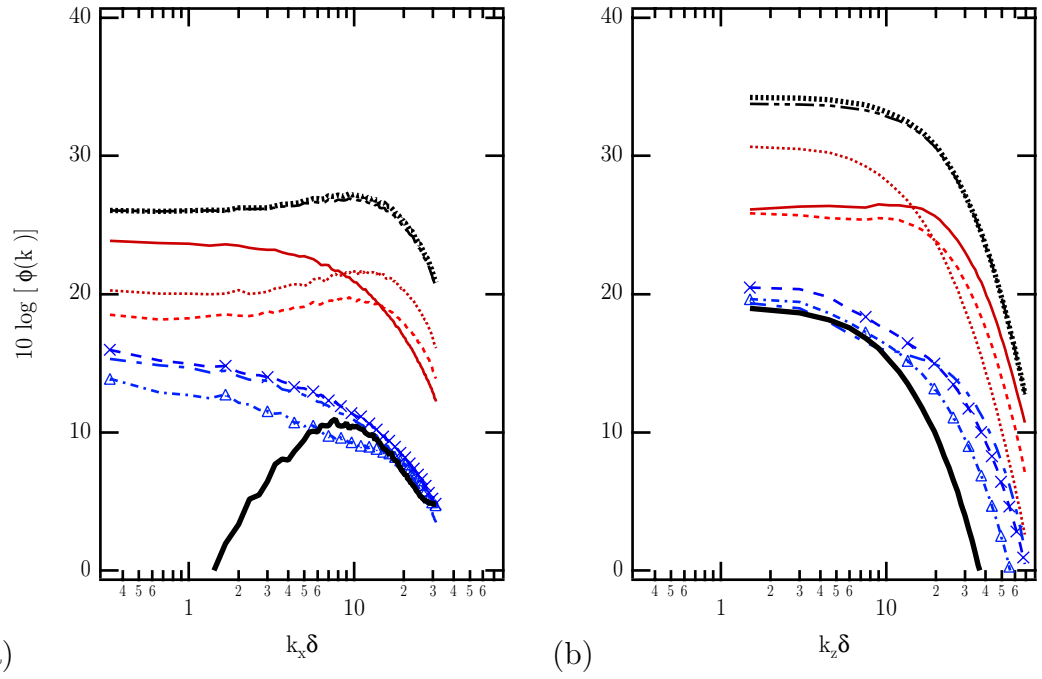

Figure 5.5: Source term spectra at $y^+ = 145$ (a) streamwise (b) spanwise. $\triangle : T_{11}^{TT}$; ····· : $2T_{12}^{TT}$; - - - - - : $2T_{13}^{TT}$; $\times : T_{22}^{TT}$; —— : $2T_{23}^{TT}$; – – – : T_{33}^{TT}; ▬▬ : T^{MS}; —·— : T^{TT}; ▪▪▪▪▪ : T^{Tot}.

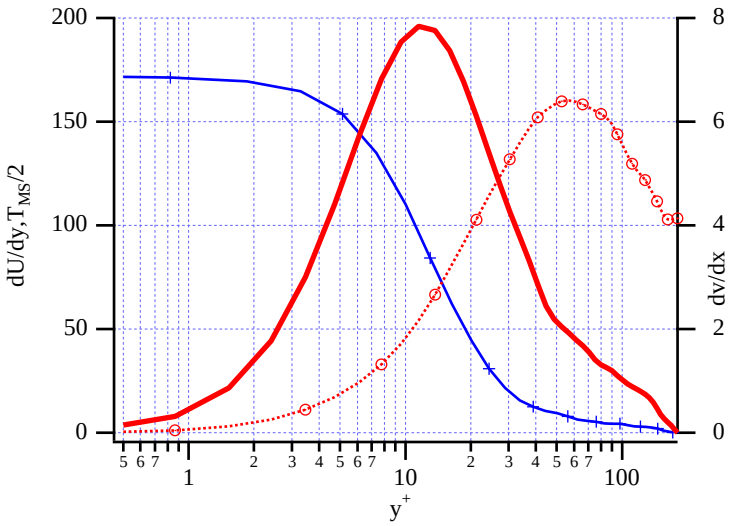

Figure 5.6: Wall-normal distribution of the components of the MS source term. + dU/dy; root-mean-square values: ∘ $\partial v/\partial x$; ━━ $(dU/dy)(\partial v/\partial x)$. All values have been normalized by u_τ and δ.

In the previous Chapter, the MS term was shown to be greater than the TT term over the entire streamwise and most of the spanwise wavenumber ranges. It was also shown that the largest contribution to the MS partial pressure came from the buffer layer. The MS term, shown in Figure 5.6, is twice the product of dU/dy and $\partial v/\partial x$. While dU/dy is maximum at the wall, $\partial v/\partial x$ is zero at the wall, and peaks at $y^+ \approx 60$. Since their product peaks at $y^+ = 12$, the most important region for MS partial pressure generation is expected to be the buffer layer.

Figures 5.1 through 5.5 show that the MS and TT terms have fundamentally different behavior as $k_x \to 0$: the TT terms approach a constant while the MS term is proportional to k_x^2. The mathematical reason for this can be seen through the spectral representation of the MS term:

$$\phi_{MS}(k_x, y) = 4\left(\frac{dU}{dy}\right)^2 \left|\widehat{\frac{\partial v}{\partial x}}^* \widehat{\frac{\partial v}{\partial x}}\right| = 4k_x^2 \left(\frac{dU}{dy}\right)^2 |\widehat{v}^* \widehat{v}| \tag{5.1.2}$$

which tends to 0 as $k_x \to 0$ because both dU/dy and $|\widehat{v}^* \widehat{v}|$ are well-behaved functions as $k_x \to 0$.

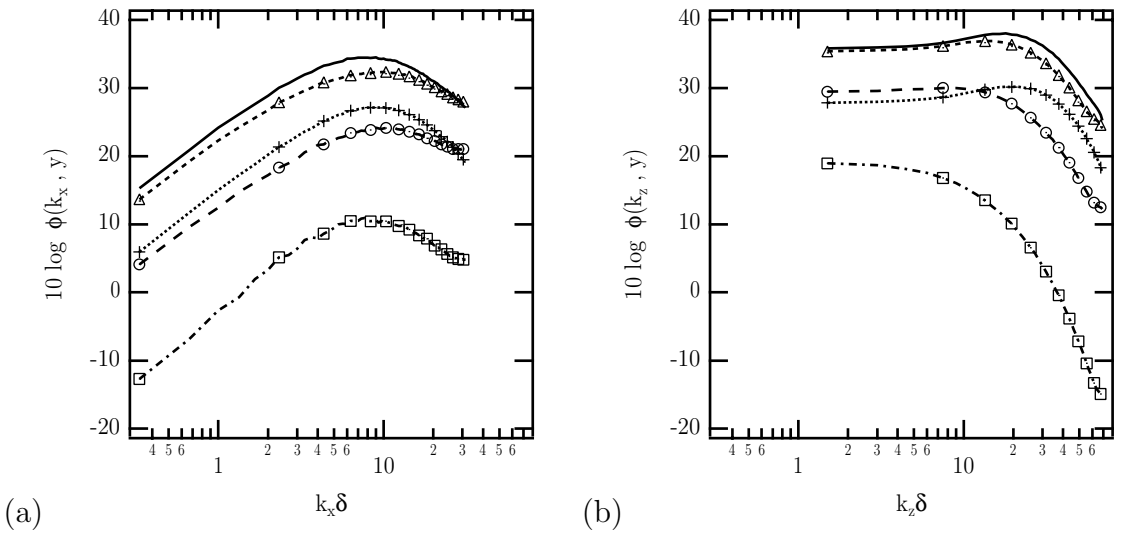

Figure 5.7: One-dimensional spectra of the MS source term. + $y^+ = 5$; —— $y^+ = 12$; △ $y^+ = 21$; ○ $y^+ = 49$; □ $y^+ = 145$. (a) Streamwise; (b) spanwise.

Comparing the spectra from the various wall-normal locations in Figure 5.7 shows that, consistent with Figure 5.6, the highest levels of the MS source spectra are found at $y^+ = 12$ and $y^+ = 21$. This is consistent with the finding that the MS partial pressure from the buffer layer is dominant. The spectra at $y^+ = 5$ and $y^+ = 12$ have a broad peak centered at approximately $k_x\delta = 8$, $k_z\delta = 13.5$, indicative of structures that are about 140 and 60 wall units in the streamwise and spanwise directions, respectively.

Several observations suggest that near-wall shear layers may be the principal source of the MS pressure; among them are the fact that near-wall shear layers and spanwise vortices have large gradients in the $x-y$ plane, which means that $\partial v/\partial x$ should be large there. It has been shown that the near-wall region is well-populated with near-wall shear layers but not by spanwise vortices [Robinson *et al.* (1989)]. Also, experimental and computational studies have shown that they generate high amplitude WPFs [Thomas and Bull (1983), Johansson *et al* (1987a,b), Johansson, Alfredsson, and Kim (1988), Wilczynski (1992)]. Finally, quasi-streamwise

vortices, the dominant vortex structure in the near-wall region, do not directly generate MS partial pressure.

Near-wall shear layers are turbulent structures formed at the interface between a downstream region of slower-moving fluid and an upstream region of faster-moving fluid. They are thought to form when faster-moving outer fluid impinges on slower moving fluid that is being ejected by either the legs of a quasi-streamwise vortex or the spanwise head of the horseshoe vortex. Johansson *et al* (1987a) showed that they exist primarily in the near wall region ($y^+ < 100$); that in the viscous shear-layer, near-wall shear layers form a small ($\approx 7^o$) angle to the wall, whereas further from the wall assume a shallow ($\approx 20^o$) angle [Figure 5.8(a)]. Figure 5.8 shows that the near-wall shear layer has an "ejection" region $(Q_2)^*$ downstream of the shear layer and a "sweep" region (Q_4) upstream. Figure 5.8(b) shows that there are three regions of $\partial v/\partial x$: a region in the center of the shear layer, where there is a sharp transition from a region of positive v, downstream and negative v, upstream; regions upstream and downstream of the shear layer ($y^+ \approx \pm 125$). A positive pressure event, shown in the $x - z$ plane, Figure 5.9, is located beneath the center of the shear layer. There is very close correlation between the positive $\partial v/\partial x$ and positive pressure, as shown in Figure 5.10. The relationship between T^{MS} and partial pressure at the wall is

$$\hat{p}^{MS}(y = -1, \eta, K) \sim \frac{dU}{dx}\frac{\partial v}{\partial x}\frac{1}{K}\exp[-K(1+\eta)] \tag{5.1.3}$$

where all factors except $\partial v/\partial x$ have to be positive, meaning that the sign of the MS partial pressure is the same as $\partial v/\partial x$. Figure 5.10 shows that there is a close correspondence between regions of positive $\partial v/\partial x$ and positive pressure. Similar

*The Q_i denote quadrants of the $u - v$ plane: Q_2 denotes negative u, positive v; Q_4 denotes positive u, negative v. See Wallace, Eckelmann and Brodkey (1972).

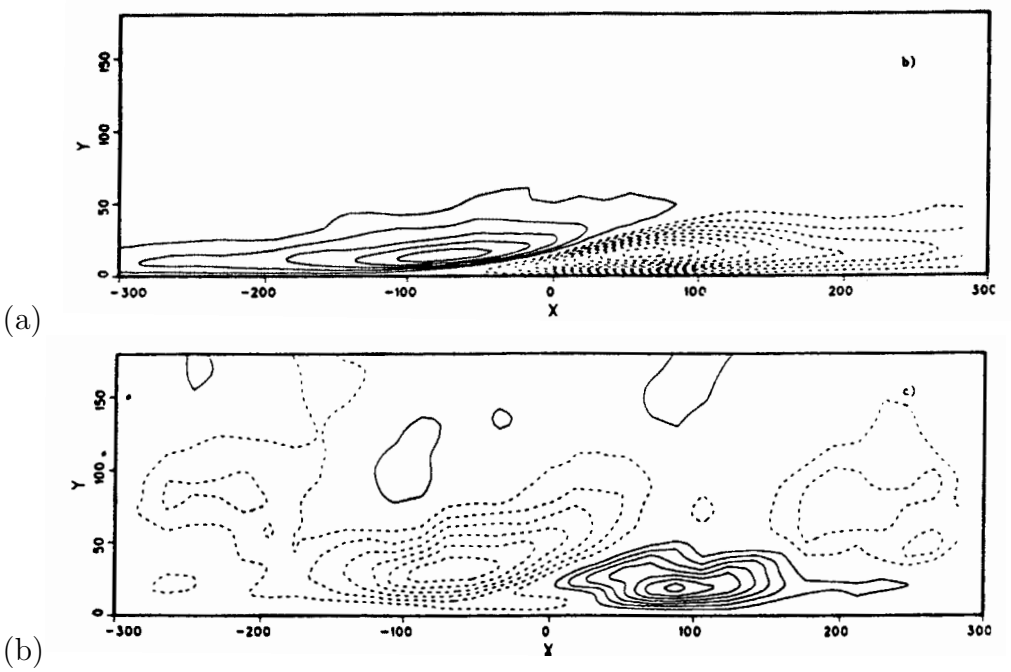

Figure 5.8: Shear layer structure as represented by velocity contours in the $x - y$ plane. Horizontal and vertical coordinates are in wall units. Velocities normalized by their local RMS values; —— : positive; - - - - - - - - - : negative. (a) u, contour increment 0.5 (b) v, contour increment 0.1. From Johansson, Alfredsson, and Kim (1988); published with permission.

results, in the time domain, have been shown by Wilczynski (1992).

The question remains, do the dominant length scales indicated by the T^{MS} source spectra compare with those for near-wall shear layers? As seen in Figure 5.10, the streamwise length scale of the central ($-60 \leq x^+ \leq 80$) v-pattern is approximately 140 wall units. The MS source spectra also has a peak corresponding to a wavelength of about 140 wall units. Also, the MS partial pressure from the buffer layer, shown in Figure 4.5(a), has a peak at $k_x\delta = 3.333$ which corresponds to a streamwise length scale of about 380 viscous units, close to the streamwise length of the entire shear-layer structure and pressure pattern shown in Figure 5.10.

It has been shown by Wilczynski (1992) that the upstream ($x^+ < -60$) and

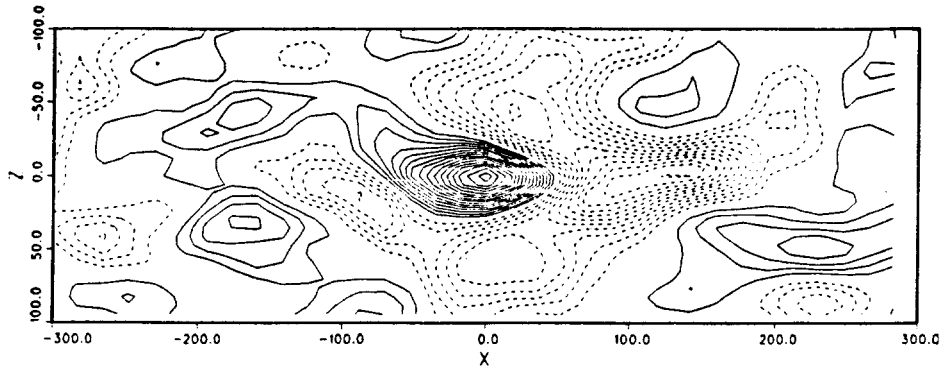

Figure 5.9: Wall-pressure due to shear layer in the $x-z$ plane. Pressure normalized by τ_w; contours every 0.1; —— : positive; - - - - - - - - : negative. From Johansson, Alfredsson, and Kim (1988); published with permission.

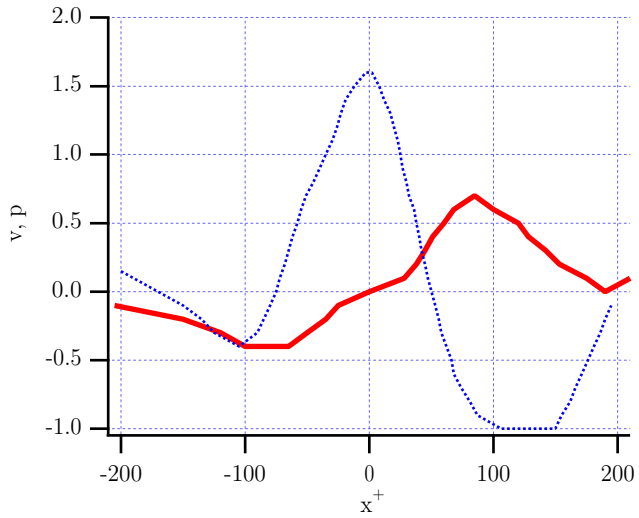

Figure 5.10: Relationship between vertical velocity and wall pressure in centerplane of near-wall shear layer ($y^+ = 15$). Horizontal coordinate are in viscous units with $x^+ = 0$ detection location. ——— : v normalized by local r.m.s. values; ..... : wall pressure normalized by τ_w. Data extracted from Johansson, Alfredsson, and Kim (1988).

downstream ($x^+ > 80$) regions may have much smaller $\partial v/\partial x$ than in the center of the shear layer. Furthermore, the regions, upstream and downstream of the center may contribute both to the higher wavenumber sources, appropriate to their local length scales (*i.e.*, approximately 100 wall units), as well as to lower wavenumber sources, which reflect the entire 400 wall unit length. When the source is multiplied by the Green's function to obtain the wall pressure, the low wavenumber contributions, due to the entire structure are magnified and show up as a lower wavenumber peak in the partial pressure spectra, whereas the higher wavenumbers are attenuated. This may explain why the source spectra has a peak that reflects only the central part of the $\partial v/\partial x$ signature, while the partial pressure spectra reflects the entire length of the signature.

The spanwise length scale for the near-wall shear layers is about $70 - 80$ wall units [Johansson, Alfredsson, and Kim (1988)]. This corresponds well with the peak of the MS source spectra (≈ 60 wall units).

Overall, the length scales of the streamwise and spanwise wavenumber spectra correspond very well with the length scales from the conditionally averaged near-wall shear layers, providing more evidence that the MS pressure is caused by near-wall shear layers.

5.2 TT sources

In this section we attempt to make connections between the dominant TT source terms and coherent turbulent structures.

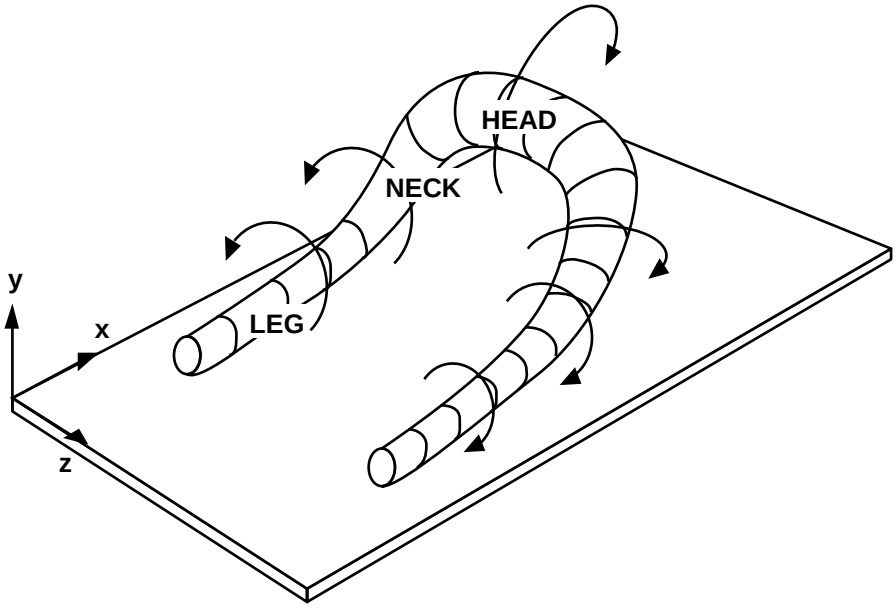

Figure 5.11: Conceptual drawing of a horseshoe vortex.

Quasi-streamwise vortices

We make the conjecture that the dominant TT terms are generated by vortical structures such as horseshoe vortices. As shown in Figure 5.11, such a model involves a spanwise vortex "head" with a tilted "neck" and trailing "legs" that descend into the buffer region. The vortices that make up the legs, which have a streamwise orientation, and the necks, which have a wall-normal component as well, are called "quasi-streamwise". It has been shown by Robinson (1991b) that the centers of quasi-streamwise vortices occur predominantly in the region $20 < y^+ < 70$, $y^+ \approx 30$ being their average location; their diameters are in the range $15 < d^+ < 50$, and their streamwise scale is "an order of magnitude shorter than the longest sublayer streaks" (which are approximately 1000 wall units) [Robinson (1991b)].

It was found that π_{23}^{TT} from the buffer layer is the largest term over almost the entire k_x and k_z ranges. The corresponding source, T_{23}^{TT}, can be related to

quasi-streamwise vortices, which have regions where the product of $\partial w/\partial y$ and $\partial v/\partial z$ is large: for a circular vortex, this will occur in four regions centered around the quadrant bisectors, as shown in Figure 5.12a. For instance, if a vortex is centered at $y^+ \approx 30$ and has a diameter $d^+ \approx 25$, the regions of maximum T_{23}^{TT} will occur at $y^+ \approx 21$ and $y^+ \approx 38$. The first location is, in fact, fairly close to the peak of the T_{23}^{TT} mean-square distribution shown in Figure 5.13. The spectra of T_{23}^{TT} at $y^+ = 21$, shown in Figure 5.3, shows that $T_{23}^{TT}(k_x)$ is dominated by low wavenumbers while $T_{23}^{TT}(k_z)$ has a peak at about $k_z\delta = 25$ corresponding to long streamwise structures with a spanwise scale of 45 wall units. This is a reasonable length scale for T_{23}^{TT} generated by quasi-streamwise vortices.

It was shown that $\pi_{13}^{TT}(R2)$ was slightly larger than $\pi_{23}^{TT}(R2)$ in the intermediate wavenumber range. The T_{13}^{TT} term would be large in a vortex oriented at some angle to the wall, such as occurs as the quasi-streamwise vortices lifts away from the wall, forming the "neck" region of the horseshoe vortex, as shown in Figure 5.12(b). As the angle of inclination increases, T_{13}^{TT} replaces T_{23}^{TT} as the predominant contribution of the vortex to the source terms. Thus, the region of T_{13}^{TT} generation should be further from the wall than for T_{23}^{TT}, a conjecture confirmed by Figure 5.13, which shows that the peak of the mean-square distribution of T_{13}^{TT} is at about $y^+ = 25$. The streamwise wavenumber spectra of T_{13}^{TT} at $y^+ = 12$, Figure 5.3, has a peak at $k_x\delta \approx 10$ which corresponds to a streamwise wavelength of about 110 wall units. This is a reasonable wavelength for a pressure footprint generated by the neck region of the horseshoe vortex (*e.g.*, a neck region extending from $y^+ = 20$ out to $y^+ = 120$, at a 45^o angle, would generate a π_{13} footprint approximately 100 wall units long).

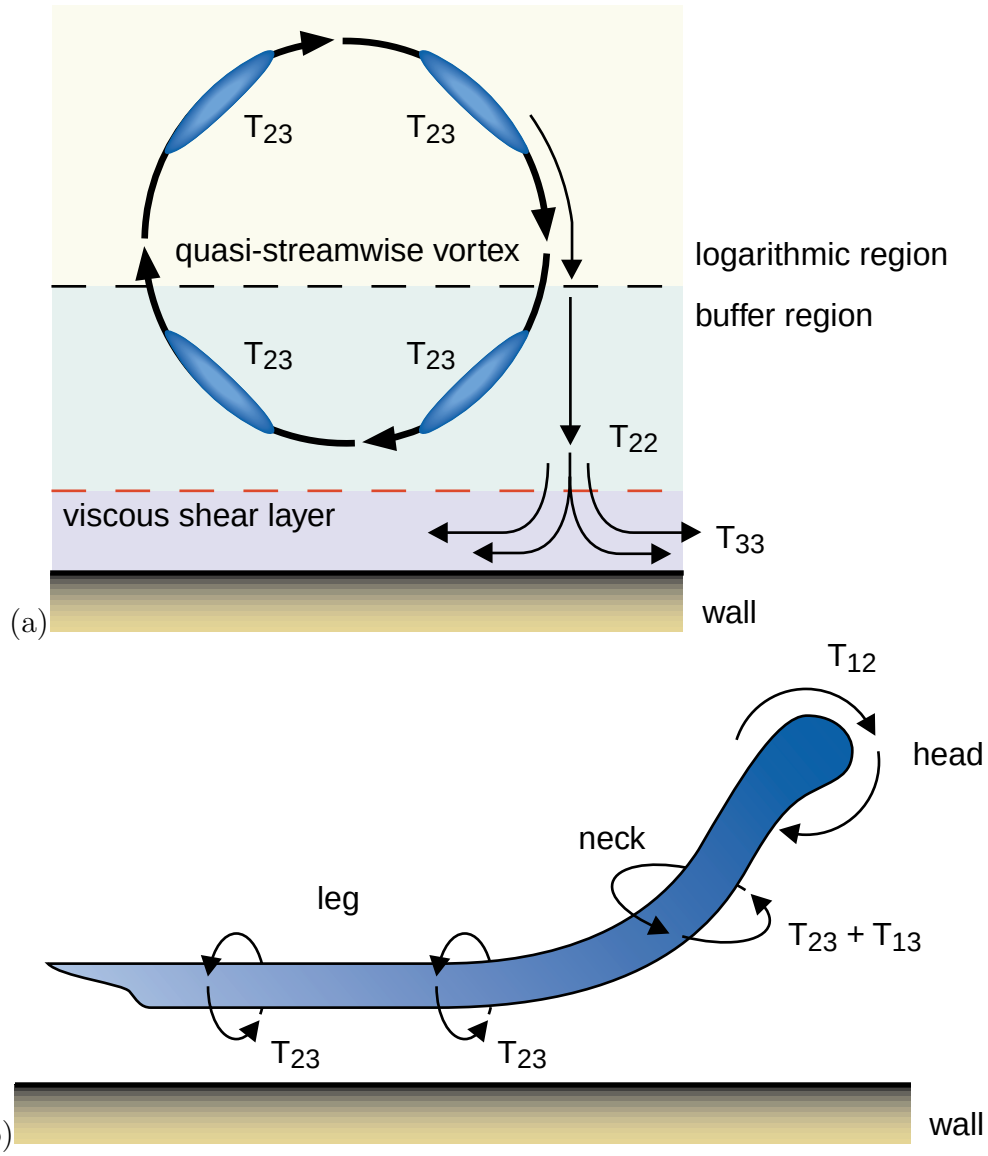

Figure 5.12: Schematic showing the relationship between horseshoe vortices and source terms. (a) End view showing showing regions of high T_{23}^{TT}, T_{22}^{TT} and T_{33}^{TT}; (b) side view showing regions of high T_{23}^{TT}, T_{13}^{TT} and T_{12}^{TT}.

T_{12}^{TT}: Near-wall shear layers and spanwise vortices

In Chapter 4, it was shown that π_{12}^{TT} from the buffer layer is one of the dominant terms for $20 < k_x\delta < 30$. T_{12}^{TT} is the product of $\partial u/\partial y$ and $\partial v/\partial x$ which may be large in near-wall shear layers or spanwise vortices. The spectra of T_{12}^{TT} at various

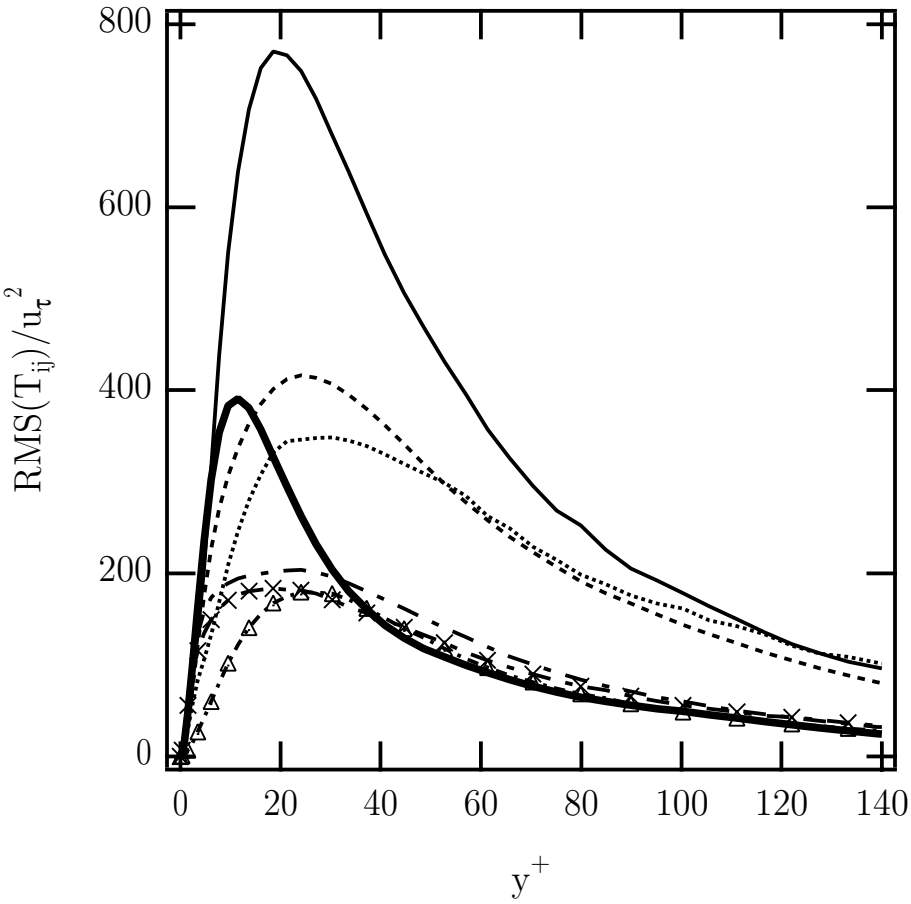

Figure 5.13: Profiles of r.m.s. TT and MS source terms. $\triangle : T_{11}^{TT}$; ..... : $2T_{12}^{TT}$; ---------- : $2T_{13}^{TT}$; $\times : T_{22}^{TT}$; —— : $2T_{23}^{TT}$; – – – : T_{33}^{TT}; ▬▬ : T^{MS}.

wall-normal locations, shown in Figure 5.14, highlight two different behaviors of ϕ_{12}^{TT}:

1. At the inner locations, $y^+ = 5, 12$ and 21, the streamwise spectra has a peak at about $k_x\delta = 10$, corresponding to a $\lambda_x^+ \approx 110$. The spanwise spectra at $y^+ = 5$ has a peak at $k_z\delta = 20$, corresponding to a $\lambda_z^+ \approx 60$; as y^+ is increased the peak in the spanwise spectra disappears, and the energy slowly moves to the lower wavenumbers. The length scales for T_{12}^{TT} can be inferred from the contour plots of uv from Johansson, Alfredsson, and Kim (1988). They show that near-wall shear layers have a region of high uv beneath the

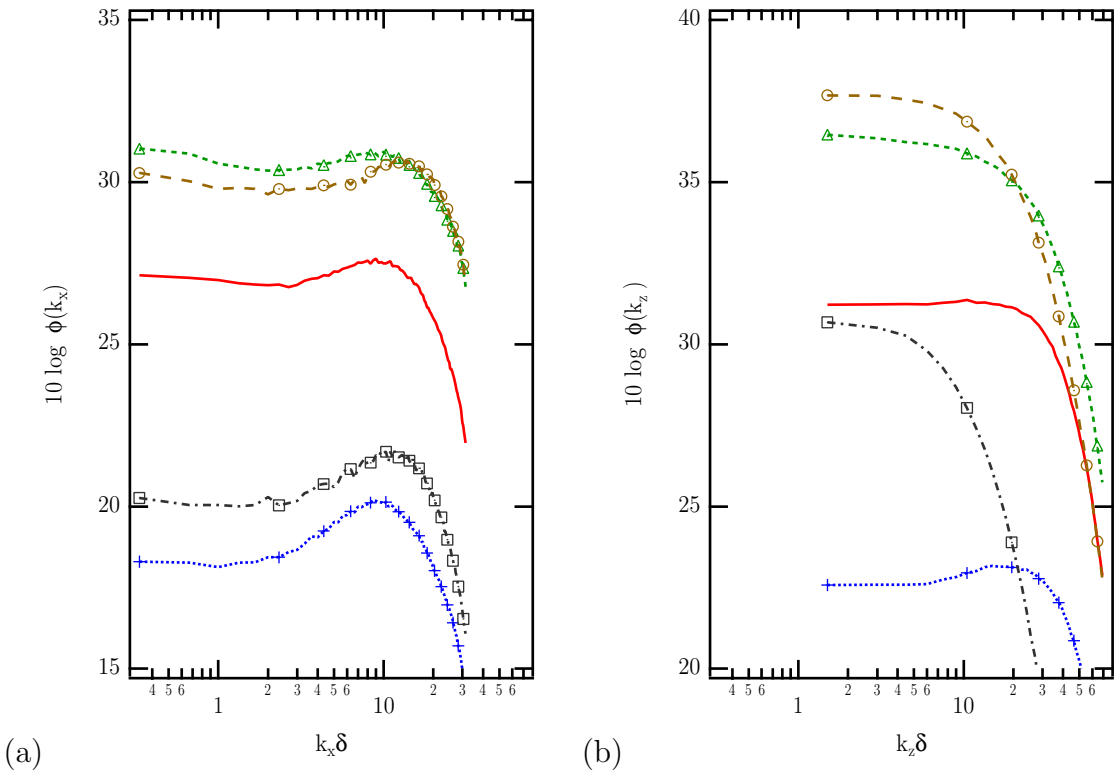

Figure 5.14: One-dimensional spectra of the T_{12}^{TT} source term. + $y^+ = 5$; —— $y^+ = 12$; △ $y^+ = 21$; ○ $y^+ = 49$; ▫ $y^+ = 145$. (a) Streamwise; (b) spanwise. Note exaggerated vertical axis (compared with Figures 5.1 through 5.5 and 5.7).

ejection side of the shear layer from which it can be estimated that the region of high T_{12}^{TT} has streamwise and spanwise length scales on the order of 140 and 60 wall units, respectively. These wavelengths are consistent with the notion that near-wall shear layers generate T_{12}^{TT}. However, at *e.g.*, $y^+ = 12$, ϕ_{12}^{TT} is smaller than ϕ^{MS} by about 8 dB; the reason for this may be that $\partial u/\partial y$ provides much weaker amplification for $\partial v/\partial x$ than does dU/dy.

2. In Figure 5.14 the character of the spectra changes for the outer two locations ($y^+ = 49$ and 145). It can be seen that the streamwise spectra has a slightly more accentuated peak which is centered about $k_x\delta = 12$. This represents a streamwise wavelength of about 75 wall units. The spanwise spectra shifts

to lower wavenumbers as distance from the wall increases; this means that the dominant spanwise wavelengths are very long. This behavior may be due to spanwise vortices. The statistics from Robinson *et al.* (1989) show that most of the spanwise vortices occur for $80 < y^+ < 180$, although there are a significant number closer to wall (*e.g.*, at $y^+ = 50$). The average spanwise vortex diameter at $y^+ = 150$ is about 60 wall units, which compares well with the streamwise wavelength of T_{12}^{TT} at $y^+ = 49$ and 145. However, since these sources have relatively low energy levels (compared with the MS term) and are far from the wall; they are highly attenuated by the Green's function and generate relatively small partial pressures.

Impinging sweeps

As shown in Figure 4.11, the smallest scales of pressure are dominated by π_{23}^{TT}, π_{33}^{TT} and π_{22}^{TT} due to sources in the viscous shear-layer. T_{33}^{TT} and T_{22}^{TT} are comprised of the wall-normal derivative of the wall-normal velocity and the spanwise derivative of the spanwise velocity, respectively. Such terms may be related to the impingement of relatively high-velocity fluid on the wall that occurs on the downward side of a quasi-streamwise vortices as shown in Figure 5.12(a). Impinging flows would create a high wall-normal gradient of the wall-normal velocity, due to the deceleration of the flow as it impinges on the wall, and a high spanwise gradient as the flow spreads out, parallel to the wall. T_{23}^{TT} could also be generated as the flow makes the 90^o bend.

The spectra of T_{33}^{TT}, T_{22}^{TT}, and T_{23}^{TT} at $y^+ = 5$, shown in Figure 5.15 show that the source terms are dominated by low k_x, indicative of long streamwise structures. In the spanwise spectra both T_{33}^{TT} and T_{22}^{TT} have peaks at $k_z\delta \approx 50$,

which indicates that they have significant energy in wavelengths of about 20 wall units; this is a reasonable length scale for the impingement described above. T_{23}^{TT} has very little low wavenumber energy, but has a pronounced peak at $k_z\delta \approx 35$, which corresponds to a spanwise wavelength of about 30 wall units. The T_{23}^{TT} spectra at $y^+ = 5$ is about 17 dB lower than the spectra for $y^+ = 21$, shown in Figure 5.3 and its peak has shifted from $k_z\delta \approx 25$ to $k_z\delta \approx 32$ which may indicate that the quasi-streamwise vortices which extend down into the viscous shear-layer have a smaller spanwise extent and may include a contribution from secondary vortices formed during impingement.

Robinson (1991b) calls near-wall regions, characterized by abruptly diverging streamlines, pockets; their shape is roughly circular in the $x - z$ plane with spanwise dimensions of 50 to 100 wall units; they can be regions where small-scale secondary vortices form. It was not clear to Robinson (1991b) what the generation mechanism for pockets was, although sweeps were the most likely candidate for their generation. Our data indicate that, in particular, T_{23}^{TT} and T_{33}^{TT} are much longer in the streamwise direction and narrower in the spanwise direction than indicated by Robinson's (1991b) description of pockets and thus, they may not be generated by the same mechanisms.

5.3 Summary

In summary, the MS source spectra strongly indicates that the MS pressure is generated by near-wall shear layers. Both the dominant length scales from the the MS spectra and the MS partial pressure compare very well with data from conditionally sampled near-wall shear layers. Since previous studies have linked

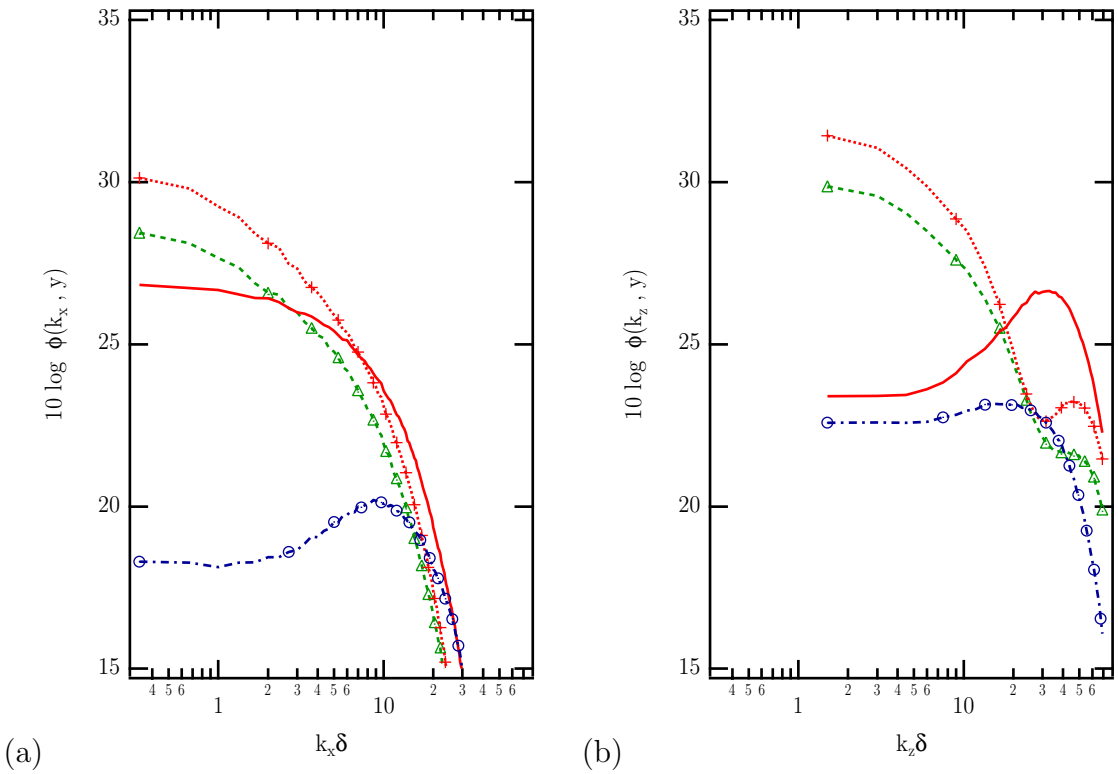

Figure 5.15: One-dimensional spectra of source terms from the viscous shear-layer, $y^+ = 5$. —— T_{23}^{TT}; + T_{33}^{TT}; △ T_{22}^{TT}; ∘ T_{12}^{TT}. (a) Streamwise (b) spanwise.

near-wall shear layers to the occurence of high-amplitude wall pressure events, it can be hypothesized that the MS partial pressure is primarily generated by these events.

The dominant TT terms occur in the buffer layer. The terms which contribute most to the wall pressure are T_{23}^{TT} and T_{13}^{TT}, which occur in quasi-streamwise vortices that are parallel to, or at an angle to the wall. T_{12}^{TT}, which was shown in the previous chapter to make only minor contributions to the pressure, is due to near-wall shear layers in the buffer layer, and spanwise vortices, in the logarithmic region. In both cases, however, it is not a very efficient generator of wall pressure.

In the viscous shear-layer T_{23}^{TT}, T_{22}^{TT} and T_{33}^{TT} are important and appear to be generated by the downward side of quasi-streamwise vortices which impinge on the

wall. These account for the highest spanwise wavenumber partial pressures.

Chapter 6

Some aspects of MS pressure modelling

One practical application of the knowledge gained from the study of WPFs is in the field of flow-induced radiated noise; noise prediction is of importance in the design and analysis of turbomachinery, where the blade trailing edges are a primary noise source. Radiated noise is related to the wall pressure through an Helmholtz equation with a solution that is the surface integral of the wall pressure spectral density and the wall-normal derivative of a Green's function for the surface [Blake, Lee and Zawadski (1998)]. At the design stage, which relies extensively on the solution of the Reynolds-averaged Navier-Stokes (RANS) equations to obtain the velocity fields, to obtain the radiated noise, some model must be employed that uses only the averaged quantities (velocity, pressure and Reynolds stresses) that are available from RANS calculations. Such models were developed by Blake (1971,1986), Chase (1980) and Zawadski *et al.* (1996), using experimental data, theoretical considerations and scaling arguments. The database generated in this study allows us to compute term-by-term the assumptions required by these models, and evaluate them directly.

An expression for the MS pressure spectrum for a turbulent one-dimensional

mean flow was developed first by Lilley (1960) and modified by Blake (1971,1986), Zawadski *et al.* (1996) and Blake *et al.* (1998). In this formulation the spectrum is given in terms of the double wall-normal integral of the product of the mean shear (dU/dy) and the wall-normal turbulence intensities, with additional factors such as the one-dimensional streamwise and spanwise wavenumber spectra and wall-normal correlation of the wall-normal velocity. The mean-shear can be obtained directly from RANS computations with the wall-normal turbulence intensities estimated from the RANS turbulence model. The shortcomings of this model are: first, it assumes one-dimensional mean flow; second, only the MS term is modelled, whereas the TT term is neglected. Regarding the first shortcoming, the MS term is the expansion of $\frac{\partial U_i}{\partial x_j}\frac{\partial u_j}{\partial x_i}$; for a three-dimensional mean flow this results in nine terms. As will be seen, there is no accurate model even for the single term that appears for one-dimensional mean flows. Thus, part of a modelling effort would be to determine how to apply a one-dimensional model in a three-dimensional flow. Regarding the second shortcoming, it was shown in Chapter 4 that the one-dimensional MS pressure spectra is slightly larger than the TT pressure at all but the highest spanwise wavenumbers, and its spectra has the same shape as the total pressure, and is lower by a few decibels. Thus, the MS pressure may provide a reasonable approximation to the total pressure.

In this chapter, we review the formulations of Blake (1986), Chase (1980) and Zawadski *et al.* (1996), restate their formulations for channel flow, and evaluate their various levels of approximation. Then, we shall study the one-dimensional streamwise and spanwise spectra and broadband wall-normal correlation coefficient of v, which are factors in the formulations that can only be modelled with knowledge of turbulent velocity fields, and are conveniently computed from the

DNS database.

6.1 MS model formulation

The solution to the Poisson equation for fluctuating pressure for channel flow was derived in Section 2.6. Ignoring the boundary terms (in Section 4.2 it was shown that the Stokes pressure was very small compared with the total pressure, except at the highest spanwise wavenumbers), the solution is given in wavenumber-frequency space by

$$\widehat{p}(y,\mathbf{K},\omega) = -\int_{-1}^{1} \widehat{T}^{tot}(y,\mathbf{K},\omega) g(y,K,\omega) dy, \tag{6.1.1}$$

where the Green's function evaluated at the near-wall is given by

$$g(K,y) = \frac{\cosh[K(1-y)]}{K\sinh(2K)}. \tag{6.1.2}$$

The only differences between the channel flow and boundary layer solutions is the Green's function, which for a boundary-layer is e^{-Ky} and the limits of integration, $[0,\infty]$.

The spectral density (amplitude) of the wall pressure is given by multiplication of the complex spectra (6.1.1) by its complex conjugate

$$\Pi^{tot}(\mathbf{K},\omega) = \frac{|\hat{p}^*(\mathbf{K},\omega)\,\hat{p}(\mathbf{K}',\omega')|}{\delta\left(\mathbf{K}-\mathbf{K}'\right)\delta\left(\omega-\omega'\right)}. \tag{6.1.3}$$

The δ functions indicate that the function need only be evaluated at $\mathbf{K}=\mathbf{K}'$ and $\omega=\omega'$. The spectral density for the wall pressure in terms of (6.1.1) is given by

$$\Pi^{tot}(\mathbf{K},\omega) = \left| \int_{-1}^{1} dy\; g(y) \left[\hat{T}^{TT*}(y) + \hat{T}^{MS*}(y)\right] \int_{-1}^{1} dy' g(y') \left[\hat{T}^{TT}(y') + \hat{T}^{MS}(y')\right] \right| \tag{6.1.4}$$

It is understood that the arguments in the right-hand-side of (6.1.4) are actually $(y, \mathbf{K}, \omega)$ or $(y', \mathbf{K}, \omega)$. The wall-normal integration in (6.1.1) must be over separate dummy integration variables, leading to a double integration in the wall-normal direction. One could also evaluate $\hat{p}^*(0, \mathbf{K}, \omega)$ and $\hat{p}(0, \mathbf{K}', \omega')$ separately, then take their amplitude, thus avoiding the complications involved with the double wall-normal integration. Such an approach, however, does not lead to a form involving the product of the wall-normal correlations and turbulence intensities, which make the MS term at all possible to model. Multiplication of the terms in (6.1.4) gives

$$\Pi^{tot}(\mathbf{K}, \omega) = \left| \int_{-1}^{1} dy \int_{-1}^{1} dy'\, G(y, y') \left[\hat{T}^{TT*}(y) \hat{T}^{TT}(y') + \hat{T}^{MS*}(y) \hat{T}^{MS}(y') + \hat{T}^{C} \right] \right| \tag{6.1.5}$$

where $G(y, y') \equiv g(y)g(y')$ and $\hat{T}^C$ represents the cross terms given by

$$\hat{T}^{C}(y, y') = \hat{T}^{TT*}(y) \hat{T}^{MS}(y') + \hat{T}^{TT}(y') \hat{T}^{MS*}(y). \tag{6.1.6}$$

We now focus on modelling the MS term spectral density which is given by the second term in (6.1.5),

$$\Pi^{MS}(\mathbf{K}, \omega) = \left| \int_{-1}^{1} dy \int_{-1}^{1} dy' G(y, y')\, \hat{T}^{MS*}(y) \hat{T}^{MS}(y') \right|. \tag{6.1.7}$$

The Fourier transform of the MS source term can be expressed as

$$\hat{T}^{MS}(y, \mathbf{K}, \omega) = 2\tau(y) i k_x \hat{v}(y, \mathbf{K}, \omega), \tag{6.1.8}$$

where

$$\tau(y) \equiv \frac{dU}{dy}. \tag{6.1.9}$$

Substituting (6.1.8) into (6.1.7) gives

$$\Pi^{MS}(\mathbf{K}, \omega) = 4k_x^2 \left| \int_{-1}^{1} dy \int_{-1}^{1} dy'\, G(y, y')\, \tau(y) \tau(y') \hat{v}^*(y, \mathbf{K}, \omega) \hat{v}(y', \mathbf{K}, \omega) \right|, \tag{6.1.10}$$

which is an exact representation of the MS spectral density and still contains the turbulent quantity v. The challenge for various modellers [*e.g.*, Chase (1980), Zawadski *et al.* (1996), Blake *et al.* (1998)] has been to model $\hat{v}^*(y, \mathbf{K}, \omega)\hat{v}(y', \mathbf{K}, \omega)$ using empirical knowledge of turbulence.

Modelling the vertical velocity

Blake (1986) defines $\Phi_{22}(y, y', \mathbf{K}, \omega)$, the cross spectral density of the normal component of fluctuating velocity between wall distances y and y', to be

$$\Phi_{22}(y, y', \mathbf{K}, \omega) \equiv \left|\hat{v}^*(y, \mathbf{K}, \omega)\hat{v}(y', \mathbf{K}, \omega)\right|. \tag{6.1.11}$$

If the magnitude operation in (6.1.10) is brought inside the integral, then the MS wall pressure spectral density (6.1.10) can be expressed in terms of the cross spectral density,

$$\Pi^{MS}(\mathbf{K}, \omega) = 4k_x^2 \int_{-1}^{1} dy \int_{-1}^{1} dy' G(y, y')\tau(y)\tau(y')\Phi_{22}(y, y', \mathbf{K}, \omega) \tag{6.1.12}$$

The mathematical difference between forms (6.1.10) and (6.1.12) is that in (6.1.10) the integrals of the complex spectra are taken, then the magnitude, whereas, in (6.1.12) the magnitude is taken first, then the integrals. This would yield the same results if the product of $\widehat{v}(\mathbf{K}, y)^*\widehat{v}(\mathbf{K}, y')$ were real, as is the case at $y' = y$. However, for $y' \neq y$, the product is complex and form (6.1.12) ignores cross terms that would appear in the integration of a complex function. The error involved in this approximation will be quantified later.

A further simplification is to express the cross spectral density function in product form

$$\Phi_{22}(y, y', \mathbf{K}, \omega) \approx R_{22}(y, y')\Phi_{22}(y, \mathbf{K}, \omega). \tag{6.1.13}$$

$\Phi_{22}(y, \mathbf{K}, \omega)$ is the spectral density of wall normal velocity at a single level, y, while

$$R_{22}(y, y') \equiv \frac{\langle v(y)\, v(y') \rangle}{\langle v^2(y') \rangle}, \tag{6.1.14}$$

is the broadband wall-normal correlation function (so-called because it is integrated over all wavenumbers and frequencies), which contains the relationship between the velocity at y and y'. Furthermore, $\Phi_{22}(y, \mathbf{K}, \omega)$ can be approximated as the product of three one-dimensional functions

$$\Phi_{22}(y, \mathbf{K}, \omega) \approx \tilde{\phi}^x_{vv}(k_x) \tilde{\phi}^z_{vv}(k_z) \phi^m_{vv}(\omega - k_x\, U_c) \left\langle v^2(y) \right\rangle. \tag{6.1.15}$$

$\tilde{\phi}^x_{vv}(k_x)$ and $\tilde{\phi}^z_{vv}(k_z)$ are the one-dimensional, normalized wavenumber spectra of v, defined below. $\phi^m_{vv}(\omega - k_x\, U_c)$ is the moving-axis spectrum which is a functional form for the distribution of energy away from the convective ridge (in the $k_x - \omega$ plane) for the energy in the vertical velocity. If Taylor's hypothesis is invoked, then ϕ^m_{vv} becomes a delta function at each value of ω

$$\phi_m(\omega - k_x\, U_c) = \delta(\omega - k_x\, U_c). \tag{6.1.16}$$

This considerably simplifies the integration of (6.1.12) over all ω to obtain the planar wavenumber spectra, since

$$\int_{-\infty}^{\infty} \delta(\omega - k_x\, U_c)\, d\omega = 1. \tag{6.1.17}$$

Invoking Taylor's hypothesis does not affect the results presented herein since we are only investigating the one-dimensional spectra, which are obtained by integration of the three-dimensional spectra over all frequencies and one of the wavenumber directions. Thus, since the convective ridge dominates the entire wavenumber-frequency domain, the one-dimensional spectra reflect mostly the energy in the convective ridge. If more detail about the subconvective wavenumber pressures are desired then a more complex functional form for ϕ^m_{vv} needs to be determined.

The functions $\tilde{\phi}^x_{vv}(k_x, y)$ and $\tilde{\phi}^z_{vv}(k_z, y)$ are the normalized spectra,

$$\tilde{\phi}_{vv}(k_x, y) \equiv \frac{\phi(k_x, y)}{\int_0^\infty dk_x \, \phi_{vv}(k_x, y)}; \tag{6.1.18}$$

$\tilde{\phi}^z_{vv}(k_z, y)$ is normalized in a similar manner. By Parseval's theorem,

$$\left\langle v^2(y) \right\rangle = \frac{1}{L_x L_z} \int_0^{L_z} dz \int_0^{L_x} dx \, v^2(x, y, z) = \int_0^\infty dk_x \, \phi_{vv}(k_x, y). \tag{6.1.19}$$

Using (6.1.15) in (6.1.13), and placing the result in (6.1.12) gives an approximate form for the MS pressure:

$$\Pi^{MS}(\mathbf{K}) \approx 4k_x^2 \int_{-1}^{1} dy \int_{-1}^{1} dy' G(y, y') \tau(y) \tau(y') \left\langle v^2(y) \right\rangle R_{22}(y, y') \tilde{\phi}^x_{vv}(k_x) \tilde{\phi}^z_{vv}(k_z). \tag{6.1.20}$$

This will be referred to as the "3-term" form. Note that RANS calculations would yield $\langle v^2(y) \rangle$ and $\tau(y)$, but all the other terms require further modelling.

Comparison of approximate forms

Figure 6.1 compares the exact (6.1.7), CSD (6.1.12) and the 3-term separable (6.1.20) forms. Results are averaged from about 80 realizations of DNS5. The differences between the various forms are quite small and occur primarily at the lowest wavenumbers. The difference between the exact and CSD forms shows the effect of moving the magnitude operation from outside the integral (6.1.7) to inside (6.1.12). The difference between the CSD and 3-term forms show the difference between evaluating the four-dimensional $\Phi(y, y', \mathbf{K})$ and the product of one-dimensional spectra.

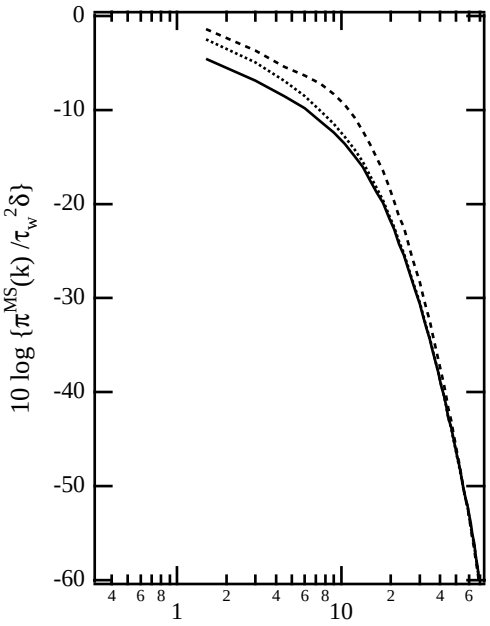

(a) (b)

Figure 6.1: Comparison of π^{MS} computed with three levels of approximation. (a) Streamwise, (b) spanwise spectra. Normalized by $\tau_w^2\delta$. —— : Exact (6.1.7); ..... : CSD (6.1.12); - - - - - - - - : 3-term (6.1.20).

6.2 Characteristics of vertical velocity

In this section we study the characteristics of the one-dimensional spectra and broadband correlations of v. Such information is necessary for forms involving evaluation of the spectra at characteristic wall-normal locations *e.g.*, it may be necessary to model (see Zawadski *et al.* (1996)) the wall-normal velocity spectra based on a single, characteristic location $y = y_c$, *i.e.*,

$$\Pi^{MS}(\mathbf{K}) \approx \int_{-1}^{1} dy \int_{-1}^{1} dy' H\left(\mathbf{K}, y, y'\right)\ R(y,y')\phi_{22}(y_c,k_x)\phi_{22}(y_c,k_z)\left\langle v^2(y)\right\rangle. \tag{6.2.1}$$

Traces of $\tilde{\phi}_{22}(y,k_x)$ and $\tilde{\phi}_{22}(y,k_z)$ at various y locations are shown in Figure 6.2. It is immediately apparent from the k_x spectra that $\tilde{\phi}_{22}(y,k_x)$ is practically constant with y. The cut at $y^+ = 145$ shows a small divergence at the lowest wavenumbers,

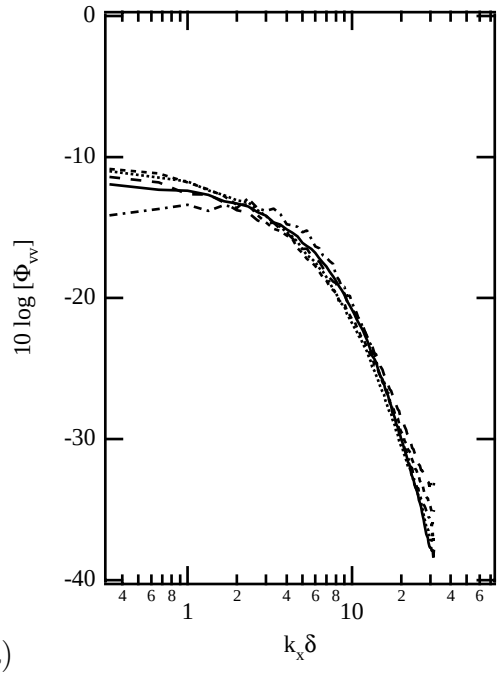

(a) (b)

Figure 6.2: Constant y^+ cuts of $\tilde{\phi}_{22}(y, \mathbf{K})$. (a) Streamwise (b) spanwise. —— : $y^+ = 5$; ····· : $y^+ = 12$; - - - - - : $y^+ = 21$; – – – – : $y^+ = 49$; –·– : $y^+ = 145$.

but for the purposes of modelling, this difference may be insignificant. On the other hand the k_z spectra shows marked differences with y, although all the curves appear to have similar shapes. The peak of the spectra moves from higher to lower values of k_z as y is increased.

Contour plots of the spectra in (k_x, y^+) and (k_z, y^+) space, Figure 6.3, show the distribution of energy as a function of wavenumber and wall-normal distance. Superimposed on top of the plot are the maxima found using a peak-detection algorithm. As shown in Figure 6.2, the peaks are very broad, so the trace of the maxima is only an approximation. In any case it can be seen that the k_x spectra are fairly constant in y, and it might be safe to assume that a characteristic of $\phi_{22}(y, k_x)$ can be taken from almost anywhere in the boundary layer. In the viscous shear-layer, k_z spectra have a peak at about $k_z\delta = 12$; the peak then migrates to lower k_z as y increases away from the viscous shear-layer.

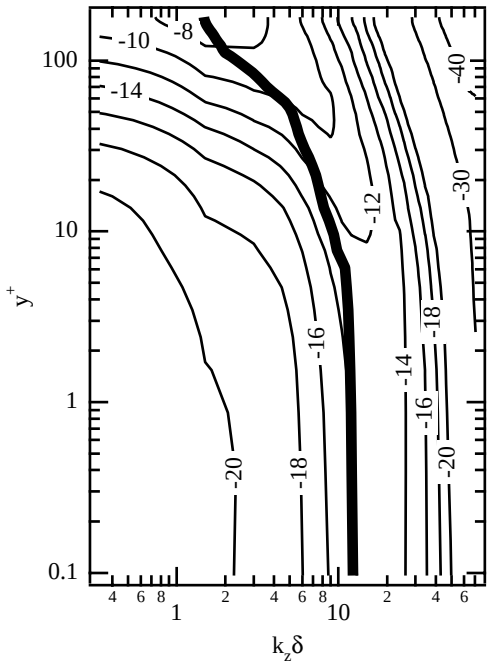

Figure 6.3: Contour plot of spanwise wavenumber spectra, $\tilde{\phi}_{22}(y, k_z)$. The thick line denotes the trace of the maxima.

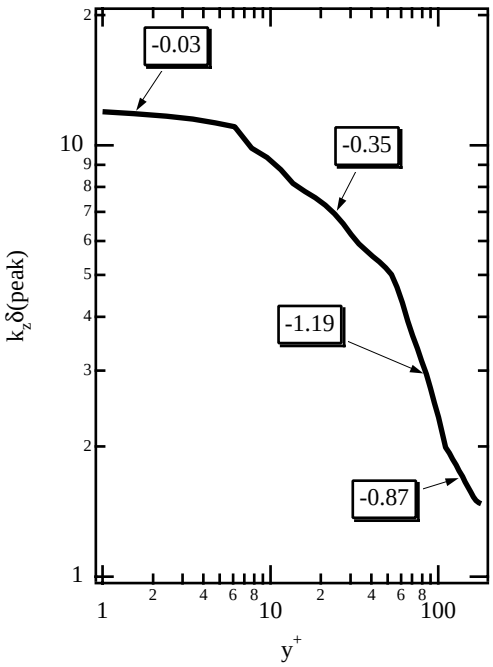

Figure 6.4: Peak k_z values of $\tilde{\phi}_{22}(y, k_z)$, as a function of y^+. Labels show the values of n for the y^n behavior of the various zones.

Region	$y^+{}_{min}$	$y^+{}_{max}$	n	approximation
1	0	6	-0.03	0
2	6	50	-0.35	$-1/3$
3a	50	110	-1.19	-1
3b	110	180	-0.87	-1

Table I: Wall-normal regions for $\phi_{22}(y, k_z)$ peak locations. n is the exponent in the relationship $k_z\delta = y^n$.

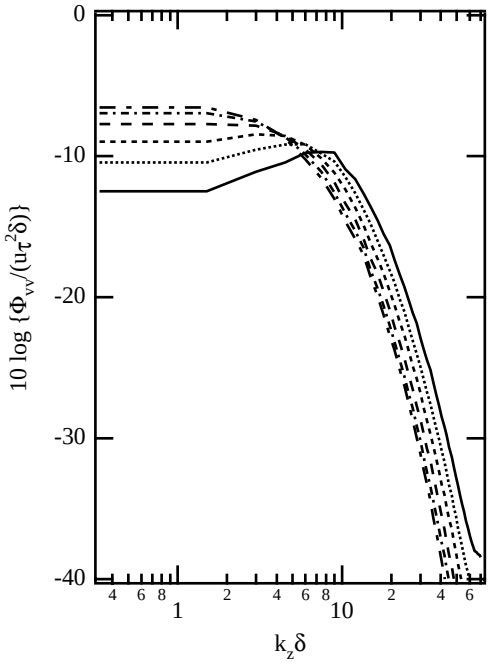

Figure 6.5: $\tilde{\phi}_{22}(y, k_z)$ in the logarithmic region plotted *vs.* $k_z\delta$. ——— : $y^+ = 53$; ····· : $y^+ = 75$; ---------- : $y^+ = 100$; – – – – : $y^+ = 128$; –·– : $y^+ = 151$; – – – : $y^+ = 174$.

Figure 6.4(b) shows the location of the peak of the spanwise wavenumber spectra. The curve presents sharp changes in behavior at $y^+ = 6$, 50 and 110. Within each layer, it can be described by a power-law behavior, y^n, with a constant exponent. The exponents obtained by fitting the data are shown in Table I; an approximate power-law behavior is also proposed. Note that in the logarithmic region and beyond, Morrison and Kronauer (1969) proposed a y^{-1} behavior for two-dimensional spectra of u, which is consistent with the present data.

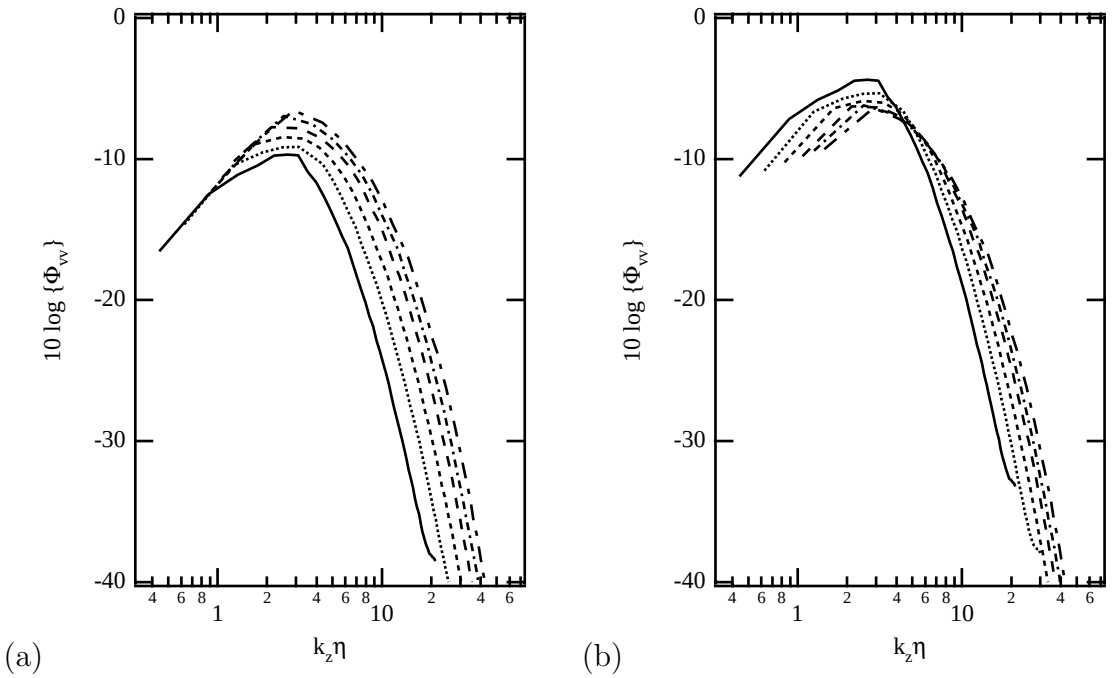

Figure 6.6: $\phi_{22}(y, k_z)$ in the logarithmic region, plotted *vs.* $k_z\eta$, normalized by (a) $\langle v^2(\eta)\rangle$, (b) $\langle v^2(\eta)\rangle\,\eta$. —— $y^+ = 53$; ····· $y^+ = 75$; - - - - - $y^+ = 100$; – – – – $y^+ = 128$; –·– $y^+ = 151$; – – – $y^+ = 174$.

Figure 6.5 shows the spanwise wavenumber spectra from five locations in the logarithmic region; the peak moves to lower wavenumbers and becomes higher and less pronounced, as y increases. The high wavenumber tail moves in a similar fashion toward lower wavenumbers as y increases. This indicates that the spectra may scale like $k_z y$.

Morrison and Kronauer (1969) claimed that their u spectra could be expressed in product form

$$\Pi(\omega^+, K^+ y^+) = f(K^+ y^+) A(\omega^+, k_z^+) \tag{6.2.2}$$

where $^+$ denotes normalization by viscous variables ($\omega^+ \equiv \omega\nu/u_\tau$, $K^+ \equiv K\nu/u_\tau$). f is called the "wave intensity function" and A is the "wave strength." This implies that for a range of wall-normal locations, their data collapsed to a single curve when plotted *vs.* $K^+ y^+$. We showed previously that the peak locations

of the spanwise wavenumber spectra scale accordingly. Figure 6.5 shows that at wavenumbers higher than the peak, the spectra decrease with distance from the wall. This would lead one to believe that the abscissa, multiplied by η ($\eta \equiv 1 + y$ is the distance from the wall), would collapse the high wavenumber spectra to a single curve. Figure 6.6(a) shows that the logarithmic region spectra, normalized by $\langle v^2(y) \rangle$, plotted versus $k_z\eta$ has all the peaks lined up at a single location, $k_z\eta = 3$. While the lowest wavenumbers collapse to a single curve, the spectral levels at wavenumbers higher than the peak tend to increase with y. It would seem that normalizing ϕ_{22} by η may collapse the data. Figure 6.6(b) shows that $\phi_{22}(k_z)$, normalized by $\langle v^2(y) \rangle \, \eta$ moves the curves for various y^+ closer together, but that in the high wavenumbers the spectra values increase with increasing y^+.

Broadband correlation function

In the 3-term formulation (6.1.20), the broadband correlation function $R_{22}(y, y')$, characterizes the relationship between the vertical velocities at different wall-normal locations. Zawadski *et al.* (1996) showed that for a range of vertical locations $8 \leq y^+ \leq 60$, $R_{22}(y, y')$, normalized by the m.s. value at the fixed point, $\langle v^2(y') \rangle$, collapsed to a single curve for $y \leq y'$, when plotted against y/y' (y' held fixed, while y varied). The correlations were computed by the formula,

$$R_{22}(y, y') = \frac{\langle v(y) v(y') \rangle}{\langle v^2(y') \rangle}, \tag{6.2.3}$$

from 60 realizations of DNS5 data. Figure 6.7 shows that for y' in the viscous shear-layer and buffer layer this results in $R_{22}(y, y')$ values greater than 1.0. When plotted against y/y', Figure 6.7(b), the curves collapse for $y/y' \leq 1.0$ consistent with the findings of Zawadski *et al.* (1996). It can be seen that for $y/y' > 1.0$

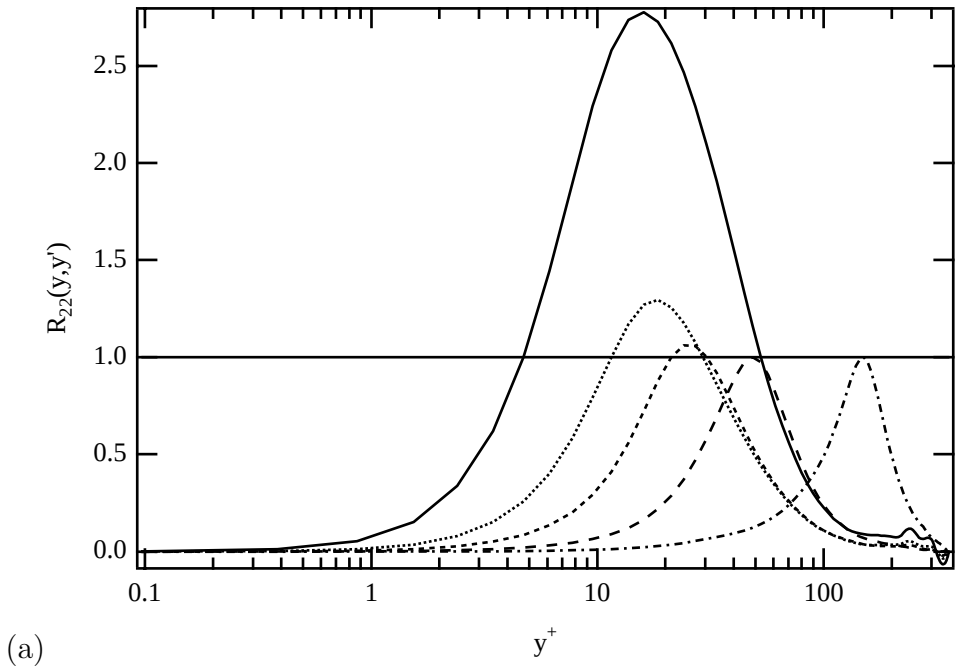

(a)

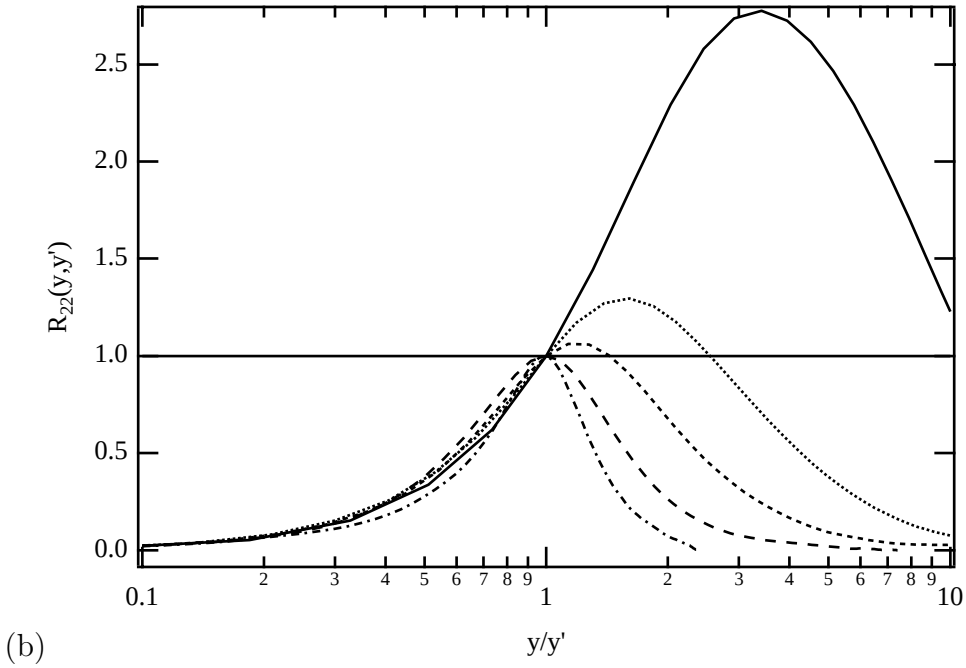

(b)

Figure 6.7: Broadband wall-normal correlations of v normalized by $\langle v^2(y')\rangle$. —— $y^{+\prime} = 5$; ····· $y^{+\prime} = 13$; ----- $y^{+\prime} = 21$; – – – $y^{+\prime} = 49$; –·– $y^{+\prime} = 151$. Plotted against (a) y^+ (b) y/y'.

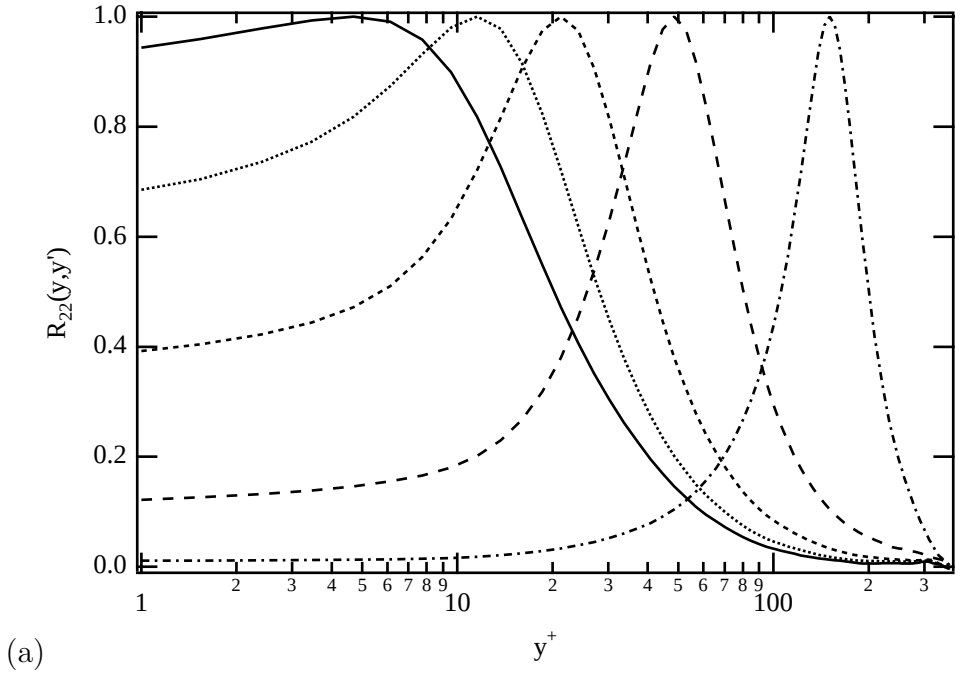

(a)

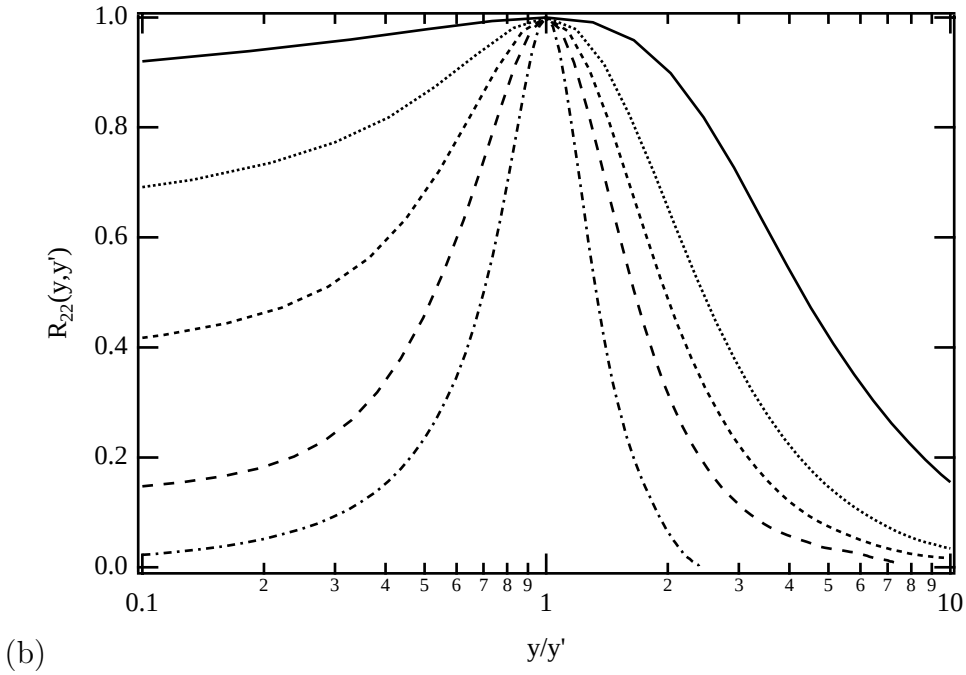

(b)

Figure 6.8: Broadband wall-normal correlations of v normalized by $\langle v^2(y)\rangle^{1/2}\langle v^2(y')\rangle^{1/2}$. —— $y^{+\prime}=5$; ····· $y^{+\prime}=13$; - - - - $y^{+\prime}=21$; – – – – $y^{+\prime}=49$; –·– $y^{+\prime}=151$. Plotted against (a) y^+ (b) y/y'.

the curves diverge from each other, with the greatest amount of divergence for the smallest values of y'.

Normalizing by the r.m.s. values from each of the two levels

$$R_{22}(y, y') = \frac{\langle v(y)v(y')\rangle}{\langle v^2(y)\rangle^{1/2}\langle v^2(y')\rangle^{1/2}}, \tag{6.2.4}$$

gives correlations with the property $R_{22}(y, y') \leq 1.0$. The correlations are shown in Figure 6.8 for a range of y' values throughout the channel. Figure 6.8(a) shows that plotting the correlations plotted against y/y' does not collapse them to a single curve. More work is necessary to determine how the correlations might be modelled.

Narrowband correlation function

The narrowband correlation functions provide wall-normal information at particular wavenumbers. They were normalized by the m.s. value at the fixed point, y':

$$R_{22}(y, y', \mathbf{K}) = \frac{\langle v(y, \mathbf{K})v(y', \mathbf{K})\rangle}{\langle v^2(y', \mathbf{K})\rangle}, \tag{6.2.5}$$

Figure 6.9 are plots of the narrowband correlations for four wavenumbers plotted *vs.* y^+. The four wavenumber pairs $(k_x\delta, k_z\delta)$, (3,4.5), (7,7.5), (16,15) and (30,45), were selected to cover a wide range of wavenumbers. As can be seen from Figure 6.9, the correlations get narrower as K increases, a result that is not unexpected since the higher wavenumbers are attenuated by the Green's function to a greater extent than the lower ones. As with the broadband correlations, the peak location can be collapsed by plotting against y/y'. Figure 6.10, plots of of narrowband correlations plotted *vs.* y/y', show that, as with the broadband correlations, for $y/y' < 1$, there is collapse of the data, particularly for $K = 22$.

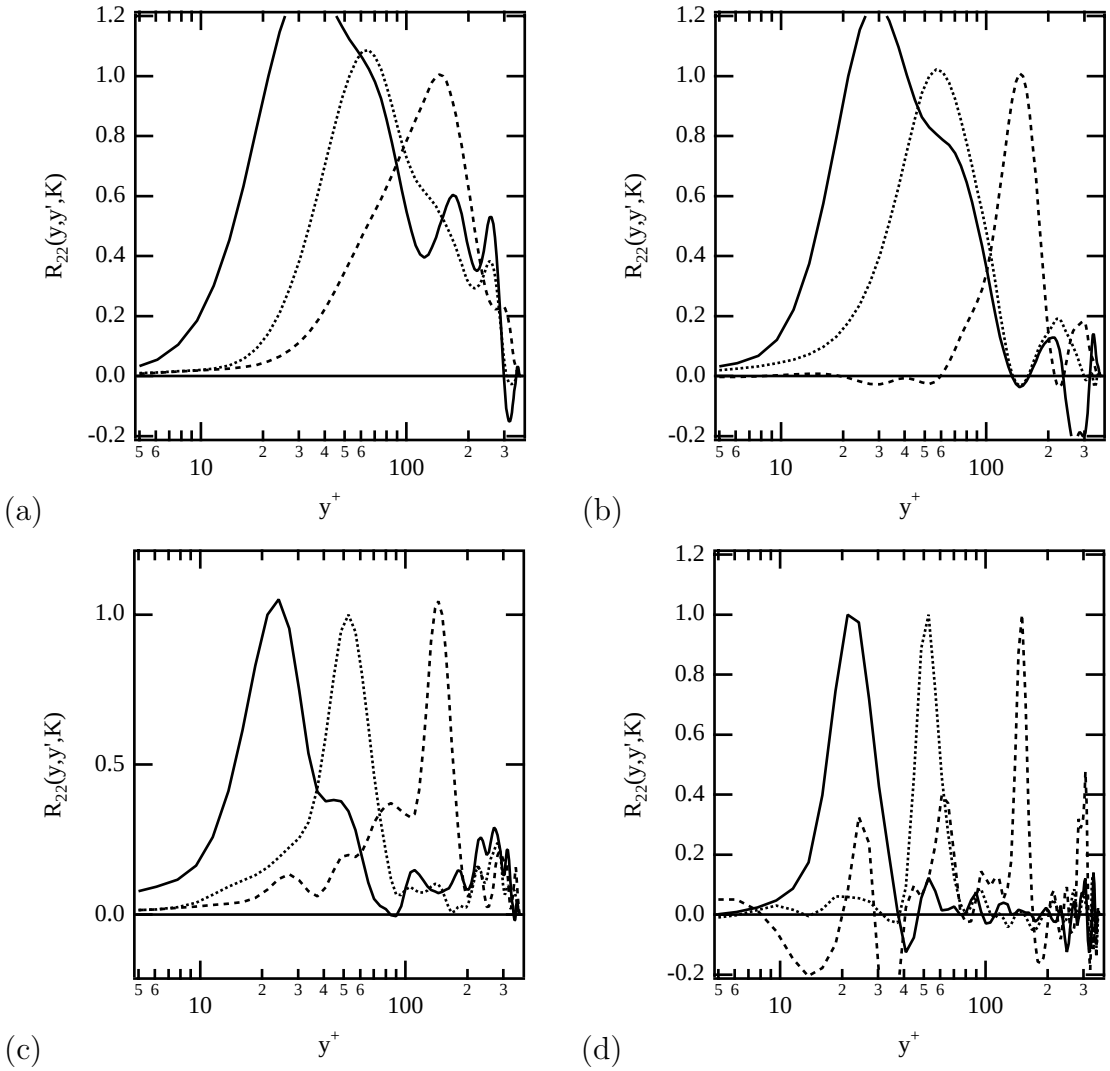

Figure 6.9: Narrowband wall-normal correlations of v normalized by $\langle v^2(y', \mathbf{K})\rangle$ plotted *vs.* y^+. —— $y^{+\prime} = 21$; ····· $y^{+\prime} = 53$; - - - - - $y^{+\prime} = 152$. At wavenumbers (a) $K = 5.4$, (b) $K = 10.3$, (c) $K = 22$, and (d) $K = 54$.

6.3 Summary

In this chapter, we compared the MS pressure computed using the various levels of approximation from the formulation of Blake (1971). Results showed that moving the magnitude operation from outside to inside the wall-normal integrals, so that the cross spectral density function could be used, increases the MS pressure by a

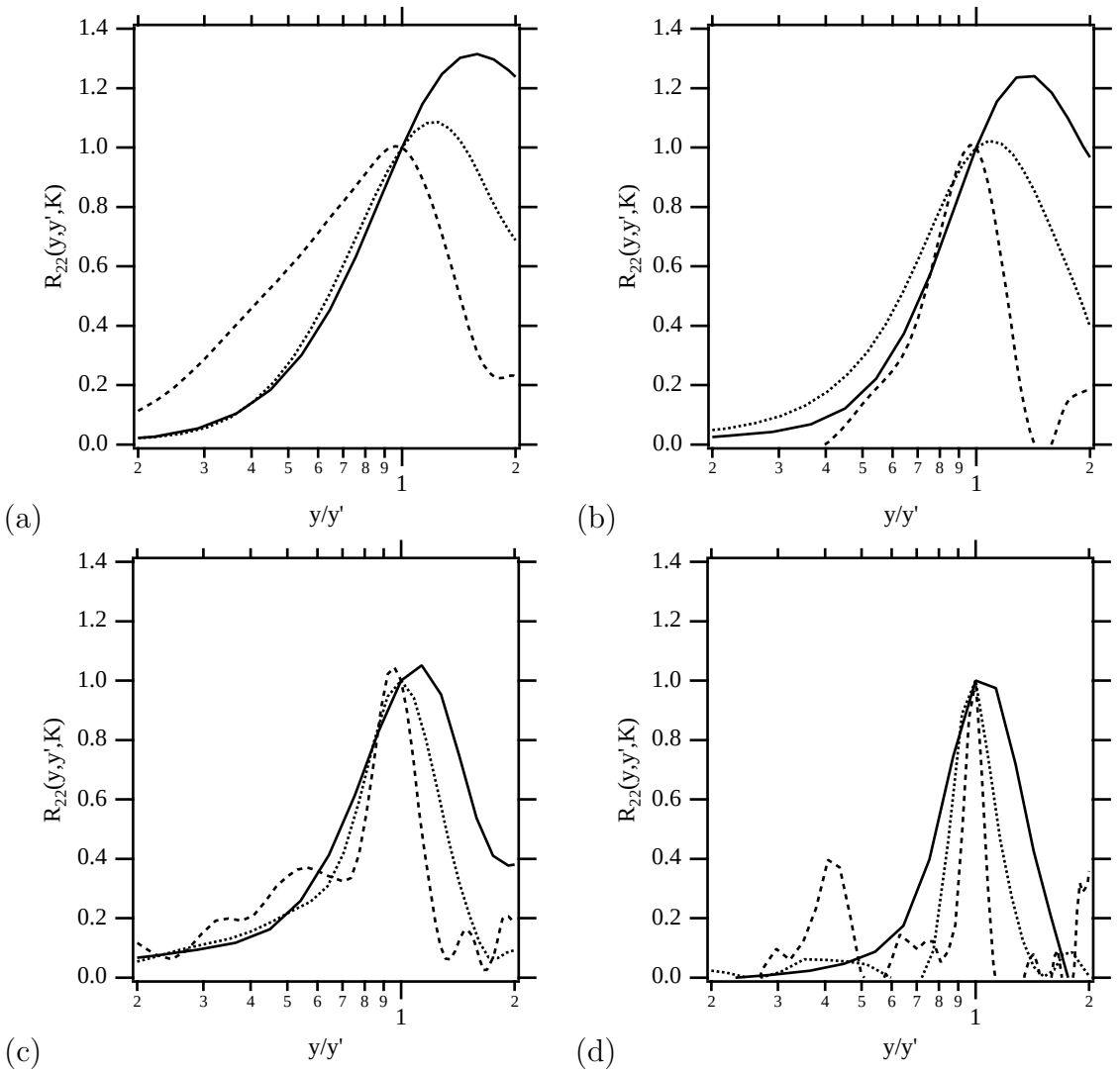

Figure 6.10: Narrowband wall-normal correlations of v normalized by $\langle v^2(y', \mathbf{K})\rangle$ plotted *vs.* y/y'. —— $y^{+\prime} = 21$; ····· $y^{+\prime} = 53$; - - - - - $y^{+\prime} = 152$. At wavenumbers (a) $K = 5.4$, (b) $K = 10.3$, (c) $K = 22$, and (d) $K = 54$.

few dB; expressing the cross spectral density function in terms of products further increases the MS pressure by a few dB. In both cases, the character of the MS pressure spectra was not altered. It can be concluded that the formulation of Blake (1971) is not significantly different from the actual MS pressure and may be a good starting point for further modelling efforts.

We studied the characteristics of the one-dimensional spectra of v and broad-

band correlation functions, which are the functions which must be modelled in the MS pressure formulation. We found that the streamwise spectra, normalized by $\langle v^2(y)\rangle$, varies only slightly throughout the channel and that a characteristic spectra can be taken from almost anywhere. On the other hand, the spanwise spectra, normalized by $\langle v^2(y)\rangle$, varies across the channel, but in a way that can potentially be modelled: the shapes of the spectra appear to be similar and the wavenumber location of the spectra peak varies by powers of y, in discrete regions of the channel. An unsuccessful attempt was made at finding a normalization that would collapse the spanwise wavenumber spectra. The broadband correlation functions were shown for locations throughout the channel. When normalized by the m.s. value at the fixed point, $\langle v^2(y')\rangle$, the correlations appear to collapse for $y/y' < 1$.

Chapter 7

Concluding Remarks

7.1 Summary and conclusions

The motivation for this investigation was to answer some longstanding questions about the sources of wall pressure. Namely, where in the boundary layer are the dominant sources, what are the physical mechanisms of these sources, and what are the relative magnitudes of the mean-shear (MS) and turbulence-turbulence (TT) interaction terms. Using the velocity fields from a direct numerical simulation (DNS) of a fully developed, turbulent, channel flow, the source terms were computed in planar wavenumber space. The convolution of the Green's function with the source terms, over four horizontal layers of the channel, gave partial pressures for each of the terms and regions. Studying the partial pressures gave insights into which source terms were dominant and where in the channel they were acting. Studying the spectra of the dominant source terms themselves showed that the dominant terms are closely related to generally accepted notions of coherent events in the near-wall region.

The practical motivation for this research is to model the wall pressure using the

data and information from the turbulent velocity fields. This is an area for which previous modelling attempts [Blake (1971), Chase (1980)] lacked detailed information. One-dimensional spectra and broadband correlations, important components of the MS models, were evaluated and attempts were made to model them.

The major findings from this investigation are as follows:

1. The MS and TT terms are of the same order of magnitude throughout the wavenumber range; both have the same shape as the total pressure.

2. The medium and high wavenumber ($k_x\delta, k_z\delta \geq 5$) MS partial pressure is generated in the viscous shear-layer and buffer layer, whereas the lower wavenumber ($k_x\delta, k_z\delta \leq 5$) MS partial pressure is generated in the buffer layer and logarithmic region. The contribution of the viscous shear-layer to the low wavenumber MS partial pressure is insignificant, and the upper channel contribution to the low wavenumber MS partial pressure is small. It is conjectured that the MS partial pressure is primarily due to near-wall shear layers, and that high amplitude events commonly found beneath such turbulence structures will contribute primarily to the MS partial pressure.

3. The medium and high wavenumber TT partial pressures are generated in the viscous shear-layer and buffer layer. At low wavenumbers, the TT partial pressure is due to the buffer and logarithmic regions with a significant contribution from the viscous shear-layer as well. At the lowest wavenumbers ($k_x\delta \leq 1$), all regions of the channel are important. The dominant TT partial pressures in the medium wavenumber range are due to T_{23}^{TT} and T_{13}^{TT} from the buffer layer. These terms are strongly affected by tilted quasi-streamwise vortices. The very highest spanwise wavenumber ($k_z\delta > 60$) partial pressures

are dominated by π_{23}^{TT}, π_{22}^{TT} and π_{33}^{TT} from the viscous shear-layer. These partial pressures may be generated by downward side of quasi-streamwise vortices impinging on the wall.

4. π_{12}^{TT} was found to be relatively large at high streamwise wavenumbers and may be related to near-wall shear layers, although its contributions to the wall-pressure are small compared to the MS term.

5. π_{12}^{TT} also appears to be related to spanwise vortices found in the logarithmic region. However, the distance from the wall and the concentration of energy at relatively high wavenumbers precludes them from being major contributors to the wall pressure.

6. Evaluation of the MS modelling formulation of Blake (1971) shows that the model gives a reasonable prediction of the one-dimensional MS pressure spectra when exact values of the vertical velocity spectra and broadband correlations are used. In order for such models to be used as general purpose predictive tools, however, the one-dimensional spectral densities and wall-normal correlation function of vertical velocity need to be modelled. It was shown that the streamwise spectra of v is constant across the channel. The peak of the spanwise spectra, however, shifts towards lower wavenumbers with distance from the wall. The $k_z\delta$ location of the peak varies as y^0, $y^{-1/3}$ and y^{-1} in the viscous shear-layer, buffer layer, and logarithmic region, respectively. Further efforts are necessary to scale the amplitude of the spanwise v spectra. The broadband correlations were shown to collapse to a single curve for $y/y' \leq 1.0$ when plotted versus y/y'.

7.2 Recommendations for further work

A number of areas closely related to the current work could profitably be exploited to clarify further the relationship between the velocity fields and the wall pressure and provide information for modelling in more practical geometries:

1. Using a channel flow, the wavenumber-frequency spectra of the dominant partial pressures could be obtained. This would provide data regarding the importance of the MS and TT term contributions to the $k_x - \omega$ spectrum, particularly with regard to the subconvective wavenumber range. It may also help to determine the cause of the high energy in the low-wavenumber TT partial pressures. Study of the $k_z - \omega$ space should be undertaken in order to compare with later streamwise varying flows.

2. Conditional averaging of the velocity fields could be used to validate our hypotheses regarding the relationship between the π^{MS} and near-wall shear layers, and between π_{23}^{TT}, π_{13}^{TT} and quasi-streamwise vortices. In particular, by generating a time series of MS and TT wall-pressure fields, the hypothesis that near-wall shear layers and thus, high-amplitude wall-pressure events generate the MS pressure could be validated.

3. Simulation of channel flow at higher Reynolds number would provide greater separation (in viscous units) across the channel. Such a simulation could help to answer questions about the low-wavenumber energy in the individual TT terms and may answer questions about the small energy in partial pressures due to the logarithmic region spanwise vortices.

4. Simulation of a boundary layer flow and the evaluation of the partial pressures could yield information about the low wavenumber partial pressures. Such a study could prove that the high energy in the low wavenumbers of the channel flow are due to low-wavenumber coherence of the opposite walls of the channel flow.

5. Simulation of flows with a backward facing step or adverse pressure gradient would yield information about the partial pressures and sources in other than equilibrium flows. Information from such flows are very important for development of airfoil trailing edge noise models. Particular tasks would be to compute the partial pressures in $k_z - \omega$ space; determine the dominant partial pressures and their relationship to coherent events; validate the relative importance of the MS and TT partial pressures; determine the relationship between π^{MS} and near-wall shear layers.

References

[Abraham and Keith, 1995] Abraham, B. M. and Keith, W. L. (1995). Wavenumber spectra of high magnitude wall pressure events in a numerically simulated turbulent boundary layer. In Lueptow, R., Keith, W., and Farabee, T., editors, *Flow Noise Modeling, Measurement and Contrl*, volume 230, pages 55–65. ASME.

[Bernard et al., 1993] Bernard, P. S., Thomas, J. M., and Handler, R. A. (1993). Vortex dynamics and the production of reynolds stress. *Journal of Fluid Mechanics*, 253:385–419.

[Blake et al., 1998] Blake, W., Lee, Y., and Zawadski, I. (1998). Evolving design tools for predicting aeroacoustics of rotating machinery. In *1998 ASME Fluids Engineering Division Summer Meeting*, Washington, DC. ASME.

[Blake, 1971] Blake, W. K. (1971). Turbulent velocity and pressure fields in boundary layer flows over rough surfaces. In *Symposium on Turbulence in Liquids*, pages 114–122, Univ. of Missouri, Rolla.

[Blake, 1986] Blake, W. K. (1986). *Mechanics of Flow-Induced Sound and Vibration*. Applied Mathematics and Mechanics. Academic Press, Inc., Orlando, FL.

[Bradshaw, 1967] Bradshaw, P. (1967). 'inactive' motions and pressure fluctuations in turbulent boundary layers. *Journal of Fluid Mechanics*, 30(2):241–258.

[Bradshaw, 1971] Bradshaw, P. (1971). *An Introduction to Turbulence and its Measurement*. Pergamon, Oxford, 1 edition.

[Cantwell, 1981] Cantwell, B. J. (1981). Organized motion in turbulent flow. *Annual Review of Fluid Mechanics*, 13:457–515.

[Chang et al., 1994] Chang, P., Abraham, B., and Piomelli, U. (1994). Wavenumber-frequency characteristics of wall pressure fluctuations computed using turbulence simulations. In Wang, K., von Flotow, A., Soureshi, R., Hendricks, E., and Farabee, T., editors, *1994 International Mechanical Engineering Congress and Exposition, Symposium on Active Control of Vibration and Noise*, volume DE-Vol. 75, pages 229–244, Chicago, IL. The American Society of Mechanical Engineers.

[Chase, 1980] Chase, D. (1980). Modelling the wavevector-frequency spectrum of turbulent boundary layer wall pressure. *Journal of Sound and Vibration*, 70(1):29–67.

[Choi and Moin, 1990] Choi, H. and Moin, P. (1990). On the space-time characteristics of wall pressure fluctuations. *Physics of Fluids A*, 8:1450–1460.

[Corcos, 1963] Corcos, G. (1963). Resolution of pressure in turbulence. *Journal of the Acoustical Society of America*, 35(2):192–199.

[Dhanak et al., 1997] Dhanak, M. R., Dowling, A. P., and Si, C. (1997). Coherent vortex model for surface pressure fluctuations induced by the wall region of a turbulent boundary layer. *Physics of Fluids - A*, 9(9):2716–2731.

[Eckelmann, 1974] Eckelmann, H. (1974). The structure of the viscous sublayer and the adjacent wall region in a turbulent channel flow. *Journal of Fluid Mechanics*, 65.

[Eckelmann, 1988] Eckelmann, H. (1988). A review of knowledge of pressure fluctuations. In Kline, S. and Afgan, N., editors, *1988 Zoran Zaric Memorial Conference*, pages 328–347, Dubrovnik, Croatia. Hemisphere, Washington.

[Emmerling, 1973] Emmerling R., Meier, G.E.A., and Dinkelacker, A. (1973). Investigation of the instantaneous structure of the wall pressure under a turbulent boundary layer. *AGARD Conf. Proc.*, AGARD-CP-131.

[Farabee, 1986] Farabee, T. M. (1986). An experimental investigation of wall pressure fluctuations beneath non-equilibrium turbulent flows. Ship Acoustics Department Research and Development Report DTNSRDC-86/047.

[Farabee and Casarella, 1991] Farabee, T. M. and Casarella, M. (1991). Spectral features of wall pressure fluctuations beneath turbulent boundary layers. *Physics of Fluids - A*, 3(10):2410–2420.

[Germano et al., 1991] Germano, M., Piomelli, U., Moin, P., and Cabot, W. H. (1991). A dynamic subgrid-scale eddy viscosity model. *Physics of Fluids A - Fluid Dynamics*, 3(7):1760–1765.

[Handler et al., 1984] Handler, R., Hansen, R., Sakell, L., Orszag, S., and Bullister, E. (1984). Calculation of the wall-pressure field in a turbulent channel flow. *Physics of Fluids*, 27(3):579–582.

[Hestenes and Stiefel, 1952] Hestenes, M. and Stiefel, E. (1952). Methods of conjugate gradients for solving linear systems. *J. Res. Natl. Bur. Stand.*, 49(409).

[Hwang and Maidanik, 1990] Hwang, Y. and Maidanik, G. (1990). A wavenumber analysis of the coupling of a structural mode and flow turbulence. *Journal of Sound and Vibration*, 142(1):135–152.

[Johansson et al., 1987a] Johansson, A., Alfredson, P., and Eckelmann, H. (1987a). On the evolution of shear-layer structures in near-wall turbulence. In Comte-Bellot, J. and Mathieu, J., editors, *Advances in Turbulence*, pages 383–390. Springer Berlag, Heidelburg.

[Johansson et al., 1987b] Johansson, A. V., Her, J.-Y., and Haritonidis, J. H. (1987b). On the generation of high-amplitude wall-pressure peaks in turbulent boundary layers and spots. *Journal of Fluid Mechanics*, 175:119–142.

[Johansson et al., 1988] Johansson, A., Alfredson, P., and Kim, J. (1988). Velocity and pressure fields associated with near-wall turbulence structures. In Kline, S. and Afgan, N., editors, *1988 Zoran Zaric Memorial Conference*, pages 368–379, Dubrovnik, Croatia. Hemisphere, Washington.

[Kammeyer, 1995] Kammeyer, M. (1995). An experimental investigation of organized turbulent motions and wall-pressure fluctuations in complex flows. Technical Report NSWCDD/TR-95/222, Naval Surface Warfare Center/Dahlgren Division.

[Karangelen et al., 1991] Karangelen, C. C., Wilczynski, V., and Casarella, M. J. (1991). Large amplitude wall pressure events beneath a turbulent boundary layer. In Farabee, T. M., Keith, W., and Lueptow, R., editors, *The Winter Annual Meeting of the ASME*, volume 11, pages 45–53, Atlanta, GA. ASME. Flow Noise, Modeling, Measurement and Control.

[Keith et al., 1992] Keith, W. L., Hurdis, D., and Abraham, B. (1992). A comparison of turbulent boundary layer wall-pressure spectra. *Journal of Fluids Engineering*, 114:338–347. Scaling of spectra.

[Kim, 1989] Kim, J. (1989). On the structure of pressure fluctuations in simulated turbulent channel flow. *Journal of Fluid Mechanics*, 205:421–451.

[Kim and Lee, 1989] Kim, J. and Lee, M. J. (1989). The structure of pressure fluctuations in turbulent shear flows. In *Seventh Symposium on Turbulent Shear Flows*, volume 1, pages 1.1.1–1.1.6, Stanford University.

[Kim et al., 1987] Kim, J., Moin, P., and Moser, R. (1987). Turbulence statistics in fully developed channel flow at low reynolds number. *Journal of Fluid Mechanics*, 177:133–166.

[Ko and Schloemer, 1992] Ko, S. H. and Schloemer, H. H. (1992). Flow noise reduction techniques for a planar array of hydrophones. *Journal of the Acoustical Society of America*, 92(6):3409.

[Kraichnan, 1956] Kraichnan, R. H. (1956). Pressure fluctuations in turbulent flow over a flat plate. *The Journal of the Acoustical Society of America*, 28(3):378–390.

[Kreplin and Eckelmann, 1979] Kreplin, H. and Eckelmann, H. (1979). Behavior of the three fluctuating velocity components in the wall region of a turbulent channel flow. *Physics of Fluids*, 22.

[Lilley, 1960] Lilley, G. (1960). Pressure fluctuations in an incompressible turbulent boundary layer. Technical Report 133, College of Aeronautics, Cranfield.

[Lueptow, 1995] Lueptow, R. M. (1995). Local wall pressure gradient events in turbulent wall-bounded flow. In Lueptow, R., Keith, W., and Farabee, T., editors, *Flow Noise Modeling, Measurement and Contrl*, volume 230, pages 75–85. ASME.

[Martin and Leehey, 1982] Martin N.C. and Leehey, P. (1977). Low wavenumber wall pressure measurements using a rectangular membrane as a spatial filter. *Journal of Sound and Vibration*, 52(1):95–120.

[Moin and Kim, 1982] Moin, P. and Kim, J. (1982). Numerical investigation of turbulent channel flow. *Journal of Fluid Mechanics*, 118:341–377.

[Morrison and Kronauer, 1969] Morrison, W. and Kronauer, R. (1969). Structural similarity for fully developed turbulence in smooth tubes. *Journal of Fluid Mechanics*, 39(1):117–141. Used by Chase(1980).

[Olivero-Bally et al., 1993] Olivero-Bally, P., Forestier, B. E., Focquenoy, E., and Olivero, P. (1993). Wall-pressure fluctuations in natural and manipulated turbulent boundary layers in air and water. In *FED/Flow Noise Modelling, Measurement and Control*, volume 168. ASME.

[Panton and Linebarger, 1974] Panton, R. L. and Linebarger, J. H. (1974). Wall pressure spectra calculations for equilibrium boundary layers. *Journal of Fluid Mechanics*, 65(2):261–287.

[Piomelli, 1993] Piomelli, U. (1993). High reynolds number calculations using the dynamic subgrid-scale stress model. *Physics of Fluids - A*, 5(6):1484–1490.

[Robinson et al., 1988] Robinson, S., Kline, S., and Spalart, P. (1988). Quasi-coherent structures in the turbulent boundary layer: Part ii. verification and

new information from a numerically simulated flat-plate layer. In Kline, S. and Afgan, N., editors, *1988 Zoran Zaric Memorial Conference*, pages 218–247, Dubrovnik, Croatia. Hemisphere, Washington.

[Robinson et al., 1989] Robinson, S., Kline, S., and Spalart, P. (1989). A review of quasi-coherent structures in a numerically simulated turbulent boundary layer. Technical Memorandum 102191, NASA.

[Robinson, 1991a] Robinson, S. K. (1991a). Coherent motions in the turbulent boundary layer. *Annual Review of Fluid Mechanics*, 23:601–639.

[Robinson, 1991b] Robinson, S. K. (1991b). Kinematics of turbulent boundary layer structure. Technical Memorandum 103859, NASA.

[Russell, 1997] Russell, S. J. (1997). *Wall pressure signatures of organized turbulent motions*. Phd, The Catholic University of America.

[Schewe, 1983] Schewe, G. (1983). On the structure and resolution of wall-pressure fluctuations associated with turbulent boundary layer flow. *Journal of Fluid Mechanics*, 134:311–328.

[Singer, 1996] Singer, B. A. (1996). Large-eddy simulation of turbulent wall-pressure fluctuations. Technical Report NASA CR-198276, NASA.

[Thomas and Bull, 1983] Thomas, A. and Bull, M. (1983). On the role of wall-pressure fluctuations in deterministic motions in the turbulent boundary layer. *Journal of Fluid Mechanics*, 128:283–322.

[Wallace et al., 1972] Wallace, J., Eckelmann, H., and Brodkey, R. (1972). The wall region in turbulent shear flow. 54:39–48.

[Wilczynski, 1992] Wilczynski, V. (1992). *Organized turbulent structures and their induced wall pressure fluctuations*. Phd, Catholic University of America.

[Williamson, 1980] Williamson, J. (1980). Low-storage Runge-Kutta schemes. *J. Computational Physics*, 35(48).

[Willmarth, 1975] Willmarth, W. W. (1975). Pressure fluctuations beneath turbulent boundary layers. *Annual Review of Fluid Mechanics*, 7(13):13–38.

[Zang, 1991] Zang, T. (1991). On the rotational and skew-symmetric forms for incompressible flow simulations. *Appl. Num. Math.*, 7(27).

[Zang and Hussaini, 1986] Zang, T. A. and Hussaini, M. Y. (1986). On spectral multigrid methods for the time-dependent navier-stokes equations. *Applied Mathematics and Computation*, 19:359–372.

[Zawadski et al., 1996] Zawadski, I., Gershfeld, J., Na, Y., and Wang, M. (1996). Hydroacoustic forcing function modeling using dns database. Proceedings of the summer program 1996, Center for Turbulence Research.